Design of Soft Implantable Devices For Tissue Regeneration

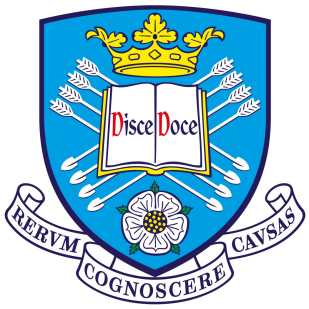

The University Of Sheffield.

Eduardo Roberto Perez Guagnelli

Department of Automatic Control and Systems Engineering
University of Sheffield

This dissertation is submitted for the degree of
Doctor of Philosophy

February 2021

Abstract

Tissue repair has largely been approached with either tissue engineering or robotic-assisted grafting techniques, but in recent years, the strategy of combining mechanical stimulation to promote cell proliferation and robotics has shown to be a promising alternative to traditional regeneration techniques. Nevertheless, this approach presents the challenge of triggering a fibrotic response in the organ, where the mechanotherapy robot is placed, which may affect its physiological, anatomical and metabolic functions. The general hypothesis of this work is that soft implantable devices that can provide controlled and localized mechanical stimulation are a physiologically, anatomically and metabolically compatible alternative to the current strategies for tissue regeneration.

In this thesis, firstly we propose a soft pneumatic actuator, that can be helically arranged to provide multi-modal motions, in agreement with the anatomical needs of the target organ, as well as load-bearing capabilities and a control scheme that regulates the stimulation provided to the tissue during therapy. Soft actuators are the building blocks of soft robots that enable their motion and thus, secondly, derived from the inherent performance efficiency and reliability requirements for such a device as a medical tool, a systematic design analysis focused on its building blocks' geometry, configuration and response to variable loads is presented. As a result of this analysis conformed by numerical, statistical and experimental procedures we provide a set of design principles for the design of highly reliable soft pneumatic actuators. Finally, informed by those principles, we introduce the design, fabrication and characterization of two soft pneumatic actuators that supersede the extension and load-bearing capabilities of its previous version, and of many other state-of-art soft actuators, providing the devices with an ability to treat a wider range of short-tissue related conditions.

Acknowledgements

I would like to express my foremost gratitude to my supervisor, Dr Dana D. Damian for her guidance throughout this project. Thanks to her passionate and hard-working supervision I have gained valuable skills for which I will ever be grateful. I would also like to thank my second supervisor, Dr Sean Anderson, who was always available to provide me with level-headed advice when I needed it.

This work would not have been possible without the support of a long list of team members and friends from the Sheffield Biomedical and Microrobotics Labs, Sheffield Robotics and the Department of Automatic Control and Systems Engineering. They were always there offering me help and motivation. Particularly, I would like to express my gratitude to Dr Shuhei Miyashita, who always looked after my development as a researcher; and Joanna Jones, who has been an incredible support during my time in the lab.

I want to thank my parents. They have always supported me along my educational journey, providing me with all the tools I needed to become who I am today. They have been for me an unwavering reference point of hard work, resilience, and above all, integrity. I am deeply grateful to my beloved wife for all her unconditional support and encouragement during this project. To her, I dedicate this work.

Lastly, this work would not have been possible without the financial support of the Mexican National Council of Science and Technology and The University of Sheffield.

Table of contents

List of figures

List of tables

Chapter 1

Introduction

This work has two aims, one clinical: to treat short-tissue conditions in the gastrointestinal (GI) tract caused by congenital diseases or surgical resections, and one technical: to develop versatile implants that are mechanically, physiologically and metabolically effective, while anatomically and safely compliant to support tissue growth. Thus, in this section we briefly introduce the anatomy and physiology of the digestive system. Then, we describe pathologies affecting tubular organs in the GI tract that cause short-tissue related conditions, such as Long-Gap Esophageal Atresia (LGEA) and Short Bowel Syndrome (SBS) which motivate the aims of this work, followed by an overview of current available treatments. Next, we introduce the challenges imposed by the technical and clinical aims and which strategies we used to overcome them, as well as the design requirements to fulfill those aims. Then, we describe the overarching hypothesis and objectives of this work, as well as providing a preview of its contributions, an overview of the publications resulted from this project and the outline for this thesis. A general background is presented in this section to describe the motivations and define the problems to be addressed. A more descriptive review of the current state of the art, technical and clinical challenges is detailed in Chapter 2. Moreover, each of the chapters describing the work done (Chapters 3-5) has a detailed introduction, relevant to the specific aim discussed therein.

1.1 Motivation

1.1.1 Anatomy and Physiology of The Digestive System

Through the ingestion of food, the cells of the body obtain their required energy, undertake their synthetic processes and the digestive system transfers the nutrients from the food into its internal environment to distribute them to the cells via the circulation. The GI tract is a

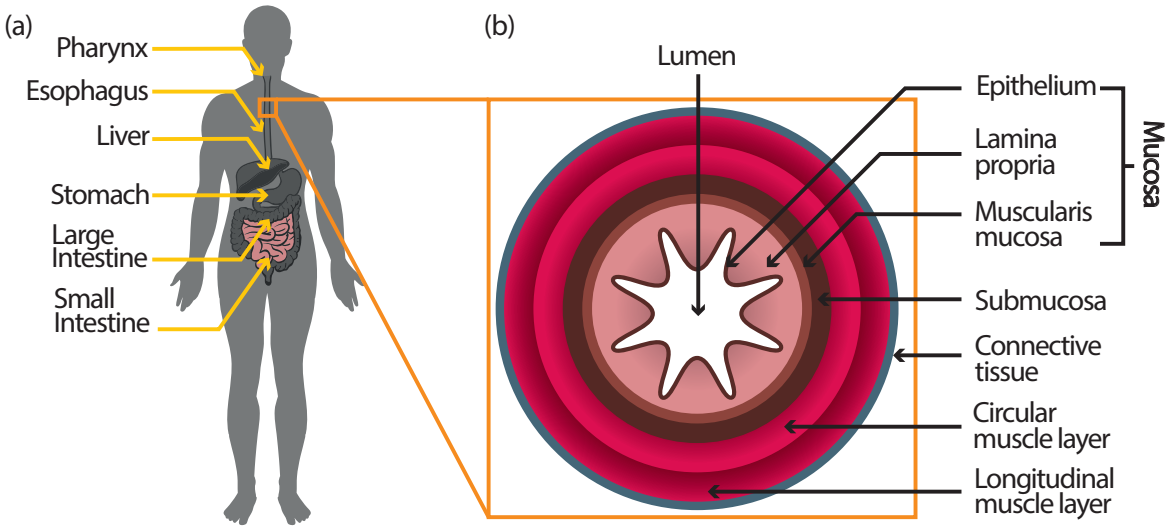

Fig. 1.1: Digestive system. (a) Overview of the organs that make up the digestive system. (b) Cross-sectional view of the multi-layered tubular structure of the GI tract.

tube of inconsistent diameter, with a length of ~ 4.5 meters that is made up of the mouth, esophagus, stomach, small and large intestine that, by the activity of skeletal muscle, takes the food from the mouth into the pharynx (Fig. 1.1(a)). The food is moved, dissolved and degraded into a semi-fluid consistency by contractions in the smooth muscles along the GI tract. These smooth muscles are configured in two layers, an inner circular muscle layer and an outer longitudinal muscle layer [183] (Fig. 1.1(b)).

The functioning of the digestive system is based on four relevant processes: (1) Digestion, which is the degradation of complex molecules, for example proteins into smaller molecules, such as amino acids. (2) Absorption, that is transportation of the products of digestion through the epithelial cell membranes (Fig. 1.1(b)) to the lymph or blood to reach circulation. (3) Motility, the process of moving the food throughout the GI tract, mixing the contents in the lumen that is carried out by hormones and nerves. (4) Secretion, which is the release of substances such as enzymes into the GI tract by the exocrine glands and elimination of bacteria and undigested material out of the body [183].

1.1.2 Pathologies of The GI Tract That Lead To Tissue Shortage

Considering that the digestive system involves a large number of organs and glands, the pathologies that can affect its correct function are diverse. The common denominator of these pathologies is an impact on the metabolic needs of the individual, caused by a sub-optimal performance of digestion, absorption, motility and/or secretion processes. In this section, we concisely describe pathologies related to a shortening in tubular organs of the GI tract

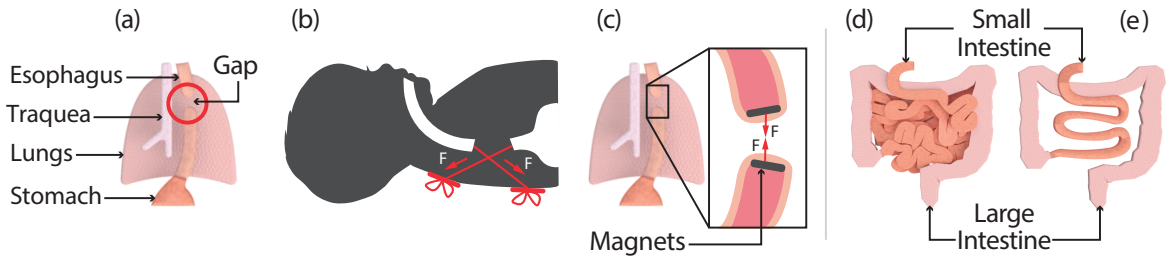

Fig. 1.2: Short-tissue conditions. (a) Diagram showing the anatomy in the first half of the GI tract affected by esophageal atresia. (b) Foker's technique for the treatment of Long-Gap Esophageal Atresia (LGEA) in which lengthening is produced by pulling sutured strings to the organ from the newborn's back. (c) Magnetic compression, an alternative approach for the treatment of LGEA that consists of stretching the tissue using magnetic force to ease anastomosis of the two blind ends of the esopghagus. (d) Anatomy of the small intestine prior and (e) after segmental resection.

that impact on its correct function, specifically congenital malformations and segmental resections.

1.1.2.1 Congenital Malformations

Congenital malformations can occur at any part of the GI tract, from the esophagus to the anus. These malformations show two particular conditions: (1) atresias (Fig. 1.2(b)), absence or abnormal narrowing of an opening or passage in the body; and (2) fistulas, an abnormal connection between two hollow spaces in the organs. Some of the most common congenital malformations are esophageal and intestinal atresias [189]. Esophageal atresias have an incidence of 1 in $2500-4000$ live births. Most of esophageal atresias (EA) show a distal tracheoesophageal fistula, although, it is also possible to find EA without tracheoesophageal fistulas [189]. In the later case, the distance between the two extremes of the esophagus exceeds the possibilities of a primary anastomosis to close the esophageal gap (Fig. 1.2(b)). In these cases, when the gap is ≥ 3 cm and up to 10 cm, the condition is called Long-Gap Esophageal Atresia (LGEA), causing esophageal leak and dysphagia among other morbidities and preventing the food to reach the stomach, resulting in malnutrition [88].

1.1.2.2 Segmental Resections

The treatment of cancer is the cause of most major surgical resections in the GI tract, which aim to remove primary tumours before they become metastatic [158]. If the resection is performed in the small intestine (Fig. 1.2(e)), in most cases patients can prescind from nutritional support thanks to the redundancy in this organ. However, the reduction of surface area can negatively affect absorption processes, causing Short Bowel Syndrome (SBS). This condition causes dehydration, malnutrition, diarrhea and weight lose, and if it occurs in

children, it causes low growth [183]. On the other hand, the esophagus is a non-redundant organ, that has a limited regeneration ability and it cannot be transplanted [158]. Thus, gastric or colon conduits are required if an esophagectomy is performed to keep luminal continuity, leading to a series of morbidities and therefore, a poor quality of life. Therefore, esophageal tissue regeneration would be an ideal alternative to traditional strategies to keep luminal continuity [57].

1.1.3 Current Treatments for Short-Tissue-Related Diseases

If more than two thirds of the small intestine are resected, intravenous fluid and nutritional support may be required to satisfy the metabolic requirements of the individual. This should be aided by the use of medicines that reduce gastric juice and duodenum secretions [221]. The treatment of SBS could be assisted by the consumption of growth hormones, stimulating the growth of the epithelium (Fig. 1.1(b)) and potentially affecting other functions in the organ. Surgical treatment involves changing the morphology of the intestine but with potential hepatic complications [58]. If a section of the esophagus is resected, continuity in the GI tract is currently restored in two ways: (1) Mobilizing the stomach into the chest to connect it to the remaining esophagus or (2) grafting a section of the small intestine into the gap between the remaining esophagus and the stomach. These procedures cause motility impairment, affecting peristalsis and ultimately the quality of life of the patient [183].

The most popular procedure to treat LGEAs is the Foker's Technique (Fig. 1.2(b)). It consists of making an incision in the back of the newborn, placing sutures on the lower and upper ends of the oesophagus, connecting them to the outside and applying tension to increase the length about one or two millimetres per day. The baby is sedated to be motionless and stays in intensive care in a breathing machine. X-ray imaging is performed to verify the ongoing progress. This technique has been modified to make it simpler and safer [132], however LGEA is still a challenging condition in pediatrics [215]. Magnetic compression is an alternative approach in which magnets are placed at both blind ends of the esophagus to make them attract each other in order to stretch the tissue, reducing the gap and easing anastomosis. However, this approach presents important drawbacks, such as esophageal leaks and the risk of tissue tearing and perforation due to the exponential increase of attraction forces between the magnets as the gap is reduced (Fig. 1.2(c)) [114].

1.2 Challenges and Design Requirements

Because of the complex anatomy and physiology of the gastrointestinal tract, developing versatile implants that are mechanically, physiologically and metabolically effective, while being anatomically and safely compliant, and that support tissue growth yields the following clinical challenges:

Mechanical compatibility: to provide therapeutical stimulation while minimizing foreign body response, caused by inflammation due to the implant's presence or mechanical incompatibilities with the host organ or surrounding tissues, e.g. during the interaction with the intraluminal layers in the GI tract.

Anatomical compatibility: to develop an implant that adapts to the shape and space needs of the host organ, e.g. by having a structure that fits to the restrictive areas in or around the GI tract.

Physiological compatibility: to develop an implant that stimulates effectively the muscle layers of tubular organs in order to restore their functions such as motility and absorption, e.g. by applying axial traction forces to the host tubular organ to make it grow, while exerting radial stimulation to keep its tubularity. The type of forces that promote tissue growth are still unknown, thus the new technology needs to have a flexible stimulation range to allow this investigation to be run.

Metabolic compatibility: to provide dynamic healing and regeneration procedures, while restoring the organ's relevant processes. The type of forces that promote GI healing and regeneration are still unknown, thus the new technology needs to have a flexible stimulation range to allow this investigation to be run.

Safe implantation: to reduce patient discomfort and post-operative trauma caused by invasive methods of implantation.

In addition, addressing those clinical challenges impose the following technical challenges:

Safe and effective tissue interaction: in order to develop a fully mechanically, physiologically and metabolically compatible tissue regeneration strategy the device must be capable of performing controlled, localized and multi-modal motions while keeping a compliant structure.

Ease of implantation: in order to make the device easy to place within the body it should be provided with a compact and scalable design that allows it to be implanted without the need of open surgery.

Monitoring: the device must provide real-time feedback of its functioning and progress of the therapeutic procedure in order to deliver reliable treatment as well as to avoid tissue damage.

In this work, we address those challenges by proposing a soft-matter based approach that combines tissue repair principles from regenerative medicine and the application of precise control-based forces and displacements provided by robotics. This approach was first employed in one of our research publications contained within Section 3 [156] and then summarized by D. Damian (2020) [40]. By deriving the previously described challenges and the clinical benefits of overcoming them into technical strategies to implement the aforementioned interdisciplinary approach, we elicited the following design requirements for the development of soft robotic implants for tissue regeneration:

Minimally Invasive Implantation: the design of the robotic device should allow it to be implanted via minimally invasive procedures, either laparoscopically or through keyhole surgery. This requirement addresses the safety and ease of implantation challenges. Further description of minimally invasive procedures is presented in Section 2.3.1.

Universal: the implant should keep functional performance while having a compact and scalable design through morphological strategies, such as modularity and/or configurability. These criteria addresses the anatomical compatibility and ease of implantation challenges.

Safe: the device should be able to operate safely *in vivo* by being mechanically compliant with surrounding organs and tissues, reducing its impact from foreign body responses and decreasing inflammation. These criteria addresses the mechanical compatibility requirement and contributes to address the challenge of safe interaction.

Multi-functional: the robotic implant should provide multi-modal motion capabilities according to the physiological and metabolic functions of the host organ produced by its multi-layer composition. In this work, we define multi-modality and multi-functionality interchangeably to the capacity of the implant to perform at least two different motions independently and simultaneously. This criterion addresses the metabolic and physiological compatibility challenges and contributes to address the challenge of safe interaction.

Table 1.1: Design requirements for the development of new regenerative robots. Adapted from [40].

Design Requirement	Clinical Benefits	Technical Strategy
Minimally invasive implantation	Patient safety and comfort	Via laparoscopy or key-hole surgery
Universal	Compact implantable	Modularity, re-configurability, scalability
Safe	Reduced fibrosis	Mechanical compliance
Multi-functional	Metabolic functions restoration	Multi-modality
Controlled operation	Effective therapy delivery	Autonomy and programmability
Biocompatibility	Patient safety	Non-toxic components / encapsulation

Controlled operation: robotic implants should deliver robust functionality during the entire therapy time to regenerate tissue. During this period, they should minimize the risk of failure through fault-tolerant mechanisms, self-recovery or adaptive control and constant monitoring. These criteria address the monitoring challenge and contributes to address the safe interaction challenge.

Biocompatible: The materials that shape or encapsulate the robotic implant should not react chemically to or affect pathologically the organs, tissue or their surroundings. This criterion addresses the challenge of safe interaction, however, it is out of the scope of this thesis, but recommendations to fulfill it are provided in Section 6.

These requirements are summarized in Table 1.1 next to the clinical benefits and the technical strategies used in this work to fulfill them. Although these requirements correspond to the overall work presented in this thesis, each of the technical Chapters 3, 4 and 5 discuss their own design criteria to fulfill the objectives established therein.

1.3 Hypothesis and Objectives

The general hypothesis of this work is that soft implantable devices that can provide controlled and localized mechanical stimulation are a physiologically, anatomically and metabolically compatible alternative to the current strategies for tissue regeneration. Derived from the clinical and technical aims and the design requirements presented in Section 1.2 these are the specific objectives of this work:

A. To design, fabricate and validate a soft actuator that can be can be configured in versatile geometries.

B. To configure a soft robot able to provide multi-modal functions that can be implanted through minimally invasive procedures.

C. To develop and validate a control scheme that regulates the behaviour of the robot's multi-modal functions.

D. To analyze, characterize and validate the reliability performance of the building blocks of a multi-modal soft robot under variable loads and configurations.

E. To design, optimize, characterize and validate the capabilities of the robot based on the integrated knowledge.

1.4 Preview of Contributions

As a result of addressing the previously described aims and objectives, this work presents the following contributions:

1. Introduction of the concept of coiling soft assembly for realizing the first deployable, multi-modal, configurable, soft yet strong soft robotic implant to achieve interdependent axial and radial expansion of tissue. The coiled assembly can potentially be placed intraluminally or around body parts, even with irregular topology, and provide mechanical stimulation by emerging balloons in a safe and controlled manner.

2. Design, fabrication, testing and validation of a physical *in vivo* simulator of biological tissue's stiffness and growth to evaluate the performance of technologies for tissue regeneration via mechanostimulation under realistic conditions.

3. Design of a model-based multi-stage control according to the tubular tissue's physiological response to actuate soft pneumatic actuators.

4. Design and fabrication of two hard and semi-soft implant-to-tissue attachment methods and testing of their effects on the tissue's elongation depending on the mechanical forces exerted by the implant.

5. Set of design principles for the fabrication of reliable soft pneumatic actuators based on a systematic analysis of their design and performance under variable loading and deflection conditions.

6. Morphological optimization of multi-modal hybrid semi-soft robots that overcome the common trade-off of softness vs strength and high extension rates in soft robotics.

1.5 Publications

This thesis represents the author's own work, and includes a number of original contributions to scientific knowledge. The work presented herein has led so far to five publications in academic journals and conferences:

1. **E. Perez-Guagnelli**, S. Nejus, J. Yu, S. Miyashita, Y. Liu, and D.D. Damian. "Axially and radially expandable modular helical soft actuator for robotic implantables". *IEEE International Conference on Robotics and Automation*, 2018 (pp. 1-9).

2. **E. Perez-Guagnelli**, J. Jones, and D.D. Damian. "Evaluation of a soft helical actuator performance with hard and soft attachments for tissue regeneration". *In Proc. 12th Hamlyn Symposium on Medical Robotics.* 2019, (pp. 3-4).

3. **E. Perez-Guagnelli**, J. Jones, A.H. Tokel, N. Herzig, B. Jones, S. Miyashita, and D.D. Damian. "Characterization, Simulation and Control of a Soft Helical Pneumatic Implantable Robot for Tissue Regeneration". *IEEE Transactions on Medical Robotics and Bionics*. 2020, 2(1), pp.94-103.

4. **E. Perez-Guagnelli**, and D.D. Damian. "Deflected vs Pre-shaped Soft Pneumatic Actuators: A Design and Performance Analysis Towards Reliable Soft Robots". *Soft Robotics*. 2021, (In Press).

5. **E. Perez-Guagnelli**, J. Jones, and D.D. Damian. "Hyperelastic Membrane Actuators: Analysis of Toroidal and Helical Multifunctional Configurations". *Cyborg and Bionic Systems*. 2021, (Conditional Acceptance).

6. **E. Perez-Guagnelli**, P. Mitrev and D.D. Damian. "Configurable Soft Tool for Mechanotherapy Based Tissue Repair". *Children's Technology Conference*, 2021.

Publication 1 was presented orally as a research poster in the International Conference of Robotics and Automation (ICRA) 2018, held in Brisbane, Australia. Publication 2 was presented orally as short paper by the author himself in the Hamlyn Symposium for Medical Robotics 2019, in London, UK. The introductory and related work material from Publications 1, 2 and 3 have contributed to the contents of Chapters 1 and 2. The contents in Publications 1, 2 and 3 correspond to the contents in Chapter 3 and in Appendix A. The content in Publication 4 corresponds to the content in Chapter 4. The results of Publications 1,2,3 and 4 contributed to the contents of Publication 5, Chapter 5 and Appendix B. Publication 6 contributed to the content of Appendix A.3.

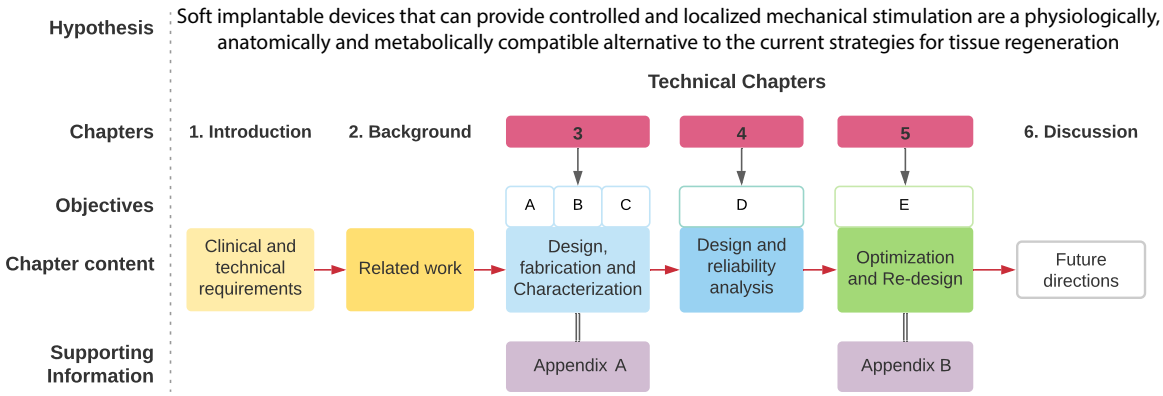

Fig. 1.3: Thesis outline.

In addition to the main body of work of the author, he has also contributed to other projects that are not featured in this thesis. These have led to the following publications:

1. J. Jones, Z. Gillett, **E. Perez-Guagnelli** and D. D. Damian. "Resistance Tuning of Soft Strain Sensor based on Saline Concentration and Volume Changes". *Towards Autonomous Robotic Systems*. 2020, pp. 49-52; Springer.

2. N. Herzig, J. Jones, **E. Perez-Guagnelli**, D. D. Damian; "Model and Validation of a Highly Extensible and Tough Actuator based on a Ballooning Membrane". *IEEE International Conference on Robotics and Automation*. 2021, (In Press).

1.6 Thesis Outline

This thesis is structured as follows and a diagram summarizing it can be found in Fig. 1.3.

- Chapter 2 provides an overview of the context in which this thesis is placed. Sections 2.1, 2.2 and 2.3 define and discuss current approaches to tissue repair. Section 2.4 discusses the state of the art in the use of robotic implants that provide controlled mechanical stimulation as an alternative to current techniques in tissue repair. A soft robotics approach is used in this work in designing minimally invasive implants. Therefore, Section 2.6 presents an introduction on these technologies. The chapter concludes with the introduction of the concept of soft robotic implants and briefly discusses how the approach used in this work combines the interdisciplinary capabilities of regenerative medicine and robotics.

- Chapter 3 discusses the challenges of soft robotics in implantable technology and propose a conceptual design and fabrication of a Soft Pneumatic Helically Interlayered

Actuator (SoPHIA) that can be used as an implant for mechanotherapy in Section 3.4. Then, we present the analytical modeling and experimental characterization of the SoPHIA's extension and expansion in Section 3.5, as well as an *ex vivo* testing of the SoPHIA using novel hard and semi-soft implant-to-tissue adaptors in Section 3.6. Next, we introduce a benchtop testing using a physical simulator for staged mechanotherapy in Section 3.8.1.1 and the force (Section 3.6.3) and extension (Section 3.6.2) characterization of the SoPHIA, as well as discussion of the obtained results. This Chapter addresses objectives A-C described in Section 1.3.

- Chapter 4 analyzes systematically the design of the Soft Pneumatic Actuators (SPAs) used as building blocks in the SoPHIA in Chapter 3 and variations in their geometry and configuration to evaluate their reliability and response to variable loads. As a result of this analysis conformed by numerical, statistical and experimental procedures we provide a set of design principles that contribute to the design of more reliable SPAs (Section 4.6.4). This Chapter addresses objective D described in Section 1.3.

- Chapter 5 presents the development of a series of numerical models to guide the design optimization of the SoPHIA, building on the results of the analysis conducted in Chapter 4 as a strategy to optimize the extension and strength capabilities shown in Chapter 3. The methodology used in this Chapter addresses the requirements of extensibility, multi-modality, modularity and structural strength. Finally, we propose, fabricate and test two devices whose designs are based on highly reliable SPAs that will enable higher extension rates with more homogeneous expansions in soft robotic implants for tissue regeneration. This Chapter addresses objective E described in Section 1.3

- Chapter 6 concludes the thesis and discusses its limitations, as well as it provides a number of potential directions for future work.

Chapter 2

Background and Related Work

In this Chapter, we describe the state of the art of the multidisciplinary fields that make up the proposed technical approach presented in this work and review the current available strategies to provide tissue repair treatment. We conclude with a summary that describes how those fields and strategies were combined to develop a new series of robotic implants for tissue regeneration presented in this thesis.

2.1 Tissue Repair

Effective tissue regenerative capacity is crucial for the survival of all living creatures. Each year, millions of people around the world are affected by deficient wound healing after chronic conditions, surgery or trauma, due to poor tissue regeneration caused by a number of factors, including inflammation and angiogenesis [62]. This imposes an important medical need to improve therapeutical strategies that improve the body's endogenous capacity to regenerate tissue [63]. Tissue repair is a complex process that aims to recover the structure and functions of organs and tissues via dynamic cell migration, proliferation and stimulation to remodel collagen to shape a scar and generate new vascular networks through regeneration and replacement pathways [127, 102].

Tissue regeneration is the process of restoring entirely the injured organ or tissue to its functioning state. When tissue regeneration is not possible, the body tries to replace the irreparably damaged tissue by remodeling connective tissue made of collagen in the affected area [102]. One averse effect of poor replacement capacity is activation of a fibrotic response, an excessive accumulation of collagenous connective tissue surrounding the affected area that decreases tissue function and might lead to organ failure [63]. Although it is possible to repair tissue entirely through regeneration, it is more frequent that tissue injuries are healed by a combination of replacement and regeneration [102].

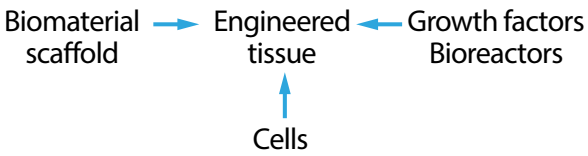

Fig. 2.1: Tissue engineering triad. (Adapted from [142], Copyright © 2011 Elsevier Ltd.).

2.2 Regenerative Medicine

Regenerative medicine is an interdisciplinary field of translational medicine that includes cell and gene therapy, tissue engineering and biomaterial manipulation [137]. Regenerative medicine aims to repair or regenerate tissues and organs functions affected by resections, diseases or traumas by processing cells and tissues from donors (allografts) or the patients themselves (autografts) [92]. The replacement of body parts to restore function by using prostheses made of ivory, as in dentures, or wood to fabricate legs can be considered the beginning of regenerative medicine [129]. An important breakthrough within the modern concept of regenerative medicine was the work of Johan Dieffenbach performing skin transplantation pre-clinically and clinically between 1792 and 1847 [51], establishing methods to use skin flaps successfully [129]. The treatment of injured or resected organs and tissues is typically focused on transplantation due to being lifesaving. However, it involves a series of problems including high cost, donor-site morbidity, anatomical limitations, risk of infection and rejection by the immune system of he patient [142]. In the following sections we discuss different strategies within the field of regenerative medicine that offer an alternative to traditional grafting techniques.

2.2.1 Tissue Engineering

An alternative to grafting and organ transplants is tissue engineering, a multidisciplinary field within regenerative medicine that aims to restore, improve or maintain tissue function by developing biological substitutes of the damaged organ or tissue using scaffolds, where cell proliferation is encouraged by chemical growth factors [212] (Fig. 2.1). Additional to scaffold-based strategies, which have shown to achieve, for example, in-situ repair in bone tissue [28] or bioengineered valves through biomechanical conditioning [138], new methods have been developed in recent years. These methods include the use of biological actuation, biochemical patterning of growth factors through the manipulation of nanoparticles using magnetic fields [111], materials assembly, in vitro and intraoperative bioprinting [222].

Tissue engineering practices present different challenges such as spatiotemporal delivery of growth factors, dispersion of primary cells and incorporation of extensive vascular well-

organised networks [9]. These challenges can become more difficult if the organs have intricate tridimensional structures and complex interactions with surrounding tissue. Despite of the significant development of methods to improve its techniques, tissue engineering still faces the drawbacks of stability towards biodegradation in its materials [212], fibrotic response and the tendency to produce strictures at the site of their implantation [145] that compromises the viability of the organ function, the need for a sustainable production method [95], lack of vascularity and poor mechanical compatibility of the scaffolds to be used, for example, in load bearing orthopedic applications. In summary, accommodating patient variation in a tissue engineering approach is still a challenging task and distant goal [102].

2.2.1.1 Tissue Engineering in the GI Tract

Aiming to overcome the negative effects of surgical resections in the GI tract such as reduction of life quality (Section 1.1.2), the field of regenerative medicine and tissue engineering have tried to construct artificial organs in situ [92]. Due to its relative simplicity, the esophagus (Fig. 1.1 (a)) has been widely studied with successful regeneration in parts of the esophageal walls and full circumference [57, 86]. However, it remains a challenge to replace the full circumference and full wall-thickness of the esophagus with its multiple layers [159, 199] (Fig. 1.1 (b)).

Recently, a study described the first human case of regrowing 5 cm of esophagus in situ in which the diet and weight of the patient remained normal at 4 years of follow-up [56]. However, the authors reported the following limitations: (1) Lack of information about the time duration of regeneration process; (2) no histological assessment of the immunological response to the treatment; (3) lack of information about esophageal residue that might cause bleeding and fistula formation. Additionally, monitoring of the treatment was performed endoscopically. Although this is a milestone in tissue regeneration, the followed process needs to be replicated in phases 1 and 2 of clinical trials and the lack of monitoring information makes this replication challenging [56].

Organs in the GI tract that perform digestive processes such as the stomach and small intestine perform more complex functions than the esophagus, such as absorption of nutrients. This adds more challenges to the engineering of tissue growth, which relates to the restoration of one of its main functions, not only structural restoration, limiting tissue engineering to be focused mainly on reconstruction of their epithelium [126] (Fig. 1.1 (b)) and reinforcement of the gastric walls [92], leaving full wall and circumference reconstruction distant from achievement.

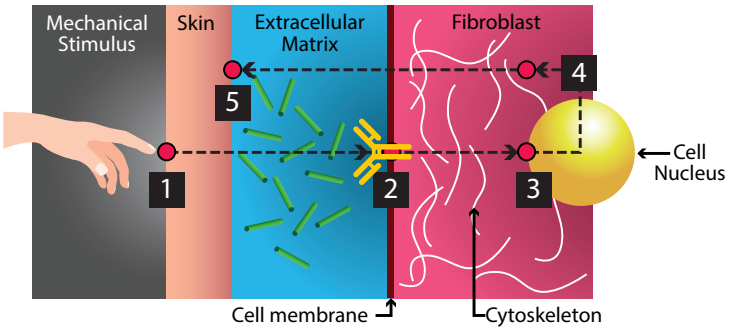

Fig. 2.2: Mechanotransduction process: (1) Application of a mechanical stimulus. (2) Fluid displacement is registered by mechanosensors in the cell membrane, transmitting a signal within the cell. (3) Mechanosensors transmit the mechanical stimulus to the cytoskeleton by activating adapter proteins. (4) Adapted products are sent to the extracellular matrix as a response of the cell to gene transcription. (5) New functional, aligned networks are created [100].

2.2.2 Mechanotherapy

Looking at approaches to therapies for wound healing, the therapeutic use of loads to stimulate remodeling and repair of tissues in bones, cartilages, muscles and tendons has been identified as a promising one [96]. Cells are sensitive to physical stimuli, such as elasticity, geometry and force, changing their morphology, physiology, regeneration and tissue functions. Mechanotransduction is the process in mechanobiology that studies how traction forces generated by those extracellular factors can affect biological processes such as metastasis, angiogenesis, cell proliferation and extracellular matrix (ECM) production [112] (Fig. 2.2). It represents an alternative to the implantation of scaffolds seeded with cells from tissue engineering as it avoids undesired tissue properties, immunogenic response or premature death of the cells caused by synthetic scaffolds [43]. Thanks to its capabilities to shape cells and tissues by traction forces, it is possible to modify complex structures in tissues such as the epithelium [112]. The concept of mechanotherapy comprises interventions by mechanical means, not only at physical therapy level as performed in rehabilitation and exercises, but also at tissue, cellular and molecular levels [83]. Thanks to its efficacy in treating and preventing pathological scars and promoting tissue lengthening, mechanotherapy has been used, for example, in burn healing [61], grafting [35], scarring treatment [1] and esophagus elongation [67].

2.2.2.1 Current Challenges in Mechanotherapy

Current challenges for mechanotherapy include: (1) specificity: mechanical stimulation (amplitude, frequency and duration) should be applied in a specific manner to different cells as mechanosensitivity vary depending on their type. (2) Selectivity: cells interact

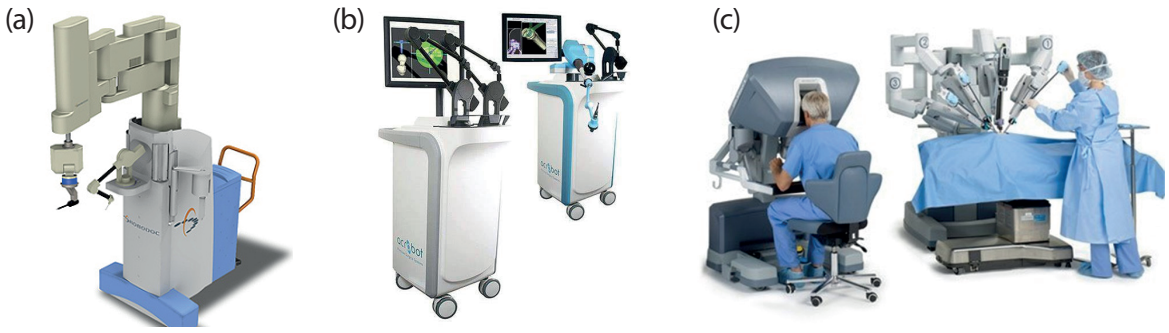

Fig. 2.3: Surgical Robotics. (a) Robodoc, an example of active surgical robot. (b) Acrobot, an example of semi-active system. (c) da Vinci, an example of master-slave system and the most popular surgical robotic system in the last decade. All images are under the Creative Commons licence.

with each other, action that may cause 'noise' making it challenging to distinguish specific signals. This makes it difficult to address specific cell targets for stimulation. (3) Timeliness: mechanotransduction should be applied during a predetermined period, under controlled dynamics to avoid damaging tissue by over stimulation [83]. These challenges remain, as the effectiveness of mechanotherapeutic procedures depends on the surgeon or therapist's haptic and visual assessment and feedback provided by imaging technologies such as x-rays. Additionally, it is unknown how regeneration of tissues develops during long-term mechanotherapies [40]. Therefore, a tissue repair strategy that provides controlled, informed, automated and localized mechanotherapy would overcome these challenges.

2.3 Robot-Assisted Surgery

Medical robots have been of interest to academics and professionals for more than fifty years [55] due to their accurate sensing, diversity of motions, precise monitoring and control. From orthopedics [101] to neurology [12], robotic technology has shown to be capable of assisting in the medical field, making it possible to foresee a near future where medical robots are inherent to the development of healthcare applications, such as in surgical procedures.

2.3.1 Surgical Robots and Minimally Invasive Surgery

Surgical robots are rapidly becoming a new standard in healthcare thanks to constant developments in technology and adaptations to laparoscopy devices [107]. These systems are capable of performing minimally invasive procedures, which reduce patient discomfort, pain and recovery time [69]. Surgical robots can be classified according to their level of autonomy as follows:

Active: system that performs pre-programmed tasks completely autonomously under supervision of the operative surgeon. Examples of active systems include Probot, a surgical robot that performed transurethral resection of the prostate (1995) [77] and Robodoc, first active system to obtain approval of the U.S. Food and Drug Administration (FDA) [107] (Fig. 2.3 (a)).

Semi-active: systems in which the surgeon complements the pre-programmed performance of the robot. Examples of semi-active systems include Acrobot, a haptic system that guides the surgeon's hand following a pre-operative planned path boundary [18] (Fig. 2.3 (b)) and RIO, a guided system for total hip arthroplasty [54]. Although there is scarse evidence of active systems' feasibility, they are often more accepted by surgeons than active systems [194].

Master-slave: systems without a programmed function or autonomous elements that depend entirely on the extra-corporeal surgeon performance, such as hand movements transmitted to a laparoscopic instrument to produce a motion intra-corporeally. An example of a master-slave system is da Vinci®, the surgical robot that has dominated the field for over a decade [107] after being used in a large number of disciplines, such as urology, pediatrics and head and neck surgery, taking advantage of its microsurgery potential [3] (Fig. 2.3 (c)).

Because they typically interact with the human body, a highly dynamic and unstructured environment [44], surgical robots present big challenges such as scalability, autonomy, compliance in *in vivo* behaviour and long-term multi-functional adaptation. Nevertheless, surgical robots have demonstrated to interact in a safe manner with organs and tissues, reducing hospitalization time and presenting no intraoperative complications [105].

2.3.2 Robot-Assisted Tissue Repair and Reconstruction

In the field of tissue repair and reconstruction surgical robots have demonstrated a number of advantages over traditional methods such as manual topical interventions [216]. Some examples of surgeries that have benefited from these technologies include: (1) microsurgery, where micro-vascular anastomosis and reduction of tissue edema were achieved [93]; (2) breast conservation and augmentation, where reconstruction was possible to be completed in one stage under minimally invasive procedures [204]; (3) assisted flap or tissue cutting, where tissue was selected and manipulated accurately, reducing trauma and scarring [177, 116].

2.3.3 Limitations of Surgical Robots

Despite their significant advantages in performing precise procedures with minimal incisions and fast postoperative recovery, surgical robots have shown several problems. They have

demonstrated to produce a shorter survival time in tumor surgery than traditional surgery [163]. Additionally, the U.S. FDA has reported that surgical robots have caused 550 out of 100,000 accidental deaths in robotic-assisted surgeries performed between 2000 and 2013, showing higher incidence than in traditional surgery for some areas, such as head and neck surgery. The U.S. FDA has also reported video jam, machine parts failure and internal ignition of the machine. Additionally, current surgical robots are bulky and expensive machines that need the constant presence of surgeons to operate them from outside the body with complex interfaces, compromising accuracy and precision for some applications [216]. Robots for minimally invasive surgery can also be classified depending on the ports types needed to access the body. Single-Port Laparoscopic Robots (SPLRs) have shown to require large operation space, to have a limited field of view and collision with organs, which represent a serious risk for the patient. Multi-Port Laparoscopic Robots (MPLRs) require multiple wound openings to access the body and Robotic Needle Insertion Systems (RNISs) have shown needle and human tissue deformation. This field can further see advancement by tackling the resilience of the technology.

2.4 Robotic Implants

Robotic implants are a recent class of medical devices, intended to replace body parts [160], monitor body functions [109], provide support to organs and tissues [209] or deliver medication [110]. They could be placed permanently or temporarily on the surface or inside the body [211]. Robotic implants can combine load-based therapies with the precise control of robots to provide mechanostimulation under controlled forces and displacements in order to promote cell proliferation, constituting a promising alternative to tissue engineering and robot-assisted surgery. Some of the drawbacks of traditional implants are infection risk during implantation, pain and swelling at the surgical site. Additionally, they are designed to work under pre-programmed regimens that make it difficult to accommodate therapeutic and patient needs variation such as in pacemakers [39]. Other risks include, similarly to surgical robots as discussed in previous sections (Section 2.3.3), that during a long-term therapy, the implant could stop working properly, move or break, requiring surgery to repair or replace the device [211].

These active implantable devices contain electronic components; therefore, they need to be isolated from the body. Currently, non-toxic and biocompatible encapsulation and its hermetic seal remains a challenge [73]. Also, the lack of integration between long-term technologies and monitoring of the implants function presents difficulties in identifying malfunction [209]. Finally, two recurrent drawbacks in the use of implants are a foreign

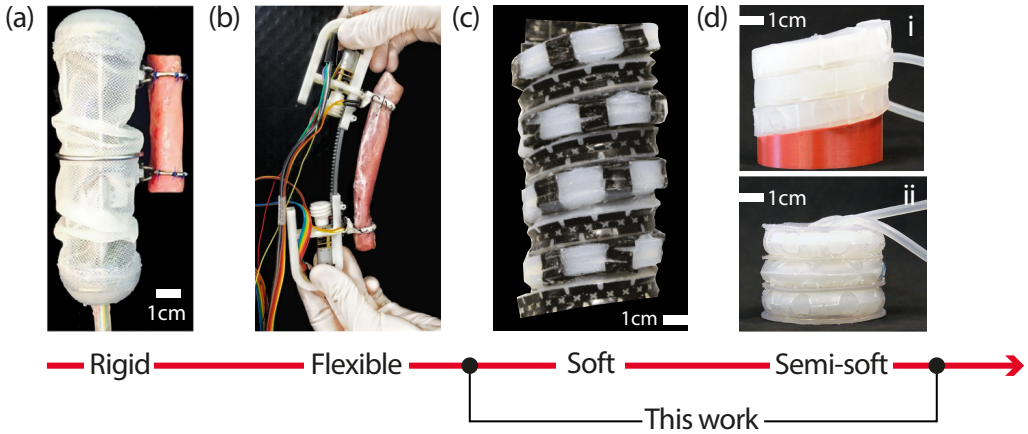

Fig. 2.4: Robotic Implants for Tissue Regeneration. (a) Hard (From [43]. Reprinted with permission from AAAS), (b) Flexible (Reprinted from [10], © 2011 IEEE), (c) Soft (Reprinted from [155], © 2011 IEEE) and (d) Semi-soft approach. i and ii show a helical and toroidal configurations of this approach.

body reaction that leads to a fibrotic response and encapsulation of the device by collagenous connective tissue [217] and their possible breakage during treatment in a difficult-to-access place. Fibrotic response was previously described in Section 2.1.

2.5 Robotic Implants for Tissue Regeneration

Recently, a series of robotic implants for tissue regeneration in the GI tract were proposed by our group (Fig. 2.4 (a,b)). These devices can be classified according to their material constituency and compliance as hard and flexible robotic implants. D. Damian, et al (2018) [43] designed, fabricated and tested *in vivo* an implant capable of lengthening tubular organs by applying traction forces of $\sim 2.5N$ in a controlled manner while maintaining full geometry and organ functionally (Fig. 2.4 (a)). This overcomes the limitations of tissue engineering techniques in which only sections of the esophageal wall or circumference were successfully reconstructed (Section 2.2.1). Moreover, patient sedation and immobilization during treatment required in traditional methods were no longer needed (Section 1.1.3). Additionally, the system was capable of sensor monitoring the procedure in real-time, including lengthening of the tissue and possible malfunctions, allowing the surgeons to adapt or stop the therapy if needed, avoiding risk of tissue tear. The results show 77% of esophageal growth, from which 63% corresponds to muscular cells proliferation (tissue regeneration) and 37% to collagen formation (tissue replacement). As aforementioned, that collagen formation or fibrotic response occurred due to the interaction of the rigid parts of the implant with the surrounding tissue. Given that vascularity is not remodeled in collagenous tissue it was the

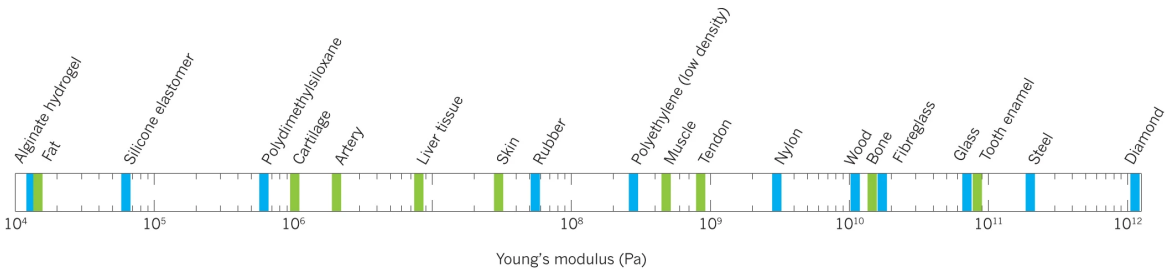

Fig. 2.5: Approximate Young's modulus of selected engineering and biological materials. Since stiffness of materials that conform soft robots is comparable to the ones in tissues and organs, they are a promising solution to the reduction of fibrotic response to implantable devices [29] (Reprinted from [173] with permission, Springer Nature 2012).

next challenge to decrease the amount of fibrotic response and increase the percentage of muscular cell growth. At the moment of starting this work, to the best of our knowledge, this was the only robotic implant for tissue regeneration via mechanostimulation in the literature, setting the baseline for future developments within its scope. Although each of the independent fields that shape the interdisciplinary approach used in work has notably advanced, there has not been other examples of soft robotic implants for tissue regeneration at the time of writing this thesis.

In an effort to advance that design by decreasing inflammation and fibrotic response and to enhance the implant-tissue therapeutic interaction, our group designed, fabricated and tested a flexible version of the aforementioned hard approach (Fig. 2.4 (b)). This robot presented two important contributions: (1) a flexible rack design, which geometry and mechanics are considered by its control system to apply precise and controlled tension to a tubular tissue while reducing self-damage and the forces applied to its surroundings [10]; (2) a symmetric redundant design that provides an effective fault-tolerant control, reducing fault risks by at least 83% [14]. This flexible robotic implant is capable of exerting up to $4N$ of force, which is superior to the force needed to grow esophageal tissue as demonstrated by the hard robotic implant. Although this implant was not tested *in vivo* yet, its compliance to deflections of up to 3 cm represents a promising strategy to decrease fibrosis. Nevertheless, despite having flexible components they are still relatively rigid, potentially not able to address fibrotic response optimally.

2.6 Soft Robotics

Looking at approaches to provide new implants with safe tissue-robot interactions, soft robotics have demonstrated to be a promising strategy. Soft robots are compliant devices made

of materials with mechanical properties similar to those of living-organisms (Fig. 2.5) that are capable of sensitivity, agility and adaptation that are not possible to obtain by their rigid counterparts [173]. The interest in soft robotics has grown rapidly within the robotics field as evidenced by its advancements reported in academia and their progressive involvement in society and industry [16]. Although hard materials can be fabricated into compliant and flexible structures, most of hard robots lack of adaptability and safe interaction with tissues, two important requirements in current developments, where it has been foreseen a closer relationship between robots and humans to perform intricate tasks [72]. To successfully achieve these new complex interactions the field of soft robotics focuses on the design of safer and more adaptive robots than conventional hard robotics [219]. In the robotics community, the word soft usually relates to the mechanical compliance in a system [160], often made of elastomeric materials such as silicone rubbers [118]. Popular examples of these are Ecoflex, Polydimethylsiloxane (PDMS) and Elastosil [134] which present different mechanical properties and are selected depending on the design requirements. Examples of applications made of silicones are a soft-matter sensor to measure pressure deformation and shear force [165], a multigait soft robot [178] and a rehabilitative soft exoskeleton for rodents [66]. The main reason of using these materials is that they are capable of continuous deformation at low pressures, which allow soft structures to yield a wide range of motions, limited only by their mechanical properties [87]. In this work, we use these materials because for internal soft tissues it is important that implants are soft and have a compatible mechanical compliance to reduce inflammation and foreign body reaction. The use of such materials also presents a range of limitations [72, 125, 179]:

- Their elasticity determines the amount of actuation force they are able to exert.
- Sharp objects and high temperatures may damage soft materials, affecting their capability to accumulate pressure and therefore reducing functionality.
- Recurring actuation leads to aneurysms, which means bulging and breakage of the internal walls, driving to failure.
- It is a challenge to optimise and simulate actuators based on elastic materials due to their nonlinear stress-strain characteristics.

A number of efforts have been made to overcome these limitations including shell-reinforcement approaches [146], self-healing techniques [201] and morphological analysis strategies to prevent mechanical damage on soft actuators [125] respectively. It is also common to find soft robotic applications that employ composite materials by mixing, assembling or embedding substrates with different rigidity to exert higher forces with low

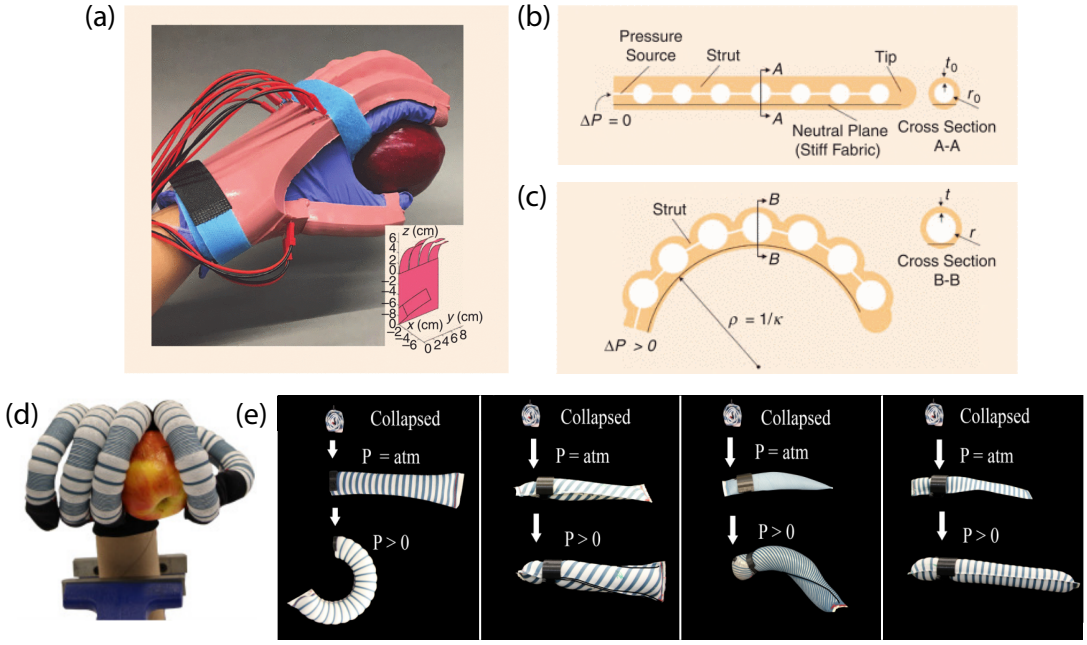

Fig. 2.6: Examples of Fluidic Elastomeric Actuators (FEAs) emulating the working principle of a human hand, following different design methods: (a) Soft hand orthosis made of multi-chamber ribbed FEAs, (b) its FEAs in rest and (c) bending equilibrium state [230]. (d) Soft robotic hand fabricated out of fabric-reinforced FEAs and, from left to right, (e) its bending, twisting, bending-twisting and extending motions [139]. All figures reused with permission, © 2011 IEEE.

elastic modulus materials such as polyethylene and shape memory alloys [179, 173]. Other materials, such as gels and hydrogels, ionic polymer–metal composites, conductive polymers, carbon nano-tubes, graphene, dielectric elastomers, shape-memory and bio-polymers have also been reported to be used in the development of soft robots. However, materials actuated with traditional technology, such as pneumatics and hydraulics have shown to exhibit the best trade-off in efficiency and strain under the lowest power density requirements. These properties make them suitable to act as medical devices [98] such as implants. Therefore, the following sections will be focused on Fluidic Elastomer Actuators (FEAs), devices that employ elastomeric matrices and fluids to achieve motion.

2.6.1 Design

The development of a wide range of soft pneumatic actuators have been critical for the rapid growth of the soft robotics field. One of these actuators are FEAs, a highly expandable and low-power consumption type of soft actuators that are made of elastomeric matrices that deform isotropically when pressurized pneumatically or hydraulically [81]. Their internal network morphology could be pleated, cylindrical or ribbed [122] and their compliance may

vary in relation to the pressurization inside their channels [160]. By combining materials with a different stiffness of that of an elastomeric matrix and making them interact, FEAs can be programmed with directionality through anisotropic expansion of its fluidic channels to perform motions [87]. If an FEA is fabricated using only an elastomeric matrix the channels contained within the actuator will expand in the most compliant region upon pressurization. The motion path followed by the actuator depends on how anisotropy is programmed within the structure, classified as bending, twisting, contracting, expanding and extending [72]. Two or more of these motions can be found combined in one actuator by for example, assembling modular sections that are pressurized independently to achieve complex movements [37, 225]. Typically, anisotropic expansion is programmed within the FEAs structure following two approaches, ribbed multi-chamber Soft Pneumatic Actuators (SPAs) [195] (Fig. 2.6 (a-c)) and fiber-reinforcements [161] (Fig. 2.6 (d,e)). The use of a "rib" or inextensible layer within the FEAs body is also used in fiber-reinforced FEAs, as it enables the actuator with bending motions. These actuator types are very popular among soft roboticist due to their simple fabrication, which consists of wrapping fibers around a silicone chamber to exert pre-programmed motions [37]. Therefore, their design versatility and potential to produce and combine motions make FEAs suitable for the development of implantable devices that require to be multi-functional.

2.6.2 Fabrication

Traditional robots made of hard components are difficult to customise and costly to fabricate as they require specialised manufacturing and assembly processes [144]. In the field of soft robotics, some of the most important factors that have contributed to its advancements are the development of sophisticated fabrication tools and digital design. From multimaterial 3D printers to soft lithography, soft roboticists combine different techniques to create compounds of expandable chambers and embedded electronics [173]. Additionally, the versatility of designs that soft robotics are able to reproduce makes possible the combination of digital and analogue techniques to fabricate complex structures. An example of this is an organ shaped FEA made of poroelastic material by traditional forming techniques such as sculpting, sheet cutting and casting [119]. Soft robotics has also benefited from manufacturing processes widely used in other fields, such as injection and extrusion from thermoplastics [160]. The following are fabrication techniques commonly used in the soft robotics field:

Digital Additive Manufacturing: single material 3D printing has been widely used to create molds to cast soft substrates and structures, such as soft robotic tentacles [123]. Multi-material 3D printing has contributed to the development of composites

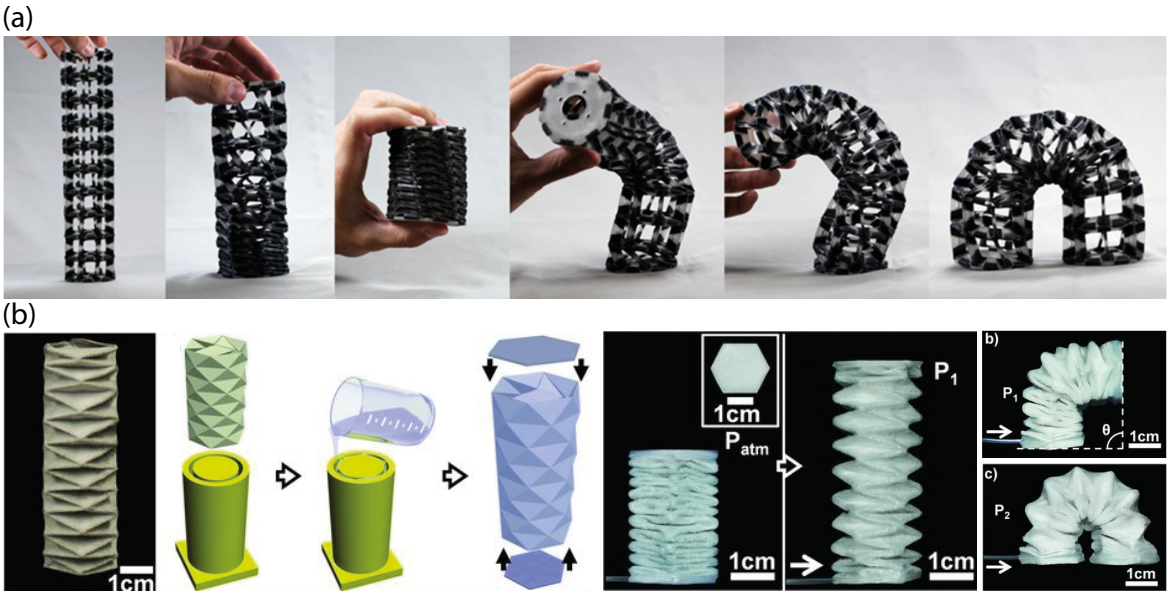

Fig. 2.7: Examples of two similar soft origami tower systems fabricated under different soft robotics manufacturing methods: (a) multi-material 3D printing [115] and (b) 3D Molding [124]. Both figures reprinted with permission: (a) © 2011 IEEE and (b) Copyright, 2012; John Wiley and Sons.

with different substrates and hence different mechanical properties within the same structure [89] (Fig. 2.7 (a)) and even 3D co-printed solids and liquids simultaneously [120]. Additive manufacturing is a quick, commercial solution to obtain customizable parts in a relative short time that has been used widely to print hard robots and now 3D printing has become a common technique for soft robots fabrication. Its limitation is that it is not possible yet to integrate mechanical, structural and electrical components in a fully functional monolithic structure [144].

3D molding: is a casting process in which the volume of an elastomeric structure is defined by the mold walls, being its main constraint the demolding step of intricate shapes [72]. Molds can be created either by additive manufacturing as 3D printing, assembling rigid substrates such as acrylic or by micro-machining (Fig. 2.7 (b)). This is a commonly used fabrication technique that has been employed to manufacture from wearables [4] to edible robotics [181].

Soft-lithography: is a fabrication approach that is typically combined with 3D printed molds based on replica molding, using a layer of flexible material, usually with a more rigid material embedded in the structure to achieve anisotropy after actuation [173]. It can also be done by spin coating, which consists on applying uniformly fine layers of soft material on a plane by distributing it homogeneously using centrifuge force

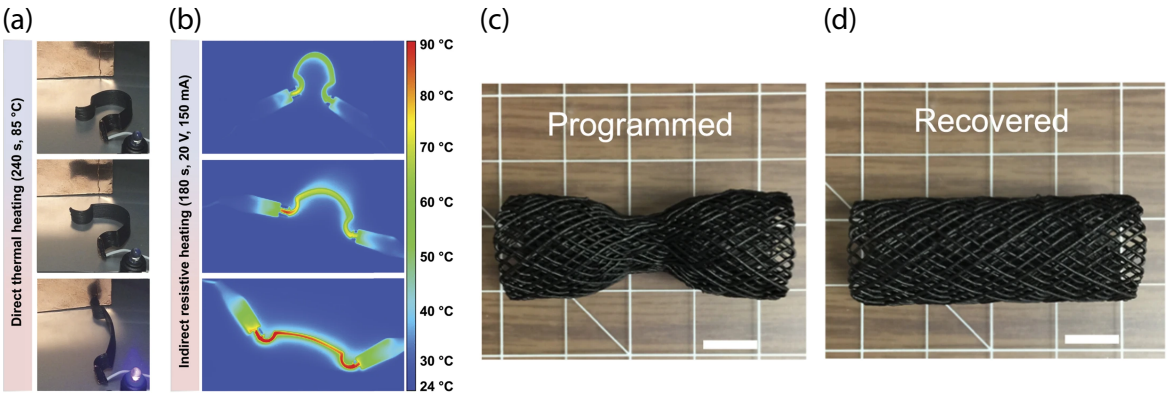

Fig. 2.8: Shape-morphing actuation principle employed in SMAs, SMPs and DEAPs: (a) Composite made of carbon-nano fibers embedded in elastomer and (b) thermal images showing how it changes its programmed shape by heating it to 80^oc. (c) Programmed and (d) recovered 3D printed stent after applying direct thermal actuation [168]. All images reproduced with permission, Springer nature 2016.

[71]. Soft lithography allows the possibility of fabricating micro and nanostructures, ranging from 30 μm to 500 μm [223].

The use of conventional tools to cast, cut, stamp or roll soft substrates manually into specific configurations gives soft roboticist an advantage in the fabrication of inexpensive models and prototypes in comparison to their rigid counterparts. However, those traditional techniques are time-consuming and add complexity if, for example, multiple molding steps are needed to build a structure or if graded materials should be embedded [120]. Additionally, these elaborate fabrication processes add involuntary stresses and defects into the actuators body due to human error [153], which should be particularly considered if the end application is a implantable device. This will be further discussed in Chapter 4.

2.6.3 Actuation

Soft actuators are the building blocks of soft robots that enable their motion. Currently, most of them are actuated fluidically and fabricated out of elastomeric matrices with embedded rigid or semi-rigid materials [97] as described in Section 2.6.1. However, since soft robots can be built by combining different types of actuation methods, it is relevant to review alternatives to FEAs powered by hydraulics and pneumatics.

Shape Memory Alloys (SMAs): a class of smart materials that, despite not being soft, they can be compliant if fabricated out of thin wires or coils, which is their typical representation. SMAs work under two phases, martensite and austenite. They

enter into the austenitic phase when subjected to certain stimuli, such as magnetic fields or heat, changing their morphology [226] (Fig. 2.8). Their light-weight bodies, super-elasticity and shape memory property make them a versatile material that have been used in various fields such as aerospace and in biomedical applications [24].

Shape Morphing Polymers (SMPs): thermo-mechanical actuators that relax and re-contract when heat is applied and removed respectively. They are inherently compliant as they are shaped out of polymers. SMPs have a larger recovery strain and stress than SMAs of $\sim 300\%$ and $\sim 1GPa$. Since they can be fabricated out of biocompatible materials, they can be used in biomedical applications such as orthodontics, neuro-prosthesis and Bio Micro-Electro-Mechanical Systems (Bio-MEMS) [182].

Dielectric-Electrically Actuated Polymers (DEAPs): DEAPs are inherently compliant as they are manufactured out of hyper-elastic membranes and stretchable electrodes. Thanks to their lightweight body and configurable membranes, these actuators have been used as stacked, folded, rolled and coiled structures to increase their output capabilities such as force [30]. However, the pre-stretching rings or any rigid structure around them may cause the increased stiffness. DEAPs support light-weight structures, however they have the limitation that, due to the high-voltage circuit used to actuate them, they should be placed away from the robotic platform.

Magnetic/Electro-Magnetic Actuators (E/MAs): E/MAs are elastomeric membranes that contain a flexible coil or ferro-magnetic particles embedded in their compliant structure [99]. Since they need remote regulation of magnetic fields, depending on the application, the actuator should be free from magnetic disturbances to operate correctly.

Active materials such as SMA and SMPs that can convert different forms of energy such as thermal, chemical, optical, electrical or magnetic into mechanical work can be used in combination with other substrates to create deployable structures, becoming an appealing alternative to fluidic actuators [180, 152]. However, they also show some limitations. SMAs are limited by their inability to reproduce motions due to their high hysteresis behaviour and their limited work-range. SMPs are only able to perform under one-way actuation, their complex fabrication, control systems and energy conversion are highly inefficient as they depend on heating processes to be actuated [24]. DEAPs need for amplification of voltage requirement, challenges in actuation force levels and durability make them unsuitable for the medical and industrial robotics fields [17]. E/MA soft actuators are a novel approach that have not been tested in a number of settings, making them the lowest in their technological

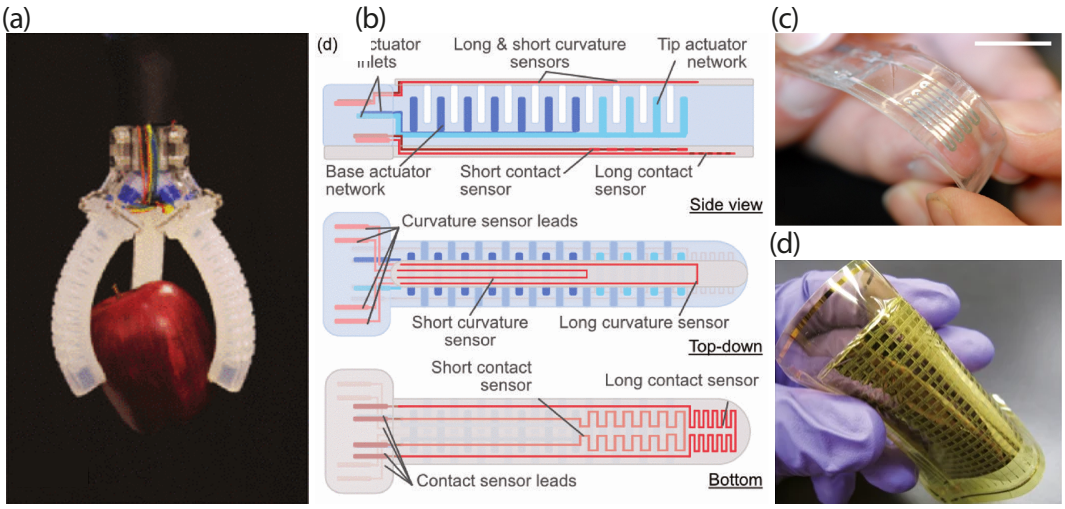

Fig. 2.9: Different sensing technologies. (a) Soft robotic fingers (b) with embedded ionogel to provide proprioceptive and tactile sensing corresponding to each degree of freedom [208]. (c) Differential multi-mode sensor showing its liquid-metal-filled microchannel embedded in a elastomeric substrate [220]. (d) A low-voltage macroscale e-skin made of a nanowire active-matrix circuitry [198]. Figs. (a,b) reproduced with permission, © 2011 IEEE. Fig. (c) is reprinted with permission from Copyright © 2011 Elsevier Ltd and Fig.(d) Copyright 2010 Nature Publishing Group.

readiness level in comparison to the previously described types of actuation [24]. On the other hand, FEAs have demonstrated to have the highest technological readiness level, thanks to their relatively easier manufacturing, high scalability (Section 2.6.2), low pressure requirements and back-drivability that makes them ideal for human-robot interaction [134], giving them a clear advantage over the previously described actuation methods to be used in medical applications such as implantable devices.

2.6.4 Sensing

Thanks to the suitability of soft robots to be used in healthcare applications there is a clear need for sensing strategies that can be embedded into these technologies without compromising their functions [104]. Although it is common to find hard sensing components as part of soft robotic systems [230, 33, 203] many commercial and conventional sensors are precluded to be used in soft robotics due to their lack of compliance. Hyper-elasticity of soft materials imposes technical limitations, even to flexible sensors based on piezoelectric polymers, making them unsuitable to be used in a system that require stretch and bend [173]. In response to this challenge, polymer materials, such as silicone rubbers, have been used in the design of novel soft sensors (Fig. 2.9 (a,b)). Nevertheless, their non-conductivity make them rely again on non-flexible materials, limiting their stretchability.

To overcome these challenges, one of the most commonly used sensing strategies in soft robotics with high-stretchability is the use of piezoresistive sensing materials. These are elastomeric matrices with embedded conductive particles such as carbon black or carbon nanotubes. Their acceptable dynamic performance defined by high sensitivity and fast response, easy manufacture and extensive wearable applications make piezoresistive elastomer matrices suitable candidates to be used in the development of soft implantable devices [187].

Another approach has been to embed microchannels in soft structures to encapsulate conductive liquid (Fig. 2.9 (c)), using this medium's continuous property and their ability to detect curvatures, strain, pressures and multi-axis shear forces [170]. Hydrogels are optically transparent, biodegradable and biocompatible, as well as inexpensive to fabricate, showing potential to be used as a conductive liquid [160]. Ionic liquids have also showed satisfactory biocompatible behaviour, despite their limited conductivity. Biocompatible sensing skins use electrical impedance tomography to detect location and magnitude of surface contact [34]. Soft optical sensors are an alternative to microfluidic sensing, as they detect changes in a hyperelastic structure through a light transmission that passes by a reflective waveguide [203]. Advancements in new materials, microfabrication and modeling principles are driving the development of more flexible electronics that are also contributing to the creation of new sensing technology such as E-skins [117] and soft palpatory pulse-rate devices [33] (Fig. 2.9 (d)). Other examples include flexible pressure sensitive rubber membranes [185] and pressure sensors made of nanopatterned elastomers for enhanced repeatability and sensitivity [148]. However, these still face limitations such as not being able to measure pressures bellow 10 kPa [85]. As described in this section, there is a wide range of approaches that aim to provide hyper-elastic substrates with sensing capabilities, being the use of microchannels to encapsulate conductive liquid and piezoresistive sensing materials two of the most promising to be integrated in the skin of soft implantable robots [90].

2.6.5 Modeling

As a consequence of their continuous function, intrinsic compliance and passive degrees of freedom, soft robots show more complex dynamics and kinematics than conventional hard robots, making modeling a persistent challenge to date (Fig. 2.10 (a-d)). First, continuum robots date back from 1960s [218], and since then, the literature scarcely shows any work proposing an approach towards modeling and holistic design guidelines. Consequently, the research in soft robotics field is mostly driven by experimentation rather than simulation and modeling, which becomes more complex given the diversity of designs and their specific modeling challenges [172].

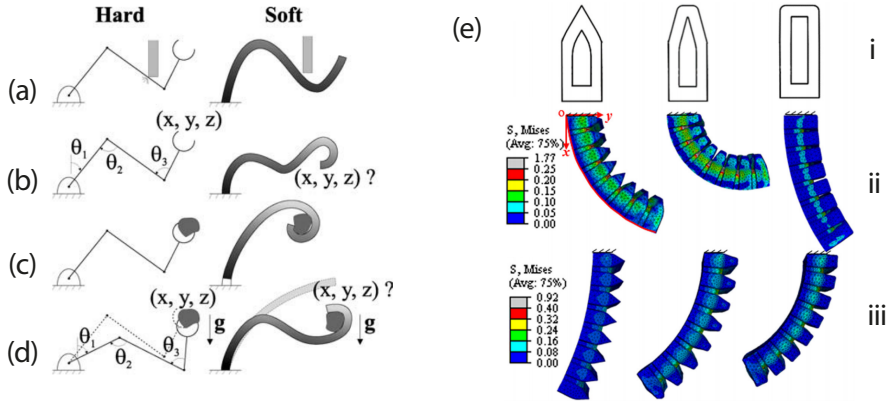

Fig. 2.10: Comparison of the capabilities of hard and soft robots in terms of (a) dexterity, (b) position sensing, (c) manipulation and (d) loading [207] (Open Source).(e) Typical numerical modeling using the Finite Element Method to analyze, predict and optimize design features in a system. i shows the schematics of the cross-sectional geometries of FEA chambers; ii and iii show the analysis of the maximum bending angles deflated and inflated respectively, using the geometries in i [76]. Fig. (e) used under the Creative Commons licence.

In a recent publication, O'Reilly and Payrebrune [47] contrast the freedom that soft robotics provides to develop a wide range of versatile designs against their analytical and computational complexity. In an attempt to mitigate the problems caused by this trade-off, the authors proposed a five-parameter constitutive relation for a rod-based model of a widely used, pneumatically actuated soft robot arm [48]. This was then used as a base for a four step framework to automate the design and modeling of soft robotic systems [172]: (1) design and parametrization, (2) finite element analysis, (3) kinematic modeling using a Piecewise Constant Curvature approach and (4) machine learning of the kinematic model. However, impact of gravity and external loads were not considered in the framework, which might decrease the reliability of this method in soft robots that undertake loading tasks. Other approaches used for the modeling of soft robots different to the ones using continuum rod theory are minimum potential energy, beam theory [75], and screw theory [74]. Although these do not reflect the hyper-elastic behaviour of the material that shapes soft actuators, they represent a useful tool for preliminary prediction of the capabilities of soft systems [153].

One of the limitations of current approaches for modeling continuous function in linear soft structures is the analysis is not made holistically, but only localized [173]. Simulations can be of help to approach modeling of complex soft robots more holistically. When performed by simulation, soft roboticist typically use Finite Element Analysis [48] (Fig. 2.10 (e)), method that has demonstrated to be very effective in modeling soft robots motions [134] and to being able to replace time-consuming experiments [47]. However, finite element simulations present the limitation of having a high computational cost [74]. Nevertheless,

finite element simulations have demonstrated to be effective in predicting *in-vivo* response to mechanical stimuli following continuum mechanics theory [233], making them suitable to design and model tissue-implant interaction.

2.6.6 Control

Control is critical for the development of robotic implants in order to avoid harming the target organ or surrounding tissues during treatment. The motions of hard robots are described within three translations and rotations on the x, y and z axes, which sum six degrees of freedom. Control kinematics and dynamics of some compliant systems, such as continuum robots, are challenging to model due to their intrinsic structural complexity. Recent efforts have been made to develop more robust control for continuum robots, such as an interval arithmetic approach and adaptive algorithms [82] achieving a performance improvement.

Nonetheless, due to their elastic and hyper-elastic capabilities, and because they are able to bend, compress, twist and wrinkle, soft robotics motions cannot always be restricted to be described to planar movements. Therefore, it is stated that soft robots have the capability of offering infinite degrees of freedom, which represent a challenge for their control [2]. On the other hand, their uncertain geometry is the basis for new control algorithms, such as soft robots that grasp objects successfully without accurate positioning [173].

A requirement for the reliable control of forces and motions of soft robots is their combined performance with soft sensors. Examples of this include the use of flex-sensors to predict the bending angle of an FEA [60] and the use of a prioperceptive flexible fluidic actuator using conductive working fluids [79]. Moreover, the control strategy selected will be defined by the challenges and requirements imposed by the actuation type (Table 2.1), driving systems and controllers [214].

The Proportional-Integral-Derivative (PID) controller is one of the most used control systems in current soft robotics developments due to its simplicity and ability to keep a constant variable through a control loop and feedback. This control system works by using a microcontroller that allows communication between the soft robot and a PC using a software interface [214]. Despite its non-linearity and abrupt overshoots, the PID controller's versatility is a promising choice to control soft implantable devices.

2.7 A Soft Robotic Implant?

In recent years, there has been an increasing interest for the development of medical robots and their components using soft and semi-soft based approaches [8, 176]. However, most of

Table 2.1: Control challenges for different actuators types. Reproduced with permission [24]

Actuator	Control Challenge
SMA	Hysteresis, slow response time.
FEA	Non-linear behavior of pneumatic modality due to compressibility and dependencies on temperature.
SMP	Non-linear and often unidentified behavior, non-linear dependencies on temperature.
DEAP	Electrical break-down limits, mechanical strain limits, durability, extra need for signal conditioning and amplification
E/MA	mm-scale dimensions, magnetic interference

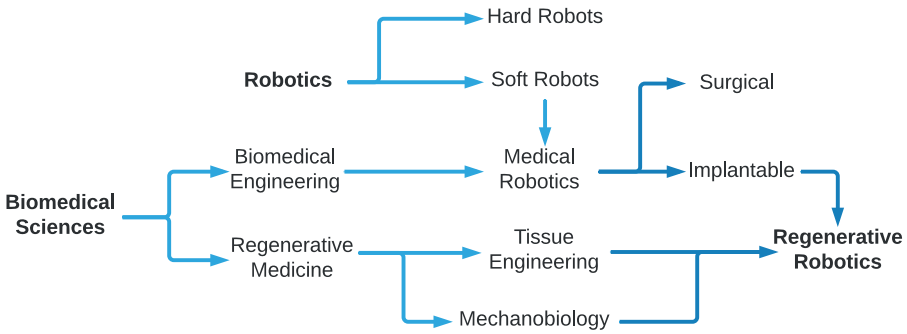

Fig. 2.11: Diagram showing the disciplines involved in the design approach used in this work.

these technologies have been focused on wearables [25] that work outside of the body [151] and devices for minimally invasive procedures [171], particularly endoscopic tools [186] and catheters [103]. The majority of soft robotic implants have focused on treating heart failure [167, 174], however, tissue repair can benefit from the compliance and mechanical support that soft robotic implants can provide.

By encoding the principles of regenerative medicine and tissue growth (Section 2.2) through mechanotherapy into the design of a robotic implant, it is possible to regenerate the tubular organs in the GI tract, as demonstrated by [43], despite their complex set of layers (Fig. 1.1(b)) and metabolic functions, which currently remains a challenge for tissue engineering (Section 2.2.1). The need for specificity, selectivity and timeliness in mechanotherapy (Section 2.2.2) can be met by applying the precise and controlled forces and displacements that the robotics field can provide. The current lack of monitoring and therapy feedback that prevents tissue engineering from successfully growing fully functional organs can also be solved by a robotics approach. The only existing robotic implant for tissue regeneration via mechanostimulation [43] in the literature by the time this work was developed have achieved to fully regenerate an esophageal section, with the disadvantage of producing collagen formation. Recent findings have demonstrated that fibrotic response to medical implants can be reduced and avoided if the surface of the device matches the stiffness of the tissue

where it resides [29], making soft robotics a promising strategy to provide the implants with mechanical compatibility. In conclusion, by embedding robotics and regenerative medicine strategies (Fig. 2.11) into a smart design we developed a series of soft robotic implants for tissue regeneration via mechanostimulation capable of providing long-term reliable tissue therapy that restore organ functions.

Chapter 3

Characterization, Simulation and Control of a Soft Robotic Implant for Tissue Repair

3.1 Preface

In Chapters 1 and 2 we described current therapies for tissue repair in the GI tract, their limitations and how by combining principles of regenerative medicine and robotics into a smart device we are be able to mitigate those limitations. In this chapter, we introduce the design, fabrication, modeling, control and validation of that device, addressing the design requirements of universality, safety, multi-function and controlled operation presented in Section 1.2. The content of this chapter and its appendix has been published in the following research articles and abstract:

1. E. Perez-Guagnelli, S. Nejus, J. Yu, S. Miyashita, Y. Liu, and D.D. Damian. "Axially and radially expandable modular helical soft actuator for robotic implantables". *IEEE International Conference on Robotics and Automation*, 2018 (pp. 1-9). Where E. Perez-Guagnelli and S. Nejus fabricated and characterized the system as well as analyzed the data. J. Yu and Y. Liu performed the numerical and analytical model respectively and S. Miyashita and D.D. Damian co-supervised the research.

2. E. Perez-Guagnelli, J. Jones, and D.D. Damian. "Evaluation of a soft helical actuator performance with hard and soft attachments for tissue regeneration". *In Proc. 12th Hamlyn Symposium on Medical Robotics.* 2019, (pp. 3-4). Where E. Perez-Guagnelli and J. Jones fabricated and characterized the system as well as analyzed the data. D.D. Damian supervised the research.

3. E. Perez-Guagnelli, J. Jones, A.H. Tokel, N. Herzig, B. Jones, S. Miyashita, and D.D. Damian. "Characterization, Simulation and Control of a Soft Helical Pneumatic Implantable Robot for Tissue Regeneration". *IEEE Transactions on Medical Robotics and Bionics*. 2020, 2(1), pp.94-103. Where E. Perez-Guagnelli designed and fabricated the actuator. E. Perez-Guagnelli and J. Jones characterized and validated the system as well as analyzed the data. A.H. Tokel designed and fabricated the physical simulator. B. Jones and J. Jones developed the control approach and N. Herzig and J. Jones developed the analytical model and the validation approach. S. Miyashita and D.D. Damian co-supervised the research.

4. E. Perez-Guagnelli, P. Mitrev and D.D. Damian. "Configurable Soft Tool for Mechanotherapy Based Tissue Repair". *Children's Technology Conference*, 2021. Where E. Perez-Guagnelli designed and fabricated the actuators. E. Perez-Guagnelli and P. Mitrev designed the experiments, characterized the system and analyzed the data. D.D. Damian co-supervised the research.

3.2 Introduction

The impact of soft robots has been seen throughout the medical field, e.g., in assistive technologies and rehabilitation [11], minimally invasive surgery [131], implants [41] and wearables [150]. One of the main advantages of soft robots is their compliance, enabling safe interaction with the human body and thus, increasing the wearability of technologies for the treatment of various clinical conditions.

Tissue repair, in particular, can benefit from the characteristics of soft robots, such as gentle dexterous handling, palpation, anatomical and functional support. As mentioned in Section 2.3, advanced surgical tools, e.g., Da Vinci robots, have demonstrated the benefit of added accuracy and minimizing invasiveness to the surgical procedures for tissue repair. However, surgical robots require supervision during the surgery and provide no further control of the tissue repair beyond the surgical intervention. Alternatively, tissue engineering aims to restore the structure and function of a tissue by stimulating cells to proliferate on scaffolds using chemical growth factors [9] (Section 2.2.1). Despite advances in structural tissue regeneration, tissue engineering faces challenges such as lack of vascularity in new tissue, poor mechanical compatibility, and lack of control of the regeneration process after the scaffold implantation [141]. As mentioned in Section 2.2.2, mechanotherapy has been found to have assistive and therapeutic effects for a variety of medical conditions [83], including tactile sensory restoration [42], wound healing [106], regeneration of skeletal muscle and esophageal tissue [43], bone growth and skin grafts [84, 45].

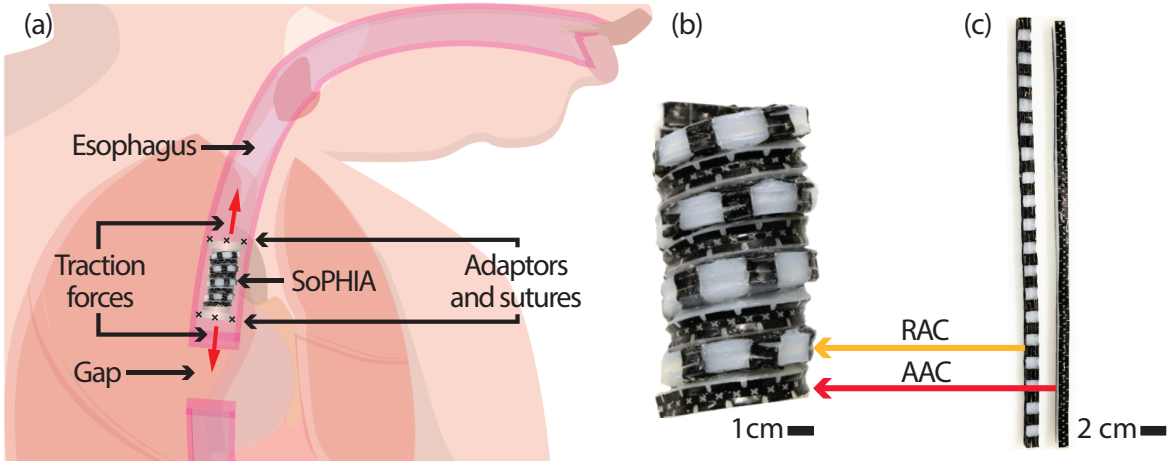

Fig. 3.1: The soft helical actuator for mechanostimulation-based tissue regeneration. (a) The envisaged implantation of SoPHIA inside the esophagus to treat the long-gap condition. It may be attached to the tissue by using sutures and adaptors [154]. (b) A view of the helical actuator made by configuring two actuation chambers. (c) The two chambers, axial (AAC) and radial (RAC) before the helical configuration to stimulate the tissue axially and radially respectively [156].

Robotic implants are a new medical technology with the potential to unify the advantages of mechanical stimulation to tissue repair and regeneration, by exploiting the cells' intrinsic proliferation mechanisms. They also have the potential to engineer and control the process of tissue repair, brought by medical devices, robots and surgical assistance, during the entire duration of treatment via remote communication [40]. These regenerative implants may be deployed inside the body and be mounted on the target tissue. There, they will exert controlled and gentle forces, and elongation on the tissue to induce regeneration and healing.

An example of potential therapies in which robotic implants may be of use is the regeneration of the gastrointestinal (GI) tract. This type of regeneration is required for conditions such as long-gap esophageal atresia (LGEA) (Fig. 3.1 (a)) or short bowel syndrome (SBS), congenital conditions in which more than two-thirds of these organs may be missing [68], and for which current treatments prove suboptimal with high mortality rates [157] (Section 1.1.3). Our group recently introduced a robotic implant that was able to induce growth of esophageal tissue using mechanostimulation and showed 77% of tissue growth over nine days [43] (Section 2.4). This rigid implant was mounted on the esophagus and gently pulled the tissue axially. It was able to apply traction forces in the range of 1-2.5 N and displaced up to 5 cm of tissue [41]. Despite the potential of these robotic implants, the *in vivo* studies also revealed a range of unanticipated challenges due to the fixed design of the implant operating long-term in a harsh *in vivo* environment. Given the interaction between the rigid implant and the tissue, it was ascertained that tissue scar level was significant, 37% of the new tissue, because of collagen formation (Section 2.1).

The derived requirements for mechanostimulation-based robotic implants for tissue regeneration are: (1) mechanical compliance to reduce inflammation [135]; (2) minimally invasive implantation by surgeons in various parts of the GI tract; (3) a design that allows hyperelastic linear deformation while securing anti-buckling structural strength to resist considerable loading; (4) safe control of the delivery of mechanical stimulation.

To address these requirements, we introduced the concept and fabrication of a Soft Pneumatic Helically-Interlayered Actuator (SoPHIA). This multi-modal soft actuator is composed of two pneumatic chambers coiling together into a tubular implant for mechanotherapeutical tissue regeneration (Fig. 3.1 (b-c)) [156]. Due to its helical arrangement and reinforced walls, the soft helical actuator is capable of both axial extension and radial expansion to stimulate the growth and function of the longitudinal and circular muscles of the GI tract. In this work, we present a holistic characterization of the soft actuator's capabilities in the axial, radial, and combined actuation mode, a simulation using a novel *in vivo* tissue growth simulator, control of the SoPHIA as well as the evaluation of hard and semi-soft attachments to fix it to tissue.

3.3 Related Work and Design Requirements

In alignment with the challenges described previously (Section 1.2), a number of technical requirements were defined. First, the actuator should be mechanically compliant with the target tissue. Recent studies in material engineering and tissue regeneration suggest that mechanically compliant implants [135] and the application of mechanotherapy may reduce the inflammatory response of the body [32]. Soft-matter robotic implants would thus be a suitable choice for mechanotherapy-based tissue repair (Section 2.6).

Second, the actuator should be modular, to facilitate implantation, and configurable, to allow its mounting on tubular tissues in a non-invasive or minimally invasive manner. Soft actuators' research has generally focused on pre-programmed axial extension and bending actuation based on fluidic control, for navigation in surgical applications or for exoskeletons [133]. Advances have been made towards modular soft robots for assistive applications [4]. Such devices are highly desirable for non-invasive surgery and implantation as well, yet have not been tested for their reliable extension under sustained loading conditions, as required for mechanostimulation. More recent work has also explored the strength of these actuators with programmable composites, demonstrating the exertion of axial forces to lift up to 1kg after being pressurized at 23.8 kPa, and the expansion of more than 200% their original size [124]. However, the actuator has a large volume due to its origami creases, which is not desirable for an implant that seemingly coats a tubular tissue.

While soft medical devices and implants have been recently proposed [167], more work needs to be done to reduce the implantation invasiveness.

Third, the actuator should elongate with the growing tissue without buckling due to load from the tissue or the body's spatial constraints. As soft actuators' directional expansion needs to be increased, to support large tissue reconstruction, it is critical to have actuators that maintain structural strength and do not buckle under load. The compliance of soft robots is limiting in this regard, making it challenging for them to withstand forces from their environments [13]. Helical or coiled structures are found in both, biology and engineering, due to their ability to handle tension and compression [175], or to provide enhanced maneuverability and stability, for example to endoscopic instruments [70]. When used in soft robotic systems, they also provide increased dexterity, more efficient workspaces by using routed tendons [191], enhanced area of contact and stability when acting as a gripper [210]. Nevertheless, scarce attention has been put into their investigation, especially in soft robotics.

Fourth, a control of the actuator similar to the current clinical treatment is needed. In general, it is difficult to develop accurate models and control of soft actuators [173] due to the diversity in hyperelastic-based material constituents. Recent research has developed a variety of new methods for control, capable of dealing with the increased dimensionality and complexity [6]. One common approach for bending linear soft robots is derived from piecewise constant curvature modeling, based on which classical control strategies can be employed [50]. Despite the promising results, for more complex soft robots, the method is often ill-suited, as the dynamic behavior with the environment is not captured. Apart from these typical problems, overcoming the soft actuator's reliable extension under loading adds new challenges, such as buckling and undesirable bending. Given the gap in control strategies for complex soft robots, we used one of the common approaches of outsourcing some of the control to the robot's morphology and design [59].

In this Chapter, we embed the aforementioned requirements in a helically configurable soft pneumatic actuator that applies controlled multi-modal mechanostimulation. We introduce the following contributions to this area of research: (1) introduction of the concept of coiling soft assembly for realizing deployable, multi-modal, compact, soft yet strong, and adaptable soft robotic implants; (2) modeling and mechanical characterization of a soft helical actuator for axial extension and radial expansion to deliver mechanostimulation to tissue; (3) a physical *in vivo* simulator of the biological tissue's stiffness and growth to allow for the evaluation of the helical actuator's performance; (4) the design of two implant-to-tissue attachments for the evaluation of the effects caused by the functional interplay between the tissue and the mechanical function of the implant; (5) a model-based multi-stage control of the axial extension of the helical actuator according to tissue's physiological response.

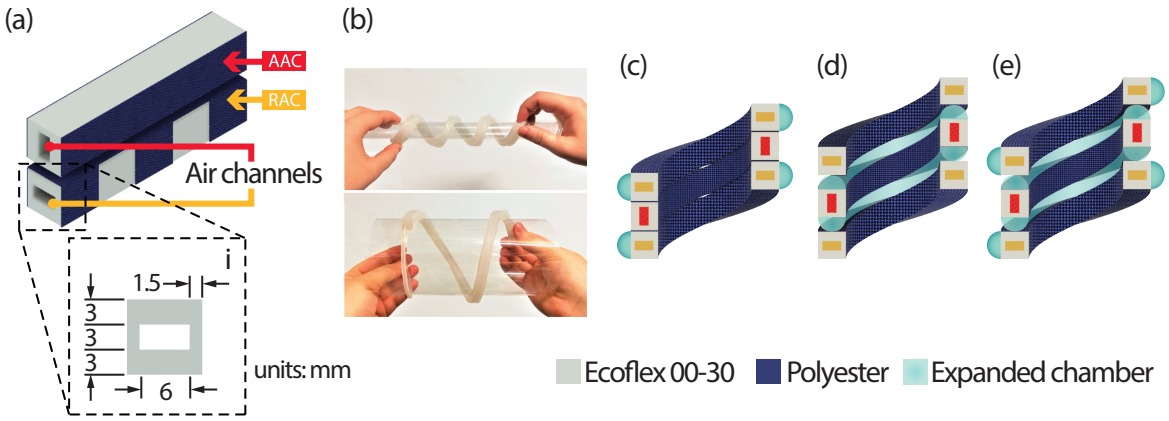

Fig. 3.2: SoPHIA Design. (a) Pneumatic chambers with embedded polyester that constraints isotropic expansion. (b) The pneumatic chambers can be configured into a helix around structures of varying diameter. (c) Cross-sectional view of SoPHIA when the RAC is pressurized (to produce expansion). (d) Cross-sectional view of SoPHIA when the AAC is pressurized (to produce extension). (e) Cross-sectional view of SoPHIA when both chambers are pressurized.

3.4 SoPHIA's Conceptual Design

We designed a soft actuator that is based on the anatomy of the GI tract. Most of the GI tract presents two types of muscle layers with fibers oriented circularly and longitudinally [121] (Fig. 1.1(b)). Therefore, a soft actuator for these organs should apply traction forces to both ends of the muscle layers in order to optimize the quality of the engineered tissue.

SoPHIA is an entirely soft actuator, made out of two identical elastomeric pneumatic chambers; the Axial Actuation Chamber (AAC) and the Radial Actuation Chamber (RAC) (Fig. 3.2 (a)). Each chamber has a length of 48 cm, reaching 10.7 cm of height when the chambers are helically arranged and unpressurized. SoPHIA has a total weight of 95 grams. The chambers are made of Ecoflex 00-30 (Smooth-on Inc.) and can be configured into a helix of different diameters, depending on the tubular organ where it is placed (Fig. 3.2 (b)). They are wrapped in polyester fabric, which in the AAC restricts radial expansion, while in the RAC restricts axial extension (Fig. 3.2 (c-e)). The AAC expands to displace adjacent chambers, increasing the axial size of SoPHIA. The RAC exhibits laterally emerging balloons from the unconstrained sections, yielding radial expansion. These chambers are coiled together into a helical structure with interlayered actuation (Fig. 3.1 (b-c)) and 3.2 (e)). A more detailed description of the conceptual design of the RAC and fabrication of the chambers can be found in Appendix A.1.1 and A.2 respectively. Details on SoPHIA's fixation to *ex vivo* esophagus tissue are described in Section 3.6.5 [154].

3.5 SoPHIA's Analytical Model

In this section, an analytical model of the helical actuator is introduced and validated, to understand the relation between the physical components and their mechanical response to pressurization. We modeled the AAC and RAC separately, given than the two actuation chambers can be decoupled and used independently. By assuming the AAC to displace in a single direction we simplify its model without affecting its main performance metric of axial extension (Fig. 3.3 (a-b)). By assuming the RAC as a toroidal structure rather than helical we simplify its model without affecting its main performance metric of radial expansion (Fig. 3.3 (c-d)). We assume that the two chambers deform uniformly, neglecting fabrication errors that may input heterogeneous expansion and complicate the model. Additionally, we assumed that the coiled chambers behave as a stack of N circular chambers, however the weight of the air and chambers that shape the actuator are neglected for simplification. Finally, we neglect any possible radial force applied by the tissue to the robot in order to match the characterization test presented in Section 3.6. At equilibrium, the force balance equations projected respectively on $\mathbf{e_x}$ and $\mathbf{e_r}$ (Fig. 3.3) can be written as:

$$P_x S_x - F_{ex} - F_t = 0 \tag{3.1}$$

$$\int_{\theta_1}^{\theta_2} hP_r R d\theta - \int_{\theta_1}^{\theta_2} w\sigma_{er} R d\theta = 0 \tag{3.2}$$

where F_{ex} denotes the resistance force of the elastomeric walls to expansion along $\mathbf{e_x}$, F_t is the resistive force of the host tissue during the mechanotherapy treatment, P_x and P_r are the relative pressure of the air inside the air channels of the AAC and the RAC respectively. S_x is the cross-sectional area of the air channel of the AAC, h denotes the height of the air channel of the RAC, w is the thickness of the RAC walls and R is the external radius of the RAC, $\sigma_e r$ is the elastic stress of the expanded wall in the radial expansion of the robot, θ_1 and θ_2 are the angular limits of the area considered for the force balance equation, and finally $d\theta$ is the angular differential for the integration.

Silicone rubbers are hyperelastic materials. Using a Neo-Hookean model for incompressible material in an uniaxial extension to describe the elastic behavior of the chambers walls, equations (3.1) and (3.2), respectively, can be rewritten as follows:

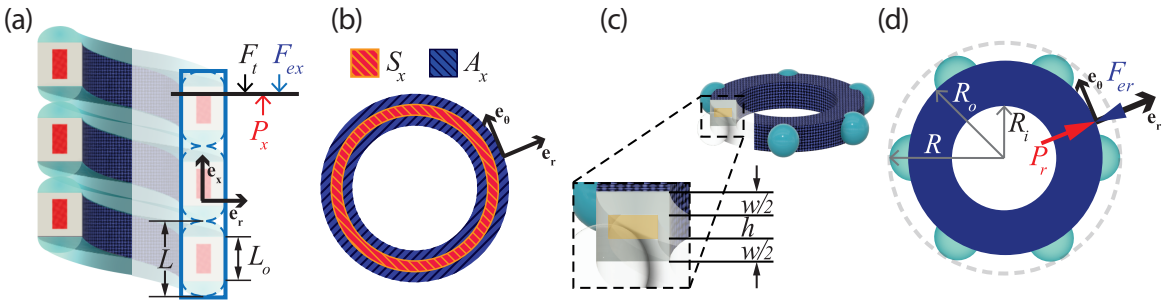

Fig. 3.3: Model of the simplified (a) front cross-sectional view and (b) top-view axial extension showing the interacting forces and areas respectively. (c) Perspective cross-sectional area and (d) top-view radial expansion showing the lengths and interacting forces respectively.

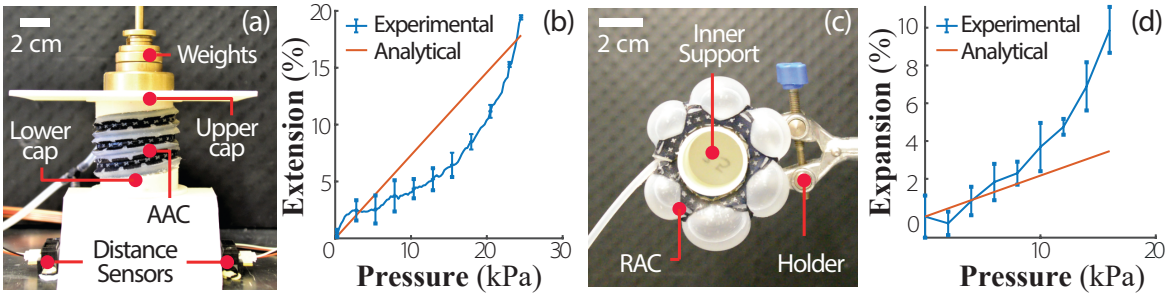

Fig. 3.4: Experimental validation of the analytical model for SoPHIA's actuation chambers. (a) Side view of a three AAC pressurized SoPHIA coils used to validate the mathematical model of axial extension. (b) Experimental and analytical evaluation of the AAC performance. (c) Top view of one of the RAC pressurized SoPHIA coils used to validate the analytical model of radial expansion. (d) Experimental and analytical evaluation of the RAC performance. Error bars stand for standard deviation of 3 trials. We pressurized the samples from 0 to 25 kPa for the AAC and from 0 to 22 kPa for the RAC. For the AAC, we used 2 N of load to represent the resistive force of the host tissue [43]. For the RAC, the resistive force was not considered.

$$A_x \frac{2E}{6}\left[\left(\frac{L}{L_0}\right)^2 - \frac{L_0}{L}\right] + F_t = S_x P_x \tag{3.3}$$

$$w\frac{2E}{6}\left[\left(\frac{R-R_i}{R_0-R_i}\right)^2 - \frac{R_0-R_i}{R-R_i}\right] = hP_r \tag{3.4}$$

where A_x is the cross-sectional area of the extended material in the AAC, E is the Young's modulus of the material, L is the height of the AAC after extension, L_0 is the initial height of the AAC, w is the width of the expanded material in the RAC, R, R_i, and R_0 are respectively the external radius of the RAC once expanded, the internal radius of the RAC, and the initial

Table 3.1: Model Parameters

Notation	Description	Value	Unit
S_x	cross-sectional area of the inner channel of the AAC	415	mm^2
A_x	cross-sectional area of the extended material in the AAC	829	mm^2
w	width of the expanded material RAC	6	mm
h	height of the RAC air channel	3	mm
R_0	initial external radius of the RAC	2.49	mm
R_i	internal radius of the RAC	17.5	mm
L_0	initial height of the AAC	9	mm
F_t	resistive force of the host tissue during the mechanotherapy treatment	2	N

external radius of the RAC. Fig. 3.3 illustrates the main parameters considered in the model. The model parameters are given in Table. 3.1.

In order to estimate the Young's Modulus, we used least squares curve fitting using the axial extension results with the model obtained in equation (3.3). The Young's modulus was optimised in the range of values found in the literature, from $E = 0.027\,\text{MPa}$ [23] to $E = 0.069\,\text{MPa}$ [195]. After the fitting, the best Young's modulus was determined to be $E = 0.068\,\text{MPa}$. The values in Table. 3.1 are based on the geometry of the actuator. The value for the resistance force Ft was taken from [43].

3.5.1 Experimental Validation of the Model

Two experiments were performed to validate the analytical model derived in the previous section. To validate the analytical model for the AAC, we coiled three turns of that chamber around an oiled (Cole Parmer VacuumPump Oil CP 500) PLA tube to reduce friction and support it vertically without restricting its movement (Fig. 3.4 (a)). An ABS plate at the top of the AAC acted as a reference for the two reflective distance sensors (SHARP© GP2Y0A41SK0F) to measure the extension, as well as to support the weights that simulate the resistive force F_t. We used two distance sensors, averaging the readings, in order to avoid inaccuracies due to uneven extension of the actuator on either side. We pressurized the AAC from 0 to 25 kPa and recorded the extension readings to obtain L. We performed three trials. For the experiments, we define extension as $\frac{L-L_o}{L}$.

To validate the RAC, we glued one turn of the RAC, along its entirely constrained face, around an ABS tube using cyanoacrylate adhesive (Fig. 3.4 (c)). The ABS tube was supported by a clamp stand. Then, we pressurized the RAC from 0 to 20 kPa and measured

its radial expansion, defined as $\frac{R-R_o}{R}$ over three trials using Image J (NIH; v.1.31, available as freeware from http://rsbweb.nih.gov/ij/)). For both chambers, relative pressure was considered. The maximum pressure values were defined considering pressurization before anisotropic deformation and failure.

As can be seen in Fig. 3.4 (b) and Fig. 3.4 (d), there is a reasonable agreement between the theoretical models and the experimental values. We calculated the root-mean-square error (RMSE) between the three AAC extension trials and the analytical model, resulting in an average RMSE of 2.95%. Similarly, we calculated the RMSE for the three RAC expansion trials and the analytical model, resulting in an average RMSE of 2.8%. The average error is similar for the two chambers but their ranges of expansion are different. Since the AAC has a longer stroke, the normalized standard error is smaller than for the RAC.

The observed differences, in both the AAC and the RAC, can be explained by the model limitations. First, the proposed model only takes into account the wall extension in one direction during the pressurization, but does not consider the ballooning behavior of the chambers. We further elaborated this aspect of the model in [80]. Secondly, the Neo-Hookean model was chosen for its simplicity, in order to provide information about the impact of each design parameters, e.g., size, Young's modulus, on the actuator's extension and expansion for a potential adaptation of SoPHIA to other applications. Finally, the model is not considering the impact of interdependence between the two chambers to axial extension. However, this effect is characterized and quantified in Section 3.7.1.

3.6 SoPHIA Characterization

We conducted experiments to characterize SoPHIA's extension, expansion and force capabilities, to determine its standalone capabilities, as well as those under conditions that are expected clinically such as the use of implant-to-tissue adaptors and staged extension. This section describes the corresponding experimental setups and methods.

3.6.1 Control Setup

The system is comprised of two pneumatically actuated chambers: axial and radial. Modular circuit boards were designed for ease of use and reliability. The primary printed circuit boards (PCBs) house the microcontroller, power input, and communication, while dedicated auxiliary boards include the pneumatic components, one for each of the chambers. The primary board provides connections for three separately actuated pneumatic channels, taking into account a possible extension of the design in the future. Fig. 3.5(a) illustrates the general electrical

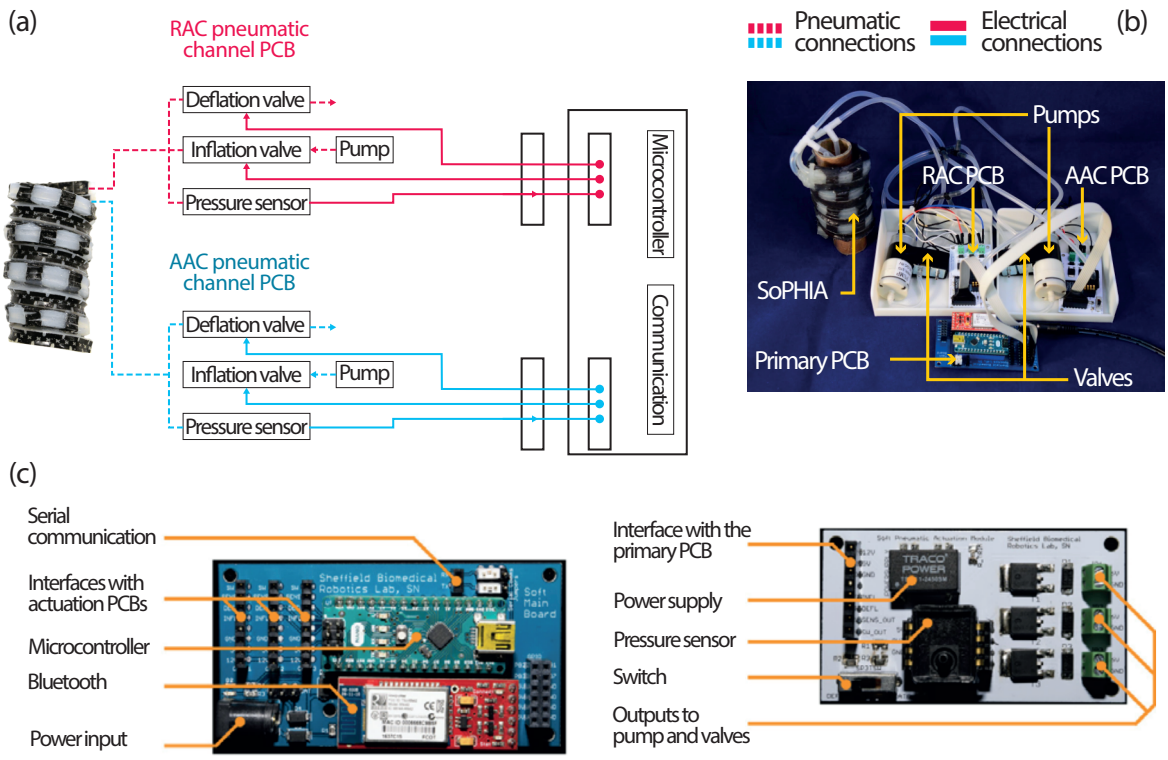

Fig. 3.5: Electrical design. (a) Electrical design topology, (b) electrical setup with the helical actuator connected. (c) Overview of the main and auxiliary control PCBs.

topology, including our electrical control and feedback as well as pneumatic connections. Fig. 3.5(c) provides an overview of the designed PCBs. Each of RAC and AAC have a dedicated DC pump (XRR-370) and two normally closed solenoid valves (FA0520D) for inflation and deflation. Inflation is achieved by the pumps and deflation is achieved by opening the corresponding valve and exhausting the air from the actuator. The air pressure within the chambers was tracked by Honeywell ASDXAVX005PGAA5 pressure sensors. The position sensor used is an infrared distance sensor (SHARP© GP2Y0A41SK0F) which was fed back and compared with the target position. When two distance sensors where used (Fig. 3.6 (a)) the average of the position measurement was taken. The valves are controlled by independent digital signals from the microcontroller (Arduino Nano ©). Because the valves and pumps require currents as high as 300mA, they are interfaced with the microcontroller through MJD112G NPN transistors. The inflation and deflation of each chamber is triggered by a position proportional integral control, further described in Section 3.8.2.3. The circuit can be powered by either a 12V/3A power supply (XP POWER VEP36US12) or a rechargeable battery pack (for example 8 x eneloop AAA batteries, providing 9.6V to the system). The design was based on the low-cost electropneumatic circuit developed by the Soft Robotics Toolkit [184]. Fig. 3.5(b) shows the entire setup, where the helical actuator is interfaced

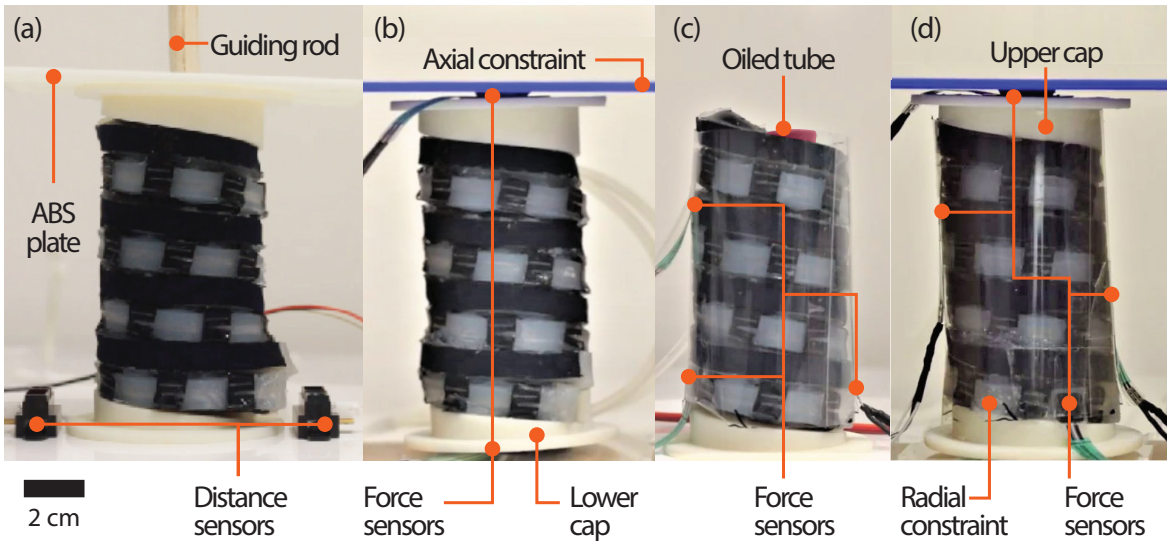

Fig. 3.6: Experimental setups to characterize extension, expansion and force capabilities. (a) SoPHIA placed around an oiled tube and a rod that guides the axial freeload extension of an ABS plate to record the actuator's extension. (b) Two force sensors were placed at the top and bottom of an axially restricted SoPHIA to measure axial forces. (c) Three force sensors were placed on the expandable sections of the RAC to record forces exerted against a PET sheet that envelops SoPHIA. (d) SoPHIA restricted axially and radially to record overall forces.

through two pneumatic channels. Using this circuit, the two actuator chambers could be pressurized independently or simultaneously.

3.6.2 Axial Extension

Considering that SoPHIA's primary application is to elongate tissue via mechanostimulation, it is relevant to characterize its axial extension in dynamic conditions in order to evaluate its suitability to elongate tissue. In this set of experiments, we investigated the hysteresis of SoPHIA by measuring the free-load axial extension response of the AAC, the RAC and the simultaneous pressurization (AAC+RAC) to pressures of 25 kPa, 20 kPa and a combined 45 kPa respectively. These were pressurization cycles of 2 seconds.

We placed SoPHIA around an oiled (Cole Parmer Vacuum Pump Oil CP 500) plastic tube to reduce friction and support it vertically without restricting its movement. A rod guided the axial extension of an ABS plate that worked as a reference to the distance sensors to measure SoPHIA's extension (Fig. 3.6 (a)). This rod was necessary for the benchtop tests, yet not needed for the clinical setting when SoPHIA will be fixed to the tubular tissue. We performed three trials of five cycles each. Then, we pressurized the AAC+RAC up to their breakage point to find their maximum expansion before failure, leaving time to settle. For this experiment, we only needed the oiled tube to support the actuator under free-load

conditions (Fig. 3.6 (a)). Extension was recorded and then measured using Image J (NIH; v.1.31, available as freeware from http://rsbweb.nih.gov/ij/)).

3.6.3 Axial and Radial Output Forces

Given that SoPHIA may be used as an implantable device, it is necessary to understand the potential forces that it can exert against the target tissue. According to [43], forces to stretch the tissue axially should be around 2.3 N. In order to investigate if this force requirement is fulfilled, and considering the interdependence of the AAC and the RAC found in our previous work [156], we proceeded to characterize the force interactions between the two chambers under constrained and unconstrained setups, performing five trials for each set of conditions. After five trials the results showed a reasonable characterization, therefore, there was no need for further trials to deepen our analysis.

To measure the axial forces exerted by SoPHIA's extension, we placed two force sensors on the top and bottom of the actuator respectively, and we restricted its expansion in these same two locations as shown in Fig. 3.6 (b). Both force sensors were averaged to get an overall reading of the maximum axially exerted force. Then, we pressurized the AAC and the RAC independently and simultaneously. The constraints were placed in direct contact with SoPHIA. To measure the radial forces exerted by SoPHIA's expansion, the actuator was enveloped in a rigid polyethylene terephthalate (PET) cylinder with force sensors adhered to its inner surface and in direct contact with the unconstrained segments in the RAC, as shown in Fig. 3.6 (c). Then, we pressurized the AAC and the RAC independently and then simultaneously. To measure the overall forces that SoPHIA can exert, the actuator was constrained both axially and radially at the same time (Fig. 3.6 (d)). Then we pressurized the AAC and the RAC independently and then simultaneously.

3.6.4 Structural Strength

Since SoPHIA needs to sustain forces around nine days in tissue regeneration treatment [43], structural strength is an important feature to test, to determine how much weight the implant can support, at different pressurization levels, without buckling. To test the structural strength, both the axial and radial chambers were pressurized at 3 different levels of averaged pressure, 10.5 kPa, 13.5 kPa and 16.5 kPa, as well as non-pressurized. With no constraints around SoPHIA, weights were then progressively added, until we observed the actuator buckling. The weights were guided on to the top cap of SoPHIA by an acrylic tube. We repeated the experiment five times.

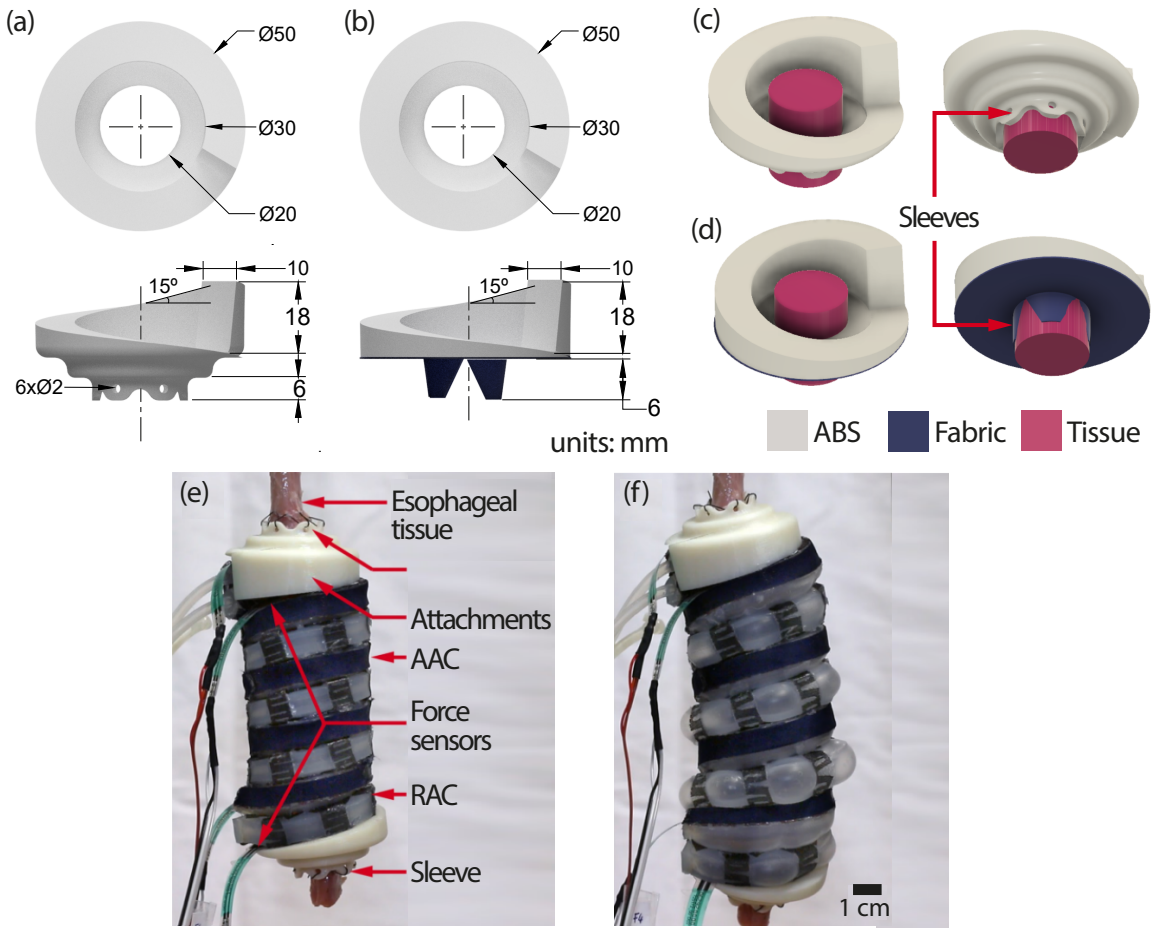

Fig. 3.7: Experimental setup, attachment and mechatronic components. (a) Hard and (b) semi-soft attachments' general dimensions. (c) Hard and (d) semi-soft diagrams showing how they are mounted on the tissue. (e) SoPHIA in relaxed and (f) pressurized states at 15 kPa for the Radial Actuation Chamber (RAC) and 20 kPa for the Axial Actuation Chamber (AAC), using the hard attachment.

3.6.5 Evaluation of Hard and Semi-Soft Implant-To-Tissue Attachments

Because SoPHIA is designed to exert traction forces on tubular organs while decreasing the risk of fibrotic response, the functional interplay between the tissue and the mechanical function of the implant is relevant. Due to this, we investigated two methods to attach SoPHIA to a cadaveric esophageal tissue and tested their effect on its performance: (1) a fully hard attachment with an integrated hard suturing sleeve (Fig. 3.7 (a,c)) and (2) a hard attachment with a polyester fabric sleeve (semi-soft attachment) that were sutured to the tissue (Fig. 3.7 (b,d)). For the semi-soft attachment, the fabric sleeve was chemically bonded to the hard part using cyanoacrylate adhesive. Both of the designs were fixed to the a cadaveric swine esophageal tissue by subcuticular continuous sutures using surgical thread (Mersil Ethicon-W577) (Fig. 3.7(e)). Four force sensors (I.E.E. Strain Gauge, RS

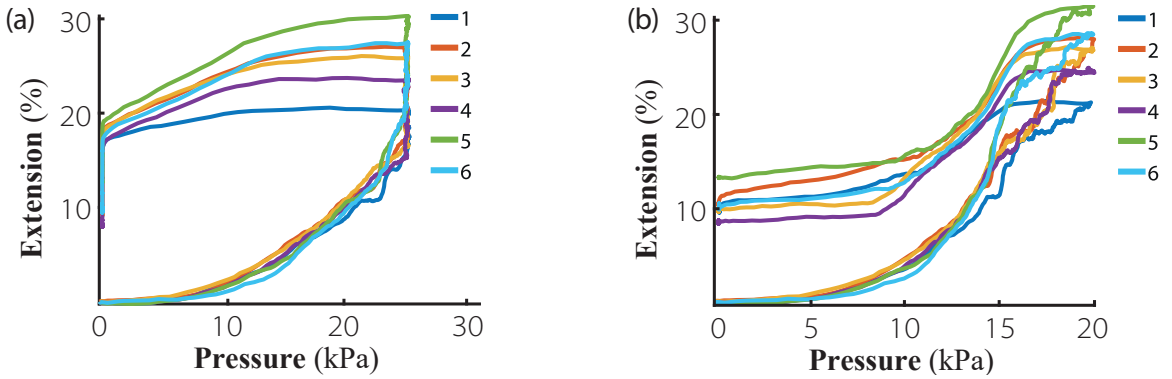

Fig. 3.8: SoPHIA's dynamic extension behavior. (a) Extension behavior as a function of axial pressure and (b) as a function of radial pressure when the AAC and the RAC are simultaneously actuated. SoPHIA exhibits hysteresis behavior and yields up to 30% of freeload axial extension under pressurization cycles of 2 seconds. Experimental conditions are detailed in Section 3.6.2.

Components) were placed between SoPHIA and the ABS attachments (Fig. 3.7(e)) to record the amount of force that can be exerted with regards to the resistance of the *ex vivo* tissue while SoPHIA is pressurized. We supplied 25 and 20 kPa of pressure to the axial (AAC) and radial actuation chambers (RAC) (Fig. 3.7(f)) respectively, in sequence. Simultaneous pressurization of the AAC and RAC caused the actuator to expand up to 25% its original size. We performed 3 trials per attachment design.

3.7 Results

3.7.1 Axial Extension

Under dynamic conditions, with two-second cycles, SoPHIA can axially elongate 0.25 cm (2.3%) at 25 kPa when only the AAC is pressurized, 0.7 cm (6.5%) at 20 kPa when only the RAC is pressurized and 2.8 cm (26%) when both are pressurized simultaneously (Fig. 3.8). The extension capability is enhanced by simultaneous pressurization of the chambers, exhibiting nonlinear behavior. Additionally, both actuation chambers show hysteretic behavior. The AAC shows an average hysteresis of 19% with a standard deviation of 1.36%. The RAC shows an average hysteresis of 10.71% with a standard deviation of 1.53%. Hysteresis in SoPHIA's chambers can be explained by the Mullins effect, a stress softening phenomenon that affects filled rubbers [232], such as Ecoflex 00-30, and occurs over cyclic loading and large deformations as in the conducted experiments.

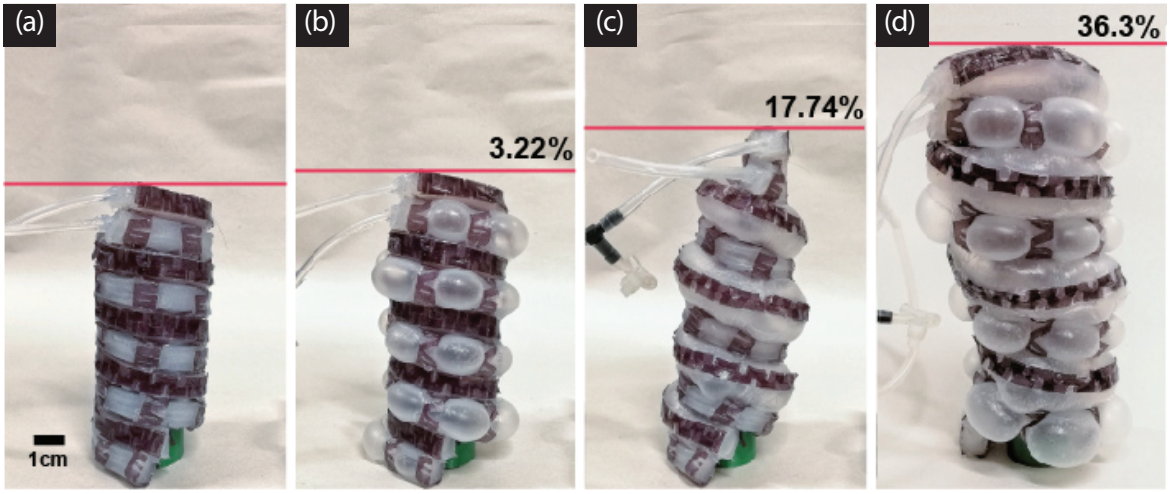

Fig. 3.9: SoPHIA's static behavior under different actuation modes. (a) SoPHIA in a relaxed state, (b) with only the RAC pressurized, (c) only the AAC chamber pressurized and (d) both chambers pressurized. By pressurizing the AAC (25 kPa) and the RAC (20 kPa) simultaneously, SoPHIA is capable of reaching 36.3% of extension in comparison to its original size.

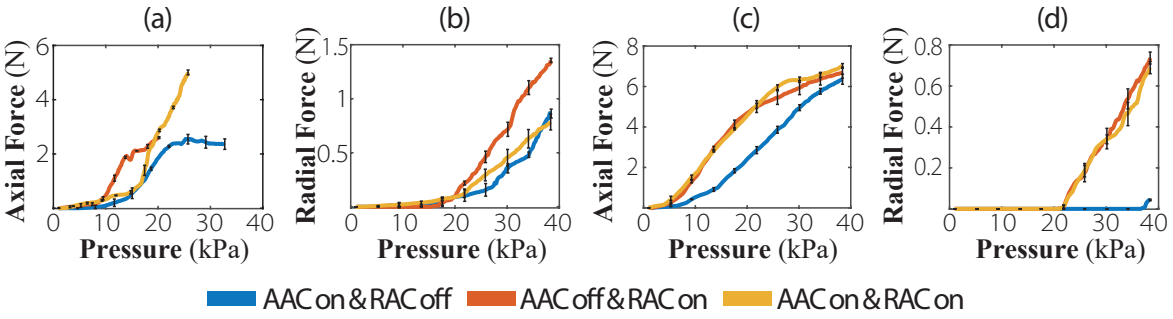

Fig. 3.10: Mean output force capabilities with standard deviation for five trials. (a) Axial forces under axial constraints and three actuation modes. (b) Radial forces under radial constraints and three actuation modes. (c) Axial forces under axial+radial constraints and three actuation modes. (d) Radial forces under axial+radial constraints and three actuation modes. As expressed in the results section, axial forces represent the most benefited from interdependence between chambers with the lowest standard deviation among trials and conditions. Experimental conditions are specified in Section 3.6.3.

In comparison, under static conditions (when the actuator had time to settle) SoPHIA can axially elongate 3.2%, 17.7% and 36.3% of its original size when the RAC, the AAC and RAC+AAC are actuated respectively (Fig. 3.9).

3.7.2 Axial and Radial Output Forces

SoPHIA is capable of exerting up to 7 N axially, when the AAC and the RAC are pressurized simultaneously at 38 kPa while entirely constrained (Fig. 3.10 (c)), and it only exerts 0.69 N

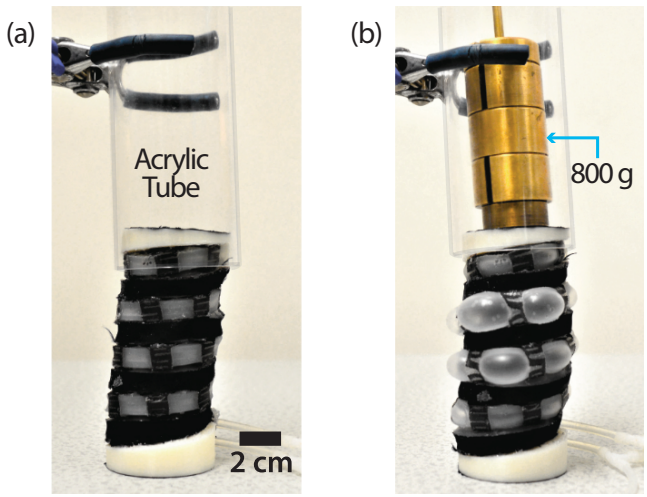

Fig. 3.11: SoPHIA's structural strength. (a) SoPHIA unloaded and in a relaxed state, and (b) at an averaged pressure of 16.5 kPa withstanding a maximum weight of 800 g.

radially under the same conditions (Fig. 3.10 (d)). This behavior is constant along all the setups, meaning that SoPHIA tends to direct its forces 90% more axially than radially. This is confirmed by looking at Fig. 3.10 (a) and (b). This result is positive considering the intended clinical application as it means that SoPHIA is capable of exerting higher forces than the ones needed in proved functional mechanotherapy [43] at low levels of pressure. SoPHIA can exert up to 1.35 N of force at 38 kPa when it is radially constrained which is equivalent to the force we would be able to yield against a tubular organ (Fig. 3.10 (b)).

3.7.3 Structural Strength

SoPHIA's helical configuration provides increasing structural strength, with increasing levels of average pressure. In a relaxed state, SoPHIA can stand 4.9 N of weight without buckling (Fig. 3.11 (a)). This strength increases as the actuator increases its inner pressure. Pressurized at an average of 16.5 kPa, it can withstand up to 7.8 N (Fig. 3.11 (b)).

3.7.4 Evaluation of Hard and Semi-Soft Implant to Tissue Attachments

The hard attachment exerted a maximum force of 0.15N on the tissue, with forces first noticeable at an axial pressure of 10 kPa and a radial pressure of around 7 kPa (Fig. 3.12(c)). The semi-soft attachment exerted similar maximum forces of 0.15N in all trials by applying a combined (axial and radial) pressure of 45 kPa. The forces were linearly related to both axial and radial pressure, with forces recorded from 0 kPa for both pressures (Fig. 3.12(c)).

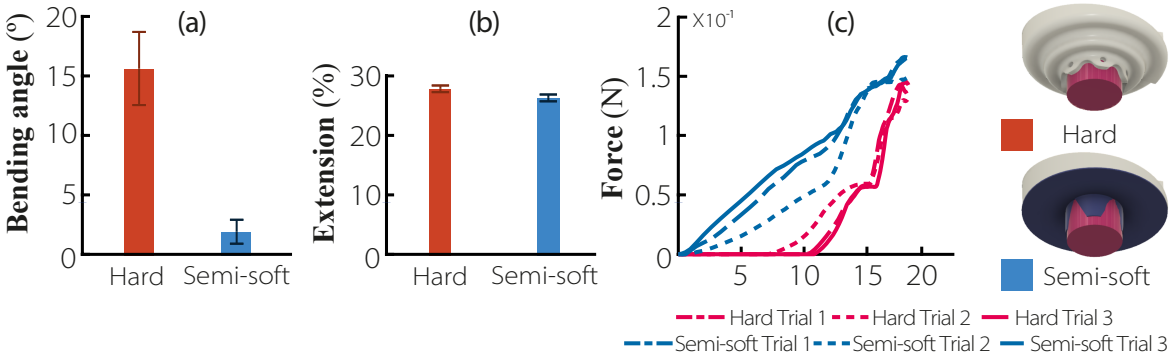

Fig. 3.12: Experimental results. (a) Bending angles and (b) extension per attachment type. (c) Force behaviour vs applied pressure for the hard and semi-soft attachments.

The similar maximum forces for both sleeve designs confirm that the material selection has no impact on the traction force capacity that SoPHIA can exert on the tissue.

We measured the extension and bending angle of SoPHIA, as an indication of its capability to stretch the tissue on which it is fixed. With the two designs, SoPHIA achieved a similar level of extension around 27% (± 1) at the maximum pressurization (Fig. 3.12(b)). In contrast, the bending angles varied between the two designs (Fig. 3.12(a)). While SoPHIA's extension with the hard and semi-soft attachments were consistent, the bending angles differed.

3.8 SoPHIA Staged Control

After characterizing SoPHIA, the control requirements for the real-life application were considered. Envisaging the *in vivo* tissue growth treatment, SoPHIA will be fixed at its ends inside the tubular organ and will extend axially every 24 hours in order to apply tension to the tissue [43]. During the week-long traction procedure, the physiological response of the tissue stiffening is to resist to the applied traction forces [68]. A release of this tension can be observed on the tissue between the traction applications, as a consequence of tissue relaxation and growth. In this section, we describe the setup, experimental procedure, results and SoPHIA's control used to simulate staged tissue growth mechanotherapy.

3.8.1 Tissue Growth Simulation

3.8.1.1 Physical Simulator

A benchtop tissue growth simulator, shown in Fig. 3.13, was developed in order to derive the control of SoPHIA in an environment similar to the one *in vivo*. The benchtop simulator has two roles: to simulate the tissue stiffness and growth, and to monitor SoPHIA's performance.

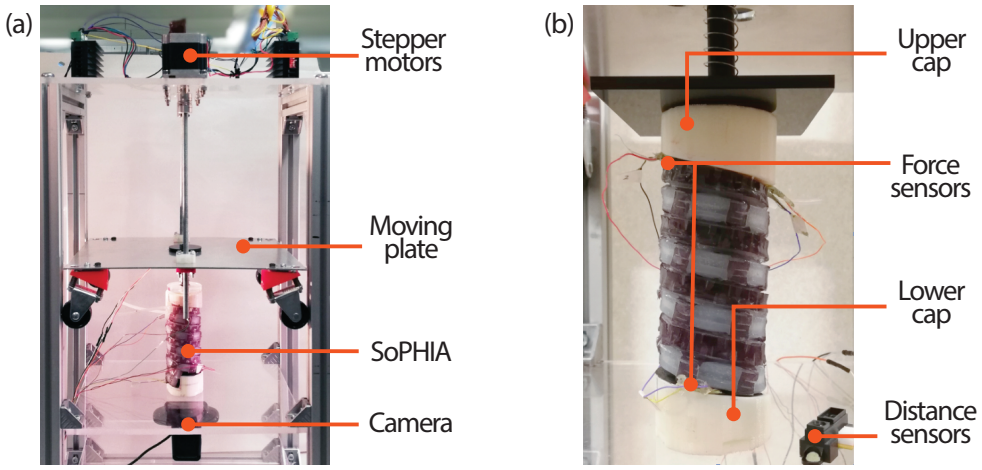

Fig. 3.13: Physical simulator of tissue stiffness and growth. (a) Overall side view; (b) detail of the sensors and actuator in the physical simulator.

The tissue growth and stiffness are simulated via two mechanisms: a passive spring actuated plate, and a controlled lifting plate. Monitoring is then achieved using pressure, force and distance recordings from the platform.

Tissue growth and stiffness were simulated using a combination of passive and active mechanisms. The tissue stiffness is replicated using a compression spring (LP 026LM 06S316, Lee Springs) - which has a 0.05 N/mm spring rate, 50.8 mm free length, 7.035 mm solid length. As SoPHIA lengthens it experiences a resistant force corresponding to the level of spring compression. The spring itself was mounted around a plastic rod capped by two acrylic plates to prevent buckling.

The tissue growth simulation was achieved using the active mechanism, made of two NEMA-23 stepper motors (57STH56, Phidgets), controlled by two stepper motor drivers (TB6600, TopDirect) through an Arduino Uno R3 microcontroller. The two motors are coupled to two vertical M8 threaded bars which lift the moving plate. The moving plate itself carries the passive spring mechanism and, when displaced vertically, allows the spring to decompress, thus simulating tissue growth. The tissue growth simulation is monitored via two distance sensors which measure the displacement of the moving plate.

Throughout the simulation, SoPHIA is also monitored by three different sensor readings: pressure, force and distance. The pressure recordings are taken from the dedicated AAC and RAC PCBs (Section 3.6.1). Similarly to the previous experiments, the force recordings are taken from four force sensors, two placed on the top and two placed on the bottom. SoPHIA's extension is measured by taking the average of two distance sensors which track the displacement between the spring actuated plate and the ground plate.

3.8.1.2 Experimental Procedure

We simulated the growth of 3.2 cm of virtual tissue by expanding SoPHIA axially, pressurizing simultaneously the AAC and the RAC. The expansion of both chambers was semi-constrained by the spring actuated plate, in order to simulate the resistance that SoPHIA will experience from the tissue under stretch. SoPHIA was constrained by a PET sheet, simulating its enclosure in a tubular tissue shown in Fig. 3.14 (a). Both chambers were pressurized simultaneously, controlled by the target distance determined for each stage, shown in Fig. 3.14 (a-e). The overall target distance of 3.2 cm was chosen as the maximal semi-constrained inflation extension before risk of failure.

The procedure followed for the simulation of tissue growth consists of four stages described in Fig. 3.14. Firstly the actuator is pressurized and then the moving plate is lifted to decompress the spring mechanism. Using this procedure, two sets of experiments were performed. The first set consisted of using manually tuned values for each stage that were then further improved in the second set using modeling and automatic tuning. Each set of experiments consisted of five trials.

The results show that SoPHIA exerts up to 0.19 N of average force against the moving plate that represents one of the stubs of the organ in the clinical application. When the moving plate is lifted at the end of each stage (Fig. 3.14 (f)) simulating relaxation of the target tissue to the displacement of SoPHIA, the forces drop to around zero N (Fig. 3.15). The high non-linearity of the force/displacement responses is caused by the fact that SoPHIA is constantly in contact with the moving plate and increases the contact forces as soon as it starts extending as it would perform in a realistic clinical setting. At the beginning of the trials, the initial interaction force between SoPHIA and the tissue simulator was set to around 0 N, although it could be tuned to other values depending on the initial position of the moving plate relative to SoPHIA.

3.8.2 Modeling and Control for Axial Extension

In this section, the control details of SoPHIA's axial extension in the tissue growth simulator are explained. The requirements of the controller are first established and more details about the controller used are given. The modeling approach is then presented, detailing how the transfer function models are derived. Finally, the control tuning is described and compared against the initial requirements.

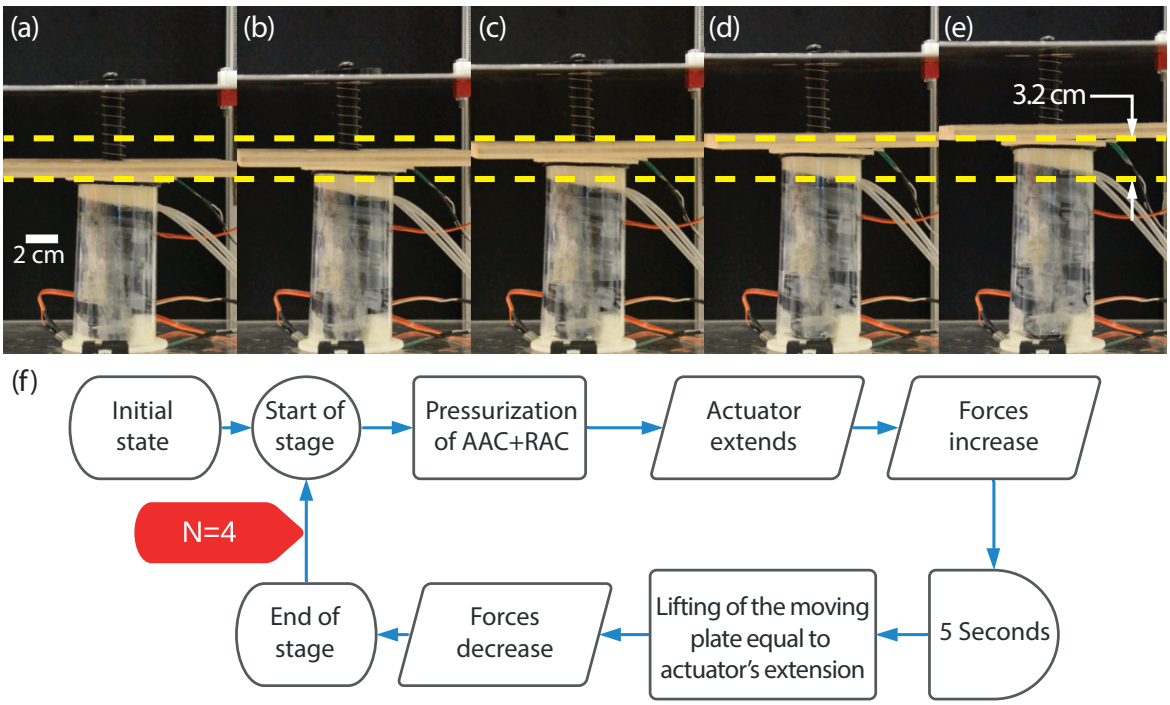

Fig. 3.14: Experimental procedure for the simulation of tissue growth treatment based on the staged application of traction forces. The dashed yellow lines represent the initial and final states of the moving plate. (a) SoPHIA in a relaxed state; (b) end of stage 1 reaching 0.8 cm, (c) end of stage 2 reaching 1.6 cm, (d) end of stage 3 reaching 2.4 cm, and (e) end of stage 4 reaching 3.2 cm. (f) Flowchart describing each stage in the simulation.

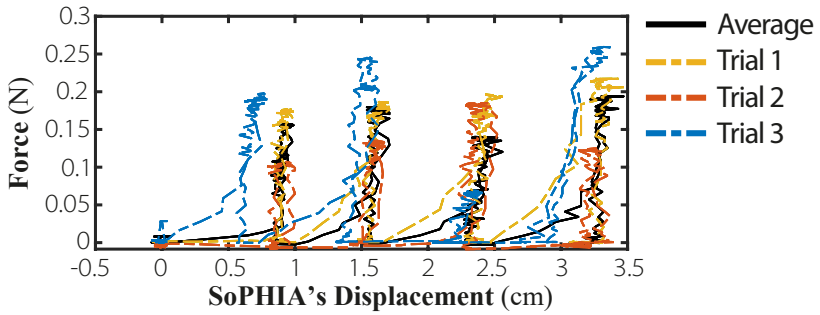

Fig. 3.15: Force response of SoPHIA caused by its extension. The decrease in force represents the end of each of the stages during the simulation.

3.8.2.1 Specifications

To establish the requirements for the controller design, both the clinical requirements and the current limitations of the actuator were taken into account. A steady-state error requirement of less than 1 mm was set. The steady-state error was limited to 1 mm, to be as small as possible, while taking into account the precision of the distance sensors that is around ± 1 mm.

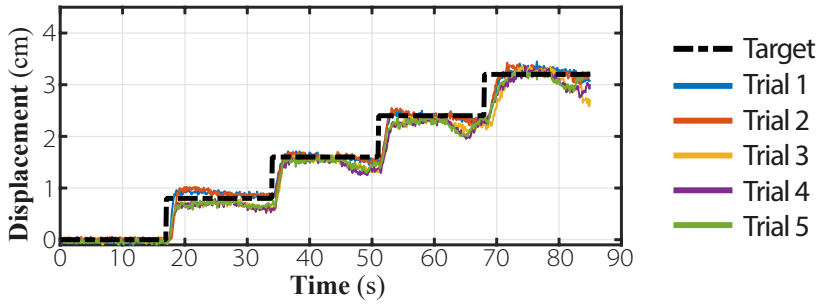

Fig. 3.16: Plot of all of the trials with the improved control throughout all 4 stages.

In addition, the rise time was set to be maximized to ensure a slow elongation of the tissue and to avoid tearing.

For the system itself, a position PI controller was used, as it was deemed appropriate to meet the requirements. A target extension of 0.8 cm for each stage was chosen, to have 4 stages of visually noticeable displacements. Additionally, an overall safe pressure limit of 39 kPa was enforced, and stopped pressurization if reached, to ensure SoPHIA would not burst. This overall safe pressure limit was determined from the maximum pressure of the previous experiments. Based on these design requirements and inspired by the current daily clinical intervention for tissue elongation [68], a gain-scheduled lengthening process was hypothesized to be suitable. Gain-scheduling was chosen to allow for better tracking of the reference signal and improve the overall behavior of the actuator. The PI values for all of the stages were initially set based on testing of previous actuators, before being improved later based on the modeling.

3.8.2.2 Modeling

For each of the stages, a model was found using system identification to aid with the tuning of the PI controller. Based on the linear dynamics observed in each stage, a low order linear time invariant transfer function was fit to the data. Of the five trials conducted, the best trial, selected based on minimal overshoots and minimal steady-state error for each stage, was chosen for modeling. A model was fit to this selected trial, identifying a second order model for stage 1 and first order models for the remaining stages. The transfer functions were determined using subspace identification with an automatic estimation of the initial condition and using the instrument variable approach for initialization.

3.8.2.3 Control

The PI values for each of the stages were tuned to meet the requirements set out in section 3.8.2.1. The overall aim of the tuning process was to achieve a smaller steady-state error,

Table 3.2: Averaged performance characteristics for the initial and improved trials. Tr: rise time, OS: overshoot and SSE: steady-state error.

	Initial				Final			
	Stg1	Stg2	Stg3	Stg4	Stg1	Stg2	Stg3	Stg4
Tr (s)	x	4.05	3.30	x	1.12	1.20	1.90	2.45
OS (%)	0	0.25	1.50	0.44	11.25	4.63	2.83	5.94
SSE (cm)	0.11	0.05	0.04	0.09	0.07	0.02	0.05	0.07

while keeping rise time as slow as possible. The digital tuning of the PI values was done using the Ziegler-Nichols method applied to the developed model transfer functions. For the tuning, a small steady-state error was prioritized, as well as a slow rise time to achieve a steady pressurization. After this initial digital tuning, the PI values were then further fine-tuned, taking into account the noticed behavior changes to smooth the response. Fig. 3.16 shows the comparison between initial and improved control throughout all 4 stages, where we demonstrate an improvement by implementing automatic tuning on the gain-scheduled lengthening process control scheme. The averaged achieved performance from the first five trials and the next five trials with improved control are summarized in Table. 3.2.

Overall, most of the stages showed a decrease in steady-state error or at least comparable values with the improved control, although this did come at the cost of greater overshoots and faster rise times. Additionally, compared to the initial tunings, where rise times were not available for stages 1 and 4 as 90% of the target value was not reached, all of the stages with the improved control reached these target values as a minimum. Overall, the system met the requirement of a steady-state error of less than 1 mm across all stages, promising safe operation for the envisaged clinical procedure.

3.9 Discussion and Conclusion

In this Chapter, we introduced a Soft Pneumatic Helically-Interlayered Actuator (SoPHIA), capable of configurability and multimodal axial extension and radial expansion, that we envisage as an implantable device to provide mechanostimulation for tissue growth. We evaluated SoPHIA's performance using a novel physical simulation platform that we envisage to be used as a research tool for tissue regeneration simulation.

We tested the capability of this actuator by evaluating the extension, output force and characterizing its nonlinear behavior. SoPHIA is capable of growing axially 36.3% its original size under freeload static conditions at an average pressure of 22.5 kPa and 33.3% under

loaded-staged control at an average pressure of 21 kPa. By constraining SoPHIA entirely and then pressurizing both chambers, which is a clinically-realistic condition, SoPHIA can exert up to 7 N axially and up to 1.35 N radially, if only the RAC is pressurized. These capabilities make the actuator suitable to address the reconstruction of tissues in clinical conditions such as LGEA (where more than 3 cm of tissue is missing) or tissue shortage caused by surgical resections. While the output performance of the soft actuator is comparable to many soft pneumatic actuators in the literature [164, 4], the design and behavior of SoPHIA provide unique features that are clinically advantageous:

- By using a geometrically simple building block (actuation chambers) that can be coiled from one to a three-dimensions actuator, we can configure SoPHIA into a cylinder that fits to various diameters of hollow organs and tubular tissues, making it a versatile medical tool. This is concisely discussed further in Appendix A.3.
- Its ease of configuration could facilitate clinical intervention on different organs. This potentially could be done by performing a small incision near the target organ, through which the AAC and RAC could be inserted, implanted and removed employing minimally invasive surgery procedures such as laparoscopy. This is concisely discussed further in a preliminary test on an animal carcass in Appendix A.4.
- By varying the orientation of the chambers, we can address different conditions. For example, the RAC could be oriented to expand inwards in order to stimulate the intestine during SBS treatment. It can also be oriented to expand outwards during LGEA treatment (Fig. 3.2).
- The helical shape also provides structural support, with air pressure distributed uniformly across the diameter and height of the actuator. We showed that the implant can support up to 800 g without buckling. This feature is clinically important as buckling could lead to a misshapen organ.

Over the duration of the treatment, the AAC may be progressively pressurized to support the lengthened tissue. The RAC may be intermittently pressurized to provide radial stimulation to the tubular organ and also to decrease fibrotic response. Powering and monitoring a robotic implant via loose cabling that exits the body through a skin port into a control box was demonstrated clinically viable in [43]. For the pneumatic tubing a similar approach is envisaged, however this needs to be tested pre-clinically.

We also presented the design of two implant-to-tissue attachment methods and tested their effects on the tissue's elongation in function of the mechanical forces exerted by the

implant. These attachments can be used without being in direct contact with the organ to heal, in order to reduce fibrosis. We demonstrated that a semi-soft attachment is capable of elongating axially and exerting similar traction forces as a hard sleeve. Moreover, the semi-soft attachment applied forces more gradually which is better suited to clinical applications, compared to the sharper increase in forces with the hard attachment, which could result in tissue damage. The forces applied by SoPHIA on the tissue, regardless of the attachment type, were low because of the initial fixation on a relaxed tissue. Thus, SoPHIA reached it maximum extension on a relatively not tensed tissue. In our experiments, the esophageal tissue works as axial support for the entire system. While Fig. 3.12 (a) indicates that the design of semi-soft attachment is the most effective for SoPHIA due to the low bending angle value, the extent of bending should not affect the tissue, but rather the extension performance of SoPHIA. We hypothesize that higher bending angles are caused in general, by the manual, and thus less precise, fixation of attachments to the esophageal tissue. However, in the *in vivo* scenario, we conceive that the bending of the actuator will be naturally suppressed by the tight arrangement of the organs. We envisage the use of SoPHIA with semi-soft attachments to perform tissue elongation on tubular organs via mechanotherapy. In this regard, future work includes the development and testing of fully soft attachments. Preliminary work on the design and testing of fully soft attachments is shown in Appendix A.5.

SoPHIA's helical configuration provides multi-modal behavior achieved by interlayering elastomeric chambers of different functions into the helix. Typically, soft helical actuators show some degree of torsion when they incorporate a backbone into their design [22]. SoPHIA is a zero-torsion helical actuator due to being constrained axially and radially.

From the dynamic extension tests, we observed that the RAC generates much more extension than the AAC, whilst under static conditions the opposite is true. We hypothesize that this difference comes from the AAC having a much slower response time, partly caused by the stacking of coils. As the RAC showed superior dynamic expansion than the AAC, which is desirable for mechanotherapy, one option is to use the RAC design for axial extension as well. Another alternative to increase SoPHIA's axial extension is to decrease shear stress between the chambers caused by their different expansion rates that currently causes the actuator to burst. This will be further discussed in Chapter 5. Another observation during the dynamic extension tests was that both chambers exhibit hysteric performance that can be explained by the Mullins effect. We assume this behavior will not impact on mechanotherapy, since in a clinically-realistic condition SoPHIA will be entirely constrained by the tubular organ walls and attachments counteracting the heterogeneous amounts of expansion at different extension stages, as well as closed-loop control.

We evaluated the behavior of SoPHIA using a novel physical simulator. During a week-long clinical tissue lengthening treatment, the tissue may become stiffer (due to inflammation), relax (due to its viscoelastic properties) or grow. These mechanical and physiological changes are being emulated by the physical simulator. Such simulations are difficult to achieve with current phantom tissues or with *ex vivo* biological tissues, as they exhibit limited lengthening. This makes the physical tissue growth simulator ideal to dynamically represent different states of tissues, from mechanical to metabolic, under either physiological or pathological conditions. Further work still needs to be done to simulate the radial growth, as well as the real-time stiffness variation of the tissue.

While the soft-matter actuator is desirable for its stretchability to support a growing tissue, its intrinsic nonlinear behavior needs to be precisely controlled for clinical safety. We thus developed a staged-position gain-scheduled controller, which emulates the daily tissue stretch within the existing clinical treatment. We successfully evaluated the implant control in a physiologically-relevant scenario. Variability of the system represents an important challenge when controlling it due to the sensor disturbances and elastomer non-linearity and wear. However, the presented analytical model constitutes a reliable tool for the prediction of the AAC and the RAC behavior, as there is a reasonable agreement between the theoretical models and the experimental values (Fig. 3.4 (b,d)). Although the proposed model does not consider the ballooning behavior of the chambers, it provides qualitative information of the design parameters that impact SoPHIA's extension. In the future, other nonlinear models, such as Ogden, will be investigated in order to provide more detailed performance insights.

Due to the lack of kinematic equations that describe soft robots in general [50], our approach was a combination of using traditional control techniques and designing constraints to achieve the desired actuation. However, further research is still needed in order to model the behavior of soft machines from first principles. Consequently, we may be able to tune the controller better to decrease the steady-state error, while keeping large rise times. Force control could also be used, such that SoPHIA applies constant traction forces and adapts to the tissue response. Future directions include embedding soft sensors to record SoPHIA's extension and forces, in order to carry out more accurate mechanotherapy control *in vivo*. Further work also includes the advancement of the axial extension capability of SoPHIA for a larger capacity of tissue lengthening.

Chapter 4

Deflected vs Pre-shaped Soft Pneumatic Actuators: A Design and Performance Analysis Towards Reliable Soft Robots

4.1 Preface

In Chapter 3 we introduced the development of a Soft Pneumatic Helically-Interlayered Actuator (SoPHIA) capable of extending up to 36.3% its size, expanding radially, providing forces over 7 N and strong enough to sustain a load of up to 7.8 N without buckling. In order to optimize the performance of such actuator to provide it with a larger capacity of tissue lengthening, in this Chapter, we analyze systematically the design of the Soft Pneumatic Actuators (SPAs) used as SoPHIA's building blocks to evaluate their reliability and response to variable loads. Additionally, we compare the SoPHIA's SPAs performance to Circular SPAs, a widely used SPA design in the soft robotics community. As a result of this analysis conformed by numerical, statistical and experimental procedures we provide a set of design principles that contribute to the design of more reliable SPAs that become part of the next version of the SoPHIA, discussed later in Chapter 5. This Chapter 4 addresses objective D described in Section 1.3. The content of this chapter and its appendix has been published in the following research article:

- E. Perez-Guagnelli, and D.D. Damian. "Deflected vs Pre-shaped Soft Pneumatic Actuators: A Design and Performance Analysis Towards Reliable Soft Robots". *Soft Robotics*. 2021, (In Press).

Where E. Perez-Guagnelli designed, fabricated, characterized and numerically modelled the SPAs and D.D. Damian supervised the research.

4.2 Introduction

Soft robots are machines made of lightweight and highly compliant materials that can be customized to perform a wide range of functions such as locomotion [162] or gripping [136]. Given their compliance, hyperelasticity and inherent safety, soft robots are well-suited to be used in applications such as exoskeletons [7] and implants [155]. Soft actuators are the building blocks of soft robots that enable their motion. Currently, most of them are actuated fluidically and fabricated out of elastomeric matrices with embedded rigid or semi-rigid materials [97]. Design of soft pneumatic actuators (SPAs) has been based on four approaches: (1) variation of cross-sectional geometry [196], (2) morphology of the pneumatic chamber [143], (3) fiber-reinforcements variation [161] or (4) hybrid rigid-soft interactions [229]. Given their influence in motion and considering that some SPAs are designed to perform precise tasks such as minimally invasive surgery [46], it is essential to comprehend how the design of soft actuators impacts soft robots reliability.

Similar to other mechanical meta-materials [20], interaction with the environment or handling during their assembly or fabrication could introduce defects into the SPAs that impact their performance. These defects could lead to high stress concentrations in the SPAs body reducing their fatigue life [130] and efficiency reduction as a consequence of unwanted deformations [225]. Those unwanted deformations cause heterogeneous expansion of the SPAs. It is frequently assumed that SPAs expand homogeneously throughout its unconstrained areas. The oversight of heterogeneous expansion makes it difficult to predict the SPAs performance accurately. Additionally, neglecting repeatability and time-wise consistency of expansion in highly precise tasks could cause serious damage, for example, a burst or leak in a clinical treatment.

Different approaches have been considered to make soft actuators with robust performance. Robertson, *et al* [166] demonstrated that bundled fiber-reinforced SPAs are robust enough to be able to maintain their capacity even when the air supply is cut off to its individual SPAs. Miron and Plante [130] proposed design principles to improve fatigue life of extensible pneumatic muscles, for example, the use of reinforcements to provide low-friction interactions to avoid abrasion between two rubber surfaces that might lead to failure. Martinez, *et al* [125] characterized elastomeric pneu-net structures that can have their functions restored after mechanical damage is applied. Although these approaches provide relevant insights into the design of more reliable SPAs, there is no systematic approach on the impact of chamber design, cross-sectional geometry and fabrication methods as a triad that might be affecting the performance of SPAs. Additionally, although different cross-sectional and chamber geometries have been tested for the design of SPAs, the analysis of their performance under loaded conditions has been done as part of a more complex or constrained

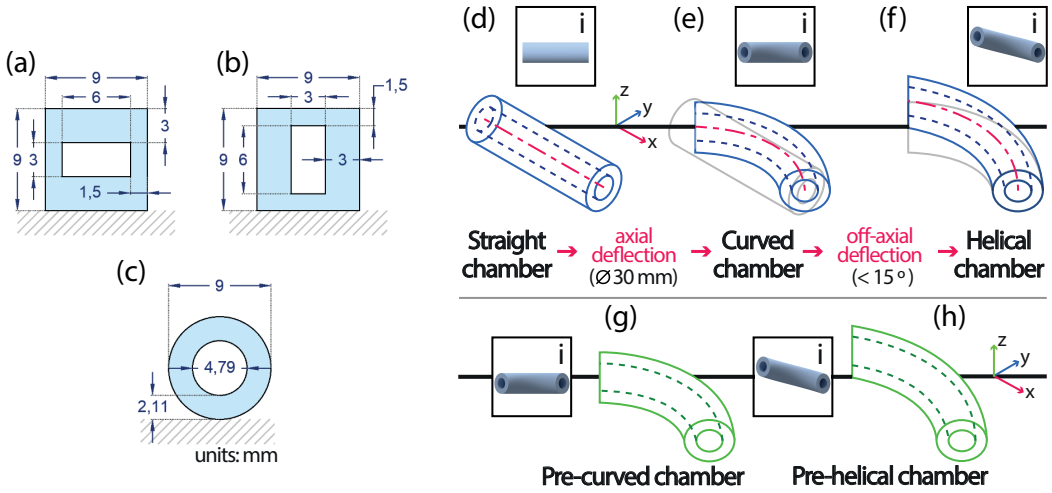

Fig. 4.1: The tested SPA samples of differing cross-sectional geometries and chamber designs. (a) Dimensions of the Horizontal, (b) Vertical and (c) Circular cross-sectional geometries. These geometries were used for each type of chamber: (d) Straight, (e) Curved, (f) Helical, (g) Pre-curved and (h) Pre-helical chambers. Chambers (e) and (f) are shaped by manually deflecting Straight chambers around a cylinder that works as an environmental constraint (Fig. 4.3). Pre-shaped chambers (d,g,h) have been molded under their respective shapes, meaning there is no manual deflection involved in shaping and placing them around the environmental constraint. Inserts i in figures d-h show a frontal view of their respective chambers for clarity.

system, possibly inadvertently hiding underlying effects of the chambers alone. In this work, a combination of modeling, experimental characterization and statistical analysis is used to analyze the design of widely used SPAs, delivering the following contributions: (1) reliability quantification of different SPAs designs by deriving their amount of expansion under variable loading conditions and deflections, (2) a comparative study among different SPA designs based on their performance reliability and (3) a set of principles for the design and fabrication of reliable SPAs. By implementing these design principles derived from our systematic analysis into the planning and design of soft systems, roboticists will be able to make informed decisions into the development of more accurate, robust and efficient robots, increasing their performance predictability and potentially making it easier to model and replicate their motions.

4.3 SPAs Design

We investigated a series of SPAs designs by varying their geometrical properties such as their pneumatic chamber 3D shape, either this shape is obtained by deflecting a chamber or by pre-configuring it from the molding stage, and their cross sectional geometry.

4.3.1 Pneumatic Chamber 3D Shape

We selected three of the most used 3D shapes in the design of SPAs: Straight (Fig. 4.1(d)), Curved (Fig. 4.1(e)) and Helical (Fig. 4.1(f)). The Straight chamber is the most common shape for pneumatic chambers, typically used for single [5] or multi-chamber linear actuators that curve when pressurized [224]. We designate a Curved chamber if it has been initially straight and an axial deflection curved it as a consequence of pressurization or manipulation (Fig. 4.1(e)). Typical examples of the use of Curved chambers are grippers [38]. If the chamber was fabricated curved, meaning that no deflection force has been inputted to the structure to modify its shape, it will be referred to as Pre-curved (Fig. 4.1(g)). We designate a Helical chamber if it has been initially straight and then axial and off-axial deflections coiled it as consequence of pressurization or manipulation (Fig. 4.1(f)). If the chamber was fabricated coiled meaning that no deflection force has been inputted to the structure to modify its shape, it will be referred to as Pre-helical (Fig. 4.1(h)). Some examples include biomimetic grippers [27, 147], walking helically-arranged tubes [200] and soft implantable devices [155]. Due to their versatility, these three shapes of chamber design, deflected or pre-shaped can be found in one system, for instance, in modules with different motion capabilities [37, 225].

4.3.2 Cross-Sectional Geometry

It has been demonstrated that varying certain design parameters in the cross-sectional geometry of a soft actuator has an impact on its performance. For example, by varying its wall thickness, the actuator will expand in the regions with lowest stiffness [87]. Additionally, the force generated by the pressure acting on the soft walls that resist expansion is highly dependant on the cross-sectional area [161]. The height-width ratio of the chamber and air channel will also affect the resistance of the actuator to physical instabilities. For this reason, we decided to explore the implications of orientation of two identical SPAs with anisotropic wall thickness (Fig. 4.1(a,b)). Considering these design parameters and given that Squared and Circular geometries are the most found in the literature, we selected the cross-sectional geometries Horizontal (Fig. 4.1(a)), Vertical (Fig. 4.1(b)) and Circular (Fig. 4.1(c)) to be investigated in this study. For the design of the SPAs with a circular cross-sectional geometry we prioritized to keep consistent (with the Squared SPAs) the cross-sectional area of the air channel (18 mm^2) and their maximum height (9 mm). In summary, combining the selected chamber types described in Section 4.3.1 and the cross-sectional geometries shown in Fig. 4.1(a-c), we analyzed the performance of 15 different SPAs (Table 4.1). The cross-sectional area and length of the air channel was kept consistent among designs.

Table 4.1: SPAs variations combining different cross-sectional geometries and chamber 3D shapes

Chamber Shape	**Cross-Sectional Geometry**		
Deflected	Horizontal	Vertical	Circular
Curved	Horizontal Curved	Vertical Curved	Circular Curved
Helical	Horizontal Helical	Vertical Helical	Circular Helical
Pre-shaped	Horizontal	Vertical	Circular
Straight	Horizontal Straight	Vertical Straight	Circular Straight
Pre-curved	Horizontal Pre-curved	Vertical Pre-curved	Circular Pre-curved
Pre-Helical	Horizontal Pre-Helical	Vertical Pre-Helical	Circular Pre-Helical

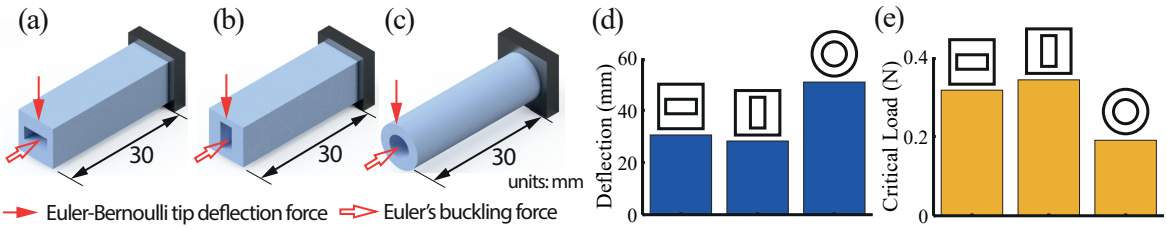

Fig. 4.2: Preliminary analysis of the SPAs response to mechanical instabilities per cross-sectional geometries. (a) Cantilever beams used in this analysis for the Horizontal, (b) Vertical and (c) Circular Straight SPAs. (d) Deflection and (e) Critical load response for each Straight SPA. The dimensions of the cross-sectional geometries are shown in Fig. 4.1(a-c). Bold arrows represent the force orientation in the tip deflection calculation and outlined arrows indicate the force orientation in Euler's buckling calculation.

4.3.3 SPAs Response to Mechanical Instabilities

When disturbed by loads, SPAs behavior will vary depending on their response to instabilities. The SPA that buckles at lower critical loads will have its chamber shape deformed by lower weights, potentially affecting its performance. Also, an SPA that shows a higher displacement in comparison to other SPAs that have been deflected under the same loads will retain less potential energy. In order to assure the selection of SPAs designs with different structural capabilities that we can compare under various scenarios, we assessed analytically the three cross-sectional geometry designs. We calculated the mechanical response of Straight Horizontal (Fig. 4.2(a)), Vertical (Fig. 4.2(b)) and Circular (Fig. 4.2(c)) SPAs to deflection using the Euler-Bernoulli tip deflection formula:

$$\delta = \frac{FL^3}{3EI} \tag{4.1}$$

where δ is the deflection of the chamber, F is the deflection force, L is the length of the SPA, E is the Young's Modulus of the silicone and I is the second moment of area of the cross-section.

To identify the mechanical resistance of the SPAs to buckling we identified their critical load using the Euler's buckling theory:

$$F = \frac{n^2 \pi^2 EI}{L^2} \tag{4.2}$$

where L is the length of the SPA, E is the Young's Modulus of the silicone, I is the second moment of area of the cross-section and n is a constant for buckling of cantilever-like beams. Although equations (4.1) and (4.2) do not consider the hyperelasticity of the material, they are a linearization of the behavior of the chambers for small loads that works as a simple way to verify the SPAs response to instabilities.

In Fig. 4.2(d), we can see that the Circular Straight chamber deflects more than the Squared Chambers. However, the Vertical Straight chamber has the highest critical load in comparison to the Circular one (Fig. 4.2 (e)). In both cases, Horizontal and Vertical performed similarly, showing that a change in orientation might produce also a different performance in our following experiments. Additionally, we confirmed that some of the SPAs have more resistance to buckling but less to deflecting. These values will be further discussed against experimental results in Section 4.6.

4.4 Methods

In this work, we analyze the performance of deflected and pre-shaped SPAs that have been submitted to variable loading conditions prior to pressurization to determine their reliability to provide a set of design principles for the development of reliable SPAs. In this section, first we describe the fabrication process of the SPAs. Second, we define the reliability requirements and assessment metrics for the analysis of the SPAs performance. Third, we predict expansion differences among the three SPAs with different cross-sectional geometries using Finite Element Modeling (FEM) in order to validate our experimental setup and FEM settings calibration. Fourth, we introduce the experimental protocol and setup we used to evaluate the SPAs. Fifth, we selected highly reliable SPAs and conducted a stress analysis using FEM in order to identify stress concentrations that might lead to failure. Finally, we conducted a statistical analysis to determine if the variation of cross-sectional geometries and chamber shapes have a significant impact into their expansion. The electronic control platform is described in Section 3.6.1.

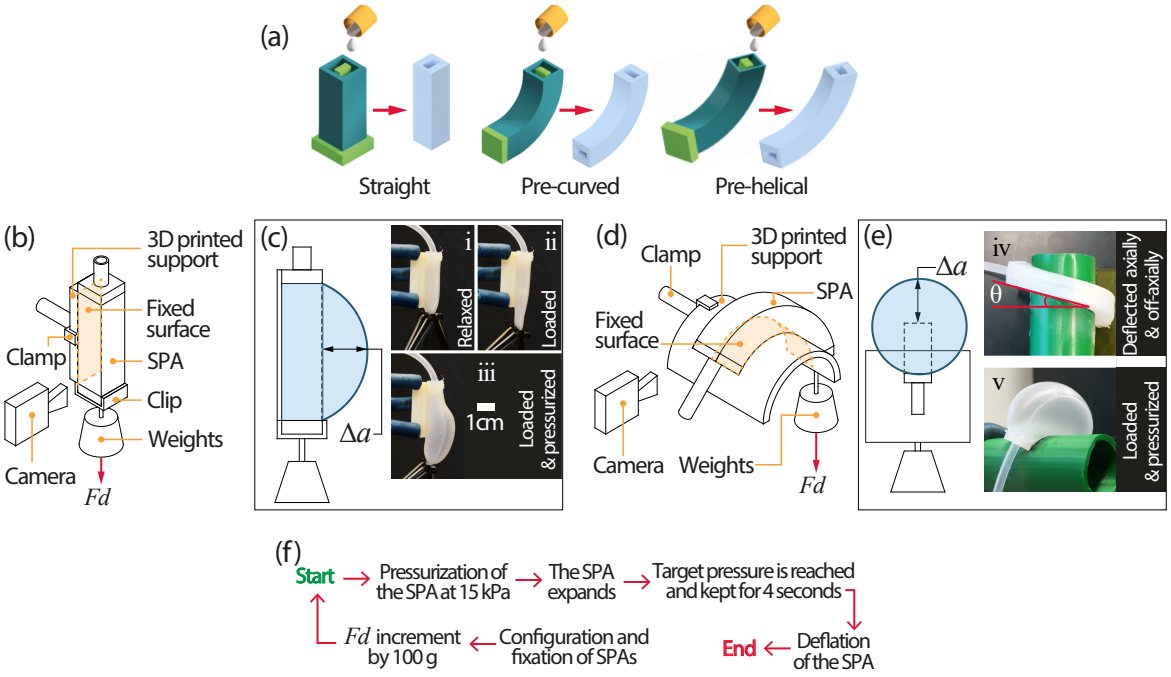

Fig. 4.3: Experimental setup and protocol. (a) Fabrication molds for casting of the SPAs. Similar molds were used to cast all the different cross-sectional geometries. (b) Isometric-view diagram of Straight and (d) non-straight SPAs, identifying the setup parts and loads (Fd). (c) Identification of Δa as the maximum expansion of Straight and (e) non-Straight SPAs. Inserts i-iii show different Straight SPAs' states, iv shows angle Θ, set to 15° for Helical and Pre-helical chambers and v shows a Pre-helical chamber loaded and pressurized. Angle Θ is kept to 0° for Curved and Pre-curved chambers. (f) Experimental procedure. We conducted experiments where Fd was 0, 100, 200 and 300 g.

4.4.1 Fabrication

ABS 3D Printed molds (Stratasys Mojo ^{TM}) were used to cast the chambers and caps of the actuators. Ecoflex 00-30 (Smooth On Inc.) was mixed and defoamed (Thinky^{TM} ARE-250 Mixer) and then poured into the molds (Fig. 4.3(a)). Prior to casting the chambers, we sprayed the interior of the molds using a release agent (Mann ®, Ease-Release 200). This avoids the chambers sticking to the molds and allows them to be removed without damage. Then, we cured them at room temperature for three hours. Next, we thermally post-cured them at 80° for two hours and then at 100° for one hour.

4.4.2 Reliability Requirements

In this study, we assess the reliability of 15 different SPAs based on their maximum expansion after being loaded and pressurized under identical conditions. The identification of the variables Fd and Δa in the setup is shown in Figs. 4.3(b,c) and Figs. 4.3(d,e) respectively.

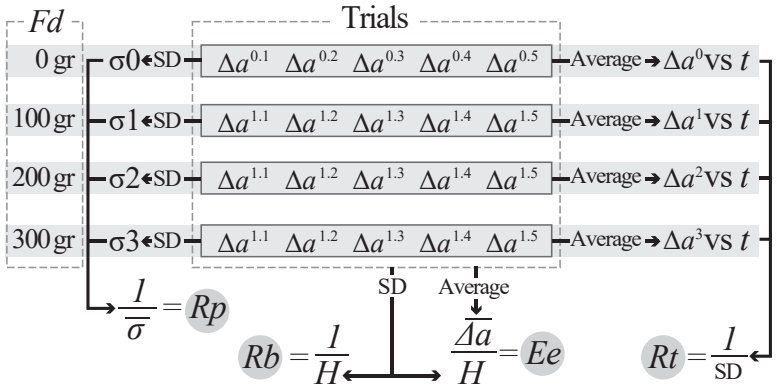

Fig. 4.4: Calculation of performance metrics for the reliability analysis of SPAs. *(Rp)* Repeatability, *(Rb)* Robustness, *(Ee)* Efficient Expansion and *(Rt)* Reiteration. Fd is the loading force. *SD* is standard deviation. H is heterogeneity of expansion. Experimental parameters of Fd and Δa are identified in Fig. 4.3(b).

We identified the following as relevant performance requirements and metrics for the design and evaluation of highly reliable SPAs (Fig. 4.4):

4.4.2.1 Repeatability

When pressurized, the SPAs should expand consistently every cycle, provided that pressure and loading conditions are identical. We quantified repeatability of each SPA by calculating the standard deviation (SD) of each group of trials (σ^0, σ^1, σ^2, σ^3 in Fig. 4.4) under the same loading conditions conditions (Fd). Then, we calculated the inverse of the average of all σ ($\overline{\sigma}$) to obtain an index of SPAs repeatability (Rp).

4.4.2.2 Robustness

When pressurized, the SPAs should expand consistently every cycle, provided that pressure conditions are identical, regardless of loading conditions varying. The higher the heterogeneity (H) of expansion, the lower the robustness. To quantify robustness of the SPAs we used the following equation:

$$R_b = \frac{1}{H} \tag{4.3}$$

Where H represents the heterogeneity of expansion as a consequence of loading introduced into the SPA, defined by the SD of all the maximum expansion measurements ($\Delta a^{0.1}$... $\Delta a^{1.5}$) across all loading conditions (Fd). A highly robust SPA will show low Heterogeneity (H) values and consequently, a high robustness value (Rb).

4.4.2.3 Expansion Efficiency

When pressurized, the SPAs should show high levels of expansion (Δa) with low heterogeneity (H). Inefficient expansion is represented by either, high expansion rates with high heterogeneity, low expansion with low heterogeneity or low expansion with high heterogeneity. We determined the efficiency of expansion of the SPAs by using the following equation:

$$E_e = \frac{\overline{\Delta}a}{H} \tag{4.4}$$

Where $\overline{\Delta}a$ is the average of Δa across all loading conditions (Fd) and H is the heterogeneity of expansion (Fig. 4.4).

4.4.2.4 Reiteration

When pressurized, the SPAs should reach their maximum expansion, in the same amount of time every cycle, provided that pressure conditions are identical, despite variations in the loading conditions (Fd).

To evaluate reiteration performance of SPAs, we correlated the time they take to reach Δa^0, Δa^1, Δa^2 and Δa^3 and the time they take to reach the target pressure plus 4 seconds. This additional time helps us to verify that the expansion pressure has reached equilibrium. A highly reiterative SPA will reach Δa^0, Δa^1, Δa^2 and Δa^3 under the same amount of time every cycle.

4.4.3 Expansion Prediction Using FEM

To predict expansion differences due to the varied cross-sectional geometries, we developed an FEM of the Horizontal, Vertical and Circular geometries with Straight chamber shape. Afterwards, we validated our models by comparing Δa (Fig. 4.3(b)) of the simulations with experimental data. We selected these SPA designs as a baseline for comparison with other SPAs as they are the most basic configuration for a pneumatic actuator. We developed the 3D models of the SPAs on Fusion360 (Autodesk®) and then, imported them into Abaqus/CAE (Simulia, Dassault Systemes™). The SPAs models were meshed using quadratic tetrahedral, 3D solid hybrid elements (C3D10H). To capture the hyperelastic behavior of silicone, we used a 3-term Ogden model with the following parameters: $\mu 1 = 0.001887$, $\mu 2 = 0.02225$, $\mu 3 = 0.003574$, $\alpha 1 = -3.848$, $\alpha 2 = 0.6632$, $\alpha 3 = 4.225$, $D1 = 2.9259$, $D2 = D3 = 0$ [4]. Boundary conditions and loads are represented in Fig. 4.5(b).

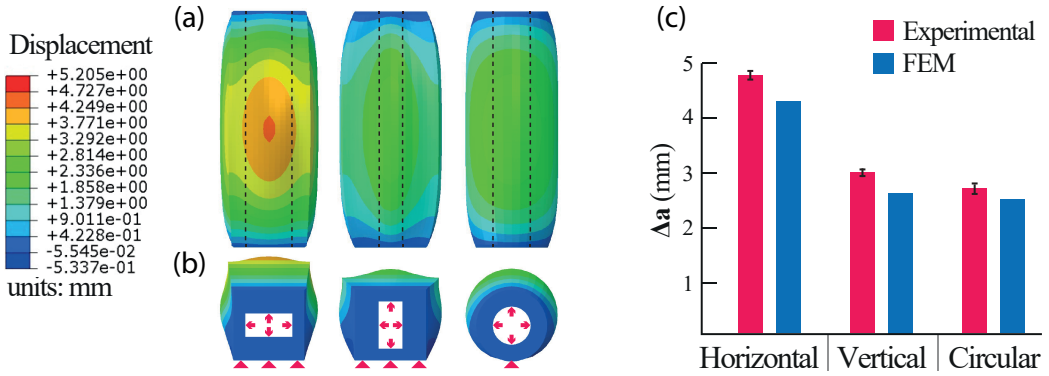

Fig. 4.5: Finite Element Analysis of the three different cross-sectional geometries in Straight SPAs upon pressurization at 15 kPa. (a) Top view showing displacement contours and (b) Front cross-sectional view showing load and boundary conditions. (c) FEM predictions and experimental results comparison.

4.4.4 SPAs Reliability Characterization

We fixed Pre-curved and Pre-helical SPAs around a rigid 3D printed supporting tube with a diameter of 30 mm using cyanoacrylate adhesive (Fig. 4.3(d)). For the Curved and Helical SPAs, we fixed the proximal end of the SPA to the supporting tube and then we manually deflected it and glued it until obtaining the desired shape, following a guiding line drawn prior the adhesion. For the Helical and Pre-helical SPAs we rotated the 3D printed tube 15° to avoid the gravity force to affect the coiling angle which is also 15° (Fig. 4.3(e) iv). For the other SPAs, this angle was kept at 0°. For the Straight SPAs, we used a flat 3D printed support and equally fixed them using cyanoacrylate adhesive (Fig. 4.3(b)). The 3D printed supports simulate environmental constraints and by gluing the lower surfaces of the SPAs to these supports we simulate inextensible layers in common SPAs. After the pre-shaped and deflected configurations were fixed, we placed a clip at the distal section of the SPAs to hang weights from them. We added those weights incrementally to serve as variable loads, from 0 to 300 g (Fd in Fig. 4.3(b,d)). These weights represent the loads that could be exerted into the system by the designer or the environment during fabrication or actuation. Afterwards, we pressurized and expanded the chamber at 15 kPa. We recorded and measured the maximum expansion Δa (Fig. 4.3(c,e)) using an image processor (ImageJ, NIH). We recognize that due to the deflection loads, the SPAs might see their chambers deformed prior pressurization. However, the inherent isotropic behavior of the silicone makes the SPAs expand equally along Δa at every axis. We conducted five trials per experiment. A diagram of the experimental protocol is shown in (Fig. 4.3(f)).

4.4.5 Stress Analysis

To provide a more complete understanding of the SPAs behavior and its possible impact in loading-related scenarios, we identified stress concentrations in their hyperelastic material as a response to expansion that might lead to failure of the SPAs by developing a static stress numerical analysis. To do this, after performing the reliability assessment of the different SPA designs (Fig. 4.7), we selected the three SPAs with the highest expansion efficiency (Ee) per cross-sectional geometry. Since it is a measure of reliability based on heterogeneity and expansion (H and $\overline{\Delta}a$ in Fig. 4.4) which are metrics of reliability frequently used in soft robotics, we decided to base our analysis on efficiency of expansion (Ee). Then, we contrasted and analyzed the stress differences between our baseline (Section 4.4.3) and the SPAs with highest Ee values Fig. 4.4(c)). The parameters and settings used in this numerical analysis are described in Section 4.4.3.

4.4.6 Statistical Analysis

To determine if the difference in expansion among SPAs is significant, we conducted a statistical analysis, where the maximum expansion $\overline{\Delta}a$ is the dependent variable. First, we ran a Shapiro-Wilk normality test to verify if the data is normally distributed. Since it was not normally distributed and given that cross-sectional geometry (circular and squared) and chamber 3D shape (Straight, Curved, Helical, Pre-curved and Pre-helical) are two independent variables with more than one variation, we proceeded to conduct a Kruskal-Wallis test with a *Bonferroni* correction and a P-value$= 0.05$.

4.5 Experimental Results

4.5.1 FEM Experimental Validation

There was a good agreement between modeling and experimental results for the expansion of the Straight SPAs (Fig. 4.5). We calculated the root-mean-square error (RMSE) between the five experimental trials and the FEM model, resulting in an average RMSE of 0.6 *mm*, 0.4 *mm* and 0.2 *mm* for the Horizontal, Vertical and Circular SPAs respectively. These results validated our experimental setup and FEM settings calibration. Additionally, this works as a benchmark for comparisons over more complex conditions, as in the stress analysis presented in Section 4.5.3.

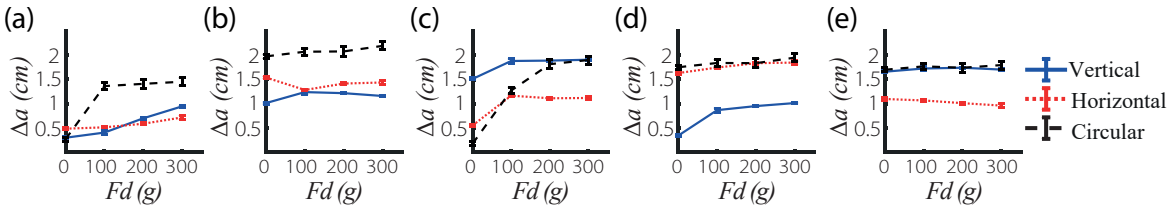

Fig. 4.6: Expansion performance of the SPAs across different chamber shapes and deflections under variable loading conditions (Fd): (a) Straight, (b) Curved, (c) Helical, (d) Pre-curved, (e) Pre-helical. Error bars represent the standard deviation out of five trials. Pneumatic pressure was kept constant to 15 kPa across all experiments

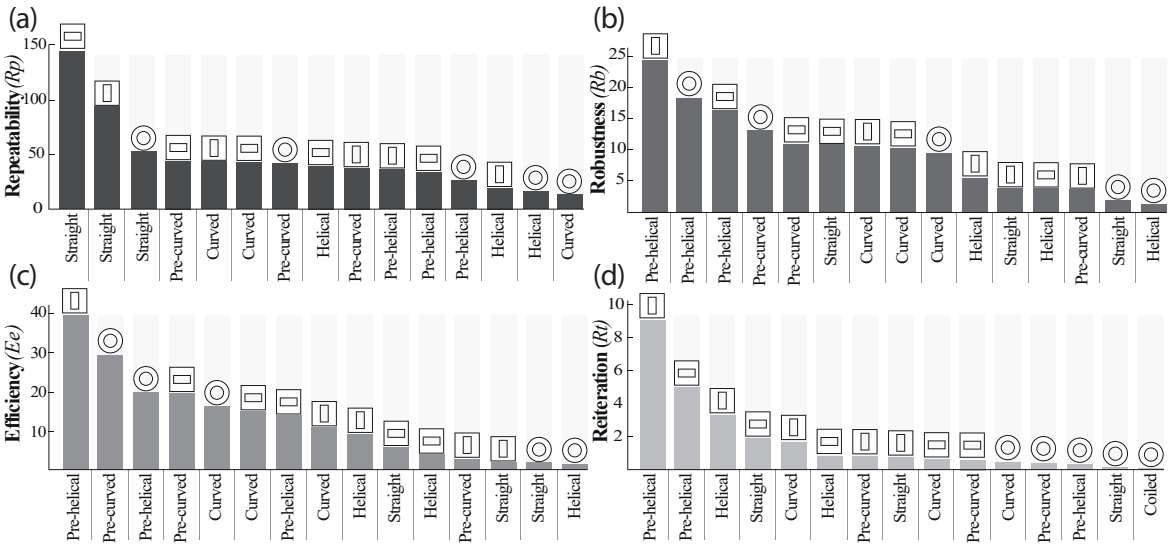

Fig. 4.7: SPAs reliability performance: (a) Repeatability, (b) Robustness, (c) Efficient expansion and (d) Reiteration.

4.5.2 Reliability Characterization

Fig. 4.6 shows that there are important differences in the performance of the SPAs with different cross-sectional geometry, shape and degree of deflection. For example, the robustness of the Vertical cross-sectional geometry is lower in a Straight chamber (Fig. 4.6(a)) than in a Pre-helical chamber (Fig. 4.6(e)), meaning that the Vertical Pre-helical SPA expansion is more consistent than the Vertical Straight Chamber regardless of the loading (Fd) conditions. Results for all the SPAs will be further discussed in Section 4.6.4. Based on the SPAs performance represented in Fig. 4.6 and using the metrics defined in Section 4.4.2 we proceeded to assess all the SPAs based on their repeatability, robustness, expansion efficiency and reiteration.

4.5.2.1 Repeatability

Fig. 4.7(a) shows a rapid decrease in repeatability, starting from Horizontal Straight down to most of the Circular geometries. Repeatability of the maximum expansion (Δa) of the Straight SPAs is higher for all the cross-sectional geometries than their otherwise shaped counterparts. Although the differences among most of the SPAs results are small and could be neglected, it stands out the contrast between Straight and Helical/Pre-helical SPAs. A way to verify in more detail these values is by looking at the error bars in Fig. 4.6. In this figure, an SPA with high repeatability will show short or almost non-visible error bars.

4.5.2.2 Robustness

Fig.4.7 (b) shows a ranking of the SPAs from the highest to the lowest levels of robustness (*Rb*), showing the Vertical Pre-helical, Circular Pre-helical and Horizontal Pre-helical SPAs as the three most robust. By looking only at their chamber type, the Vertical Pre-helical, Circular Pre-curved, Vertical Helical, Vertical Curved and Straight Horizontal show the highest levels of robustness. A way to verify these values is by identifying the straightest lines on the x axis in Fig. 4.6.

4.5.2.3 Expansion Efficiency

Fig. 4.7(c) shows a ranking of the SPAs from the highest to the lowest efficiency (Ee), showing the Vertical Pre-helical, Circular Pre-curved and Circular Pre-helical SPAs as the three most efficient in terms of expansion. By segmenting the ranking based on chamber type, the SPAs with highest efficiency (Ee) are Vertical Pre-helical, Circular Pre-curved, Vertical Helical, Circular Curved and Horizontal Straight.

4.5.2.4 Reiteration

Fig. 4.7(d) shows a ranking of the SPAs from the highest to the lowest levels of reiteration (Rt). It shows that reiteration for the squared SPAs is higher than for their Circular counterparts. The difference between the first and last SPAs in the ranking is a standard deviation of ≈ 15 seconds, making it a highly relevant parameter to consider in the design of SPAs that may suffer variable loading conditions.

4.5.3 SPAs Stress Analysis

Fig. 4.8 and table 4.2 show the Von Mises stress concentration values obtained in the developed FEM for the Straight SPAs and their counterparts with the highest efficient

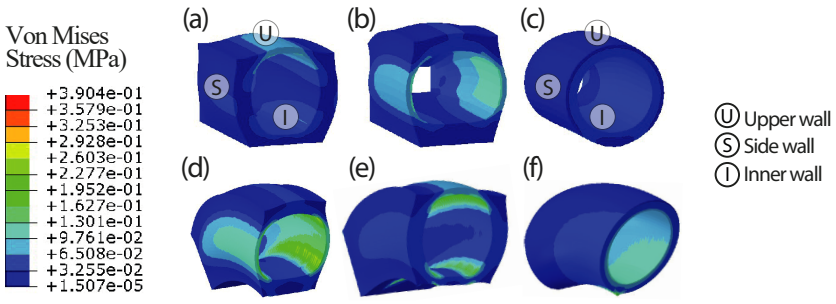

Fig. 4.8: Finite Element Analysis showing Von Mises stress contours of baseline Straight SPAs: (a) Horizontal, (b) Vertical, (c) Circular; and highly reliable SPAs per cross-sectional geometry based on the efficient Expansion (Ee) values (Fig. 4.7(c)): (d) Horizontal Pre-curved, (e) Vertical Pre-helical and (f) Circular Pre-curved.

expansion (Ee) levels per cross-sectional geometry. For this study, we focused our analysis on three sections of the SPAs: (1) Inner wall; the inner wall measurements were taken from the areas where they are more prone to fail. In the square SPAs, the inner corners of the air channel and in the Circular SPAs, the area close to the fixed surface. (2) Side wall; for all the SPA designs, the side wall is the adjacent surface to the upper and lower face. (3) Upper Wall; the upper face is the opposite side to the fixed surface of the SPA, where the maximum expansion (Δa) (Fig. 4.3(d,e)) occurs.

Except for the upper wall in Horizontal SPAs and the side walls of Vertical SPAs, these values show an overall increment in stress in the non-straight squared SPAs. In the Circular Pre-curved SPA there is an increment in stress in the inner and side wall. The upper face shows almost negligible amounts of stress for both Circular SPAs. Specifically, stress in the Horizontal Pre-curved SPA increases 700% and more than a thousand times on its inner and side walls respectively, but in the upper wall it decreases by 50% in comparison to its Straight counterpart. For the Vertical Pre-Helical SPA, stress increases by 133% and 100% on its inner and upper walls respectively, but decreases by 50% in the side wall in comparison to its Straight counterpart. In the Circular Pre-curved SPA, stress increases by 200% in the inner wall and more than thousand times in the side wall. We can conclude that, Horizontal Pre-curved showed the highest increment and overall levels of stress, located in its inner and side walls respectively, but Vertical Pre-helical showed the highest increment in its upper wall.

Table 4.2: Von Mises Stress (kPa) concentration values in FEM SPAs

	SPA Section		
SPA design	**Inner Wall**	**Side Wall**	**Upper Wall**
Horizontal Straight	32.55	0.01507	65.08
Vertical Straight	97.61	65.08	32.55
Circular Straight	32.55	0.01507	0.01507
Horizontal Pre-curved	260.3	97.61	32.55
Vertical Pre-helical	227.7	32.55	65.08
Circular Pre-curved	97.61	32.55	0.01507

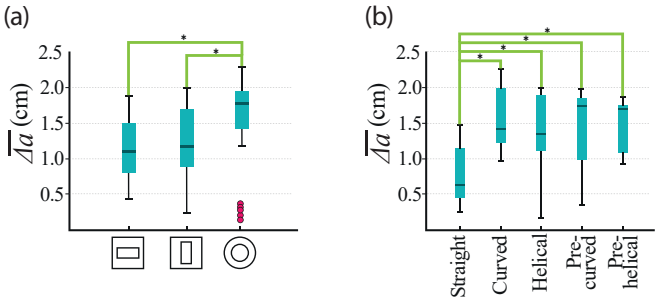

Fig. 4.9: Statistical Analysis Results for $\overline{\Delta}a$. (a) Significance among cross-sectional geometries. (b) Significance among SPAs chamber shapes.

4.5.4 Statistical Analysis Results

4.5.4.1 Significance of Cross-Sectional Geometry

The test shows that there are overall statistically significant differences between the cross-sectional geometries of the chambers in relation to their average maximum expansion $\overline{\Delta}a$ (Fig. 4.9(a)). By conducting a *Post-Hoc* test, we identified that the statistically significant difference occurs specifically between the Circular and the two squared SPAs, but is not significant between the two squared SPAs, Horizontal and Vertical. This means that varying the orientation of the squared chambers does not impact the expansion of a SPA as much as using a Circular cross-section.

4.5.4.2 Significance of Chamber Shape

The test shows that there is overall statistically significant differences among the chamber shapes in relation to $\overline{\Delta}a$ (Fig. 4.9(b)). By conducting a *Post-Hoc* test, we identified that the statistically significant difference occurs specifically between the Straight SPAs and the other

chamber shapes. This means that using a Curved, Helical, Pre-curved or Pre-helical chamber shape will not impact the expansion of a SPA as much as using a Straight shape.

4.6 Discussion

This work analyzes systematically the impact of deflection on the performance of SPAs with different chamber shapes and cross-sectional geometries under variable loading conditions to provide insights into the design of more reliable soft actuators. We selected actuators that are widely used in soft robotics based on their chamber shape (Straight, Curved, Helical, Pre-curved and Pre-helical) and cross-sectional geometries (Squared and Circular). Additionally, we implemented one variation orientation to capture its impact into their performance (Vertical and Horizontal). To provide a holistic comparative view on the behavior of the selected SPAs, we explored experimentally numerically and statistically their differences in reliability, stress concentration and significance of expansion of geometry and shape.

While previous work addresses the reliability of soft actuators from a deterministic approach, they do not consider the influence of the variations in the chamber design, cross-sectional geometry and fabrication method triads, as well as dynamic factors such as deflections and pressurization, into the assessment of reliability of SPAs. Also, despite various efforts have been made to optimize different design parameters in SPAs design, the analysis is often focused on complex, constrained or reinforced examples that could be inadvertently hiding underlying effects of the SPAs alone.

4.6.1 Conditions that Impact on Reliability

All non-Straight SPAs showed lower levels of repeatability than their Straight counterparts. This may be due to the effects of hysteresis, creep and stress relaxation and elastic energy storage in elastomeric materials, all of which are geometry and time dependant. For example, reiteration (Rt) values of the SPAs are affected by these properties. Fig. 4.7(d) shows time variation in reaching $\overline{\Delta}a$. Because a load is applied and sustained during the pressurization, we hypothesize that viscoelastic creep is affecting the robustness (Rb) and efficiency of expansion (Ee) of the SPAs, as seen in Fig. 4.7(b) and (c).

4.6.1.1 Effects of Elastic Energy Storage and Chamber Shape

In the case of non-Straight-deflected actuators (Curved and Helical SPAs), the deflection force needed to configure the actuator is stored as potential energy. This energy generates stress concentrations that might be affecting maximum expansion of the SPAs ($\overline{\Delta}a$).

However, as demonstrated in [147], even a non-deflected non-Straight actuator (such as Pre-curved and Pre-helical SPAs) tends to straighten when it is pressurized also increasing stress concentrations (Fig. 4.8).

4.6.1.2 Effects of Cross-sectional Geometry

The cross-sectional geometry of the SPAs provides resistance to deflection, buckling and other mechanical instabilities. As shown in Fig. 4.2, the squared SPAs require more force to be deflected and to be buckled. This might explain their tolerance to external loads under the same loading conditions (Fd) and their reiteration (Rt) performance in comparison to the Circular SPAs. In summary, SPAs that can reduce the effects of viscoelasticity and energy storage due to their chamber shape and cross-sectional geometry produce highly reliable actuation. An example of this is the SPA Vertical Pre-helical, which showed to be the most reliable SPA as by showing the highest reiteration, robustness and efficiency. The implication is, that the height/width ratio of its cross-sectional geometry combined with its pre-shaped chamber shape mitigates better than the other SPAs the effects of viscoelasticity and the elastic energy stored into its structure. The relevance of the height/width ratio is visible as the Horizontal Pre-helical SPA was ranked in a lower position than the Vertical Pre-helical SPA for all the requirements (Fig. 4.7).

4.6.2 Statistical Analysis

The conducted statistical analysis concluded that the difference in maximum expansion between the squared and Circular SPAs is significant. The resistance of the SPAs to mechanical instabilities shows a similar conclusion (Fig. 4.2). This supports our previous assumption (Section 4.6.1.2) on the effects of the cross-sectional geometry into the SPAs performance. The statistical analysis also concluded that the maximum expansion ($\overline{\Delta a}$) of Straight chambers is significantly different from all the other chamber shapes. This supports our assumptions on the effects of elastic potential energy (Section 4.6.1.1). Although there is no significant difference among the maximum expansion ($\overline{\Delta a}$) of all the non-Straight SPAs and between Horizontal and Vertical SPAs, we recommend to select one or another chamber shape or geometry based on their final application and the corresponding confidence interval based on standardized metrics, such as safety factors, repeatability, robustness and reiteration.

4.6.3 Stress Concentrations

The developed FEM highlights local stress concentrations that provide visualization of possible failure areas in the SPAs. It has been demonstrated that the geometry of the cross-

section of a pneumatic chamber impacts on the stress distribution and consequently on global actuator performance [161]. In this Chapter, we demonstrated that the shape of the SPA also has an important impact on the stress concentration. In the presented scenarios, curving and coiling Straight SPAs with Horizontal, Circular and Vertical cross-sectional geometries increase the overall risk of failure. It is well known that rounded angles show higher average load carrying capacity than square right angles. In this study, we illustrated that by curving and coiling the Straight chambers. As a result, some sections of the SPAs increased in stress concentration by more than a thousand times (Section 4.5.3). We relate that increase to the effects of elastic energy storage described previously (Section 4.6.1.1). Circular SPAs are more likely to fail in the areas close to the inextensible surface because its contact surface is reduced in comparison to the squared SPAs. However, despite its limitations in reliability, Circular SPAs show the lowest stress in their bodies, potentially allowing them to reach higher expansion rates without failing than their squared counterparts.

4.6.4 Design Principles

The results and analysis previously discussed in addition to supporting literature cited in Section 4.2 provide the basis for the following design principles of highly reliable SPAs.

Straight SPAs Yield higher repeatability than other deflected and pre-shaped SPAs: Although the maximum deviation of expansion was 1 mm (Circular Helical SPA), there are tasks in which repeatability of expansion is non-trivial for the correct function of the system, as in surgical applications using laparoscopic instruments [171]. In these cases, Straight SPAs may provide better outcomes, specifically, Horizontal SPAs, which showed an average deviation of only 0.06mm. Nevertheless, it is important to consider the trade-off in efficiency. For instance, Circular Curved, which $\overline{\Delta}a$ is $> 300\%$ higher than for the most repeatable SPA, has an average deviation of only 0.72 mm, which could be enough if for example, it is implemented in an industrial soft gripper. We recommend to verify regulatory, operational and safety parameters that determine the degree of precision required by the system.

Pre-shaped SPAs increase efficiency in comparison to deflected SPAs: Provided that deflections of the main body of the SPAs can be avoided, these will show overall higher efficiency than deflected SPAs. This can be confirmed by Fig. 4.7(c), where most of the pre-shaped SPAs are better ranked than the deflected SPAs. We assume that the reason for Vertical Pre-curved to be poorly ranked is the height-width ratio of the inner channel affecting its resistance to instabilities such as lateral-torsional buckling, and therefore, its performance. We suggest to keep the fabrication shape as

close as possible to the final-use shape to avoid deflections that could be transformed into stored energy and residual stress. An example of implementation of this principle is pure-motion actuators, as their extended, expanded or twisted configurations are often a scaled version of their relaxed state.

Pre-helical SPAs increase robustness in comparison to Pre-curved and deflected SPAs Provided that the environment in which the actuator will perform and the application allows it, SPAs should be fabricated as Helical chambers. As can be seen in Fig. 4.7(b), the Pre-helical SPAs showed the highest robustness. Specifically, the Vertical Pre-helical SPA showed to have the highest robustness, which also showed high reiteration and the highest repeatability among the Pre-helical SPAs. As in the previous requirement, we assume that Vertical Pre-curved performance is affected by the height-width ratio of its inner channel. It is important to consider the trade-off regarding other reliability requirements. For example, in the case of the Circular Pre-helical, the second best SPA in robustness, it performs poorly in reiteration. We assume this happens due to the lower resistance of the Circular SPAs to mechanical instabilities. An example of the implementation of this principle is the design of actuators that have to carry variable loads. By using Pre-helical SPAs, they can lift these loads potentially minimizing variability of expansion.

Straight Horizontal SPAs are potentially more reliable than traditional Straight Circular SPAs for axial deflections Straight SPAs that bend due to their inextensible layer can benefit from having a cross-sectional geometry as in the Horizontal SPA studied in this Chapter. Its efficiency and robustness is as optimal as the traditional Circular Curved SPA, but with a higher repeatability and reiteration. An example of implementation of this principle is the design of modular soft robots that use bending sections to steer their motion. By using Straight Horizontal SPAs with an inextensible layer, these robots can potentially follow a path with higher repeatability, efficiency and robustness than using any other SPA presented in this work.

4.7 Conclusion

There has been a general oversight of a systematic design and performance analysis of SPA's as building blocks. Several publications [53, 171, 108, 229] have expressed a prevalent need to enhance soft robots reliability as a conduit for improved design, fabrication, modeling and control of these systems. In this article, we quantify the reliability performance of three SPA designs with different actuation response to deflection to provide a set of design

principles that address the challenges of developing soft robots with predictable and reliable behaviour. We identified three main factors that impact SPAs reliable performance: (1) viscoelasticity of the SPAs' material, (2) elastic energy storage related to the SPAs chamber 3D shape and deflections and (3) the SPAs cross-sectional geometry. To overcome the negative effects of those factors such as low repeatability, time-wise inconsistent inflation and inefficient expansion, designers should select the optimal triad of cross-sectional geometry, chamber shape and fabrication method (deflected or pre-shaped chambers) depending on the requirements of the system. By using the proposed rankings in Fig. 4.7 and applying the design principles into the development of soft robots, designers will be able to make informed decisions prior to the actuators fabrication. Although there can be a larger spectrum of chamber variations different from the SPAs presented within this work, the proposed methodology serves as a guideline for the assessment of most SPA design providing the soft robotics community with a useful tool for soft robots design. Further studies will include the development of a constitutive model for the prediction of the stress–strain relations, quantification of elastic potential energies to provide further depth into its effects on reliable performance and replication of the analysis to cover other SPA types, such as braided soft actuators.

Chapter 5

Hyper-elastic Ballooning Membrane Actuators: The Soft, Yet Resistant Actuators for Tissue Repair

5.1 Preface

In Chapter 4, we analyzed systematically the design of the Soft Pneumatic Actuators (SPAs) used as building blocks in the SoPHIA (Chapter 3) and variations in their geometry and configuration to evaluate their reliability and response to variable loads. As a result of this analysis conformed by numerical, statistical and experimental procedures we provided a set of design principles that contribute to the design of more reliable SPAs (Section 4.6.4).

In this Chapter, we introduce the development of a series of numerical models to guide the design optimization of the SoPHIA, building on the results of the analysis conducted in Chapter 4 as a strategy to optimize the extension and strength capabilities shown in Chapter 3. Finally, we propose, fabricate, test and validate two devices whose designs are based on highly reliable SPAs that will enable higher extension rates in soft robotic implants for tissue regeneration. This Chapter addresses objective E described in Section 1.3. The content of this chapter and its appendix has been published in the following research article:

- E. Perez-Guagnelli, and D.D. Damian. "Hyperelastic Membrane Actuators: Analysis of Toroidal and Helical Multifunctional Configurations". *Cyborg and Bionic Systems*. 2021, (Conditional Acceptance).

Where E. Perez-Guagnelli designed, fabricated, characterized and numerically modelled the actuators. J. Jones characterized, analyzed and discussed the strength capabilities of the actuators and develop the empirical prediction model. D.D. Damian supervised the research.

5.2 Introduction

Soft robots are highly compliant and conformable systems made of materials with similar mechanical properties to those of living tissues [173]. They can perform different motions by combining hyperelastic materials with inextensible substrates or by pre-programming them into their geometries, such as axial extension [124], radial expansion [52] or twisting [225]. These properties provide them with several advantages over conventional rigid robots that have proven to be a compelling alternative to current strategies for the development of medical technologies, such as interacting safely with humans [151]. There has been an increasing interest for the development of medical robots and their components using hybrid soft and semi-soft (a combination of hyperelastic and elastic materials into one system) [229] based approaches, for either, outside of the human body as exosuits [8, 176], or inside, as implants [167]. However, most of these technologies have been focused on wearables [25] that work outside of the body [151] and devices for minimally invasive procedures [171], particularly endoscopic tools [186] and catheters [103]. Robotic implants are devices that can be placed on a target organ or tissue inside of the body to deliver mechanical stimulation based on controlled forces and displacements. The majority of soft robotic implants have focused on treating heart failure [167, 174], however, these types of devices have the potential to assist in the delivery of a number of therapies.

Regenerative medicine can particularly benefit from the compliance and mechanical support that soft robotic implants can provide. Examples of how this technology can be applied in the field of tissue regeneration include: (1) promoting tissue growth of tubular organs of the gastrointestinal (GI) tract caused by congenital defects, such as Long-Gap Esophageal Atresia (LGEA) [67] (Fig. 5.1(a)) or Short Bowel Syndrome (SBS) [188] (Fig. 5.1(b)); (2) To regenerate GI tract tissue after partial resections as a treatment for cancer.

It has been demonstrated that robotic implants that promote tissue regeneration via mechanostimulation in long-term therapies are a promising alternative to traditional approaches in tissue engineering or robot-assisted surgery. Recently, a robotic implant for tissue regeneration in the GI tract was proposed by our group [43]. This implant was capable of growing esophageal tissue up to 77% by exerting a constant force of ~ 2.5 N over nine days. However, fibrotic response occurred due to the interaction of the rigid parts of the implant with the organ. To decrease fibrotic response, our group developed a flexible version of that implant [10], capable of exerting up to 4 N of force and to comply to deflections of up to 3 cm. Nevertheless, despite having flexible components they are still relatively rigid, potentially not able to decrease fibrosis optimally.

Recent findings demonstrate that fibrosis can be reduced if the surface stiffness of medical implants matches the stiffness of the tissue where they reside [29]. Therefore, we introduced

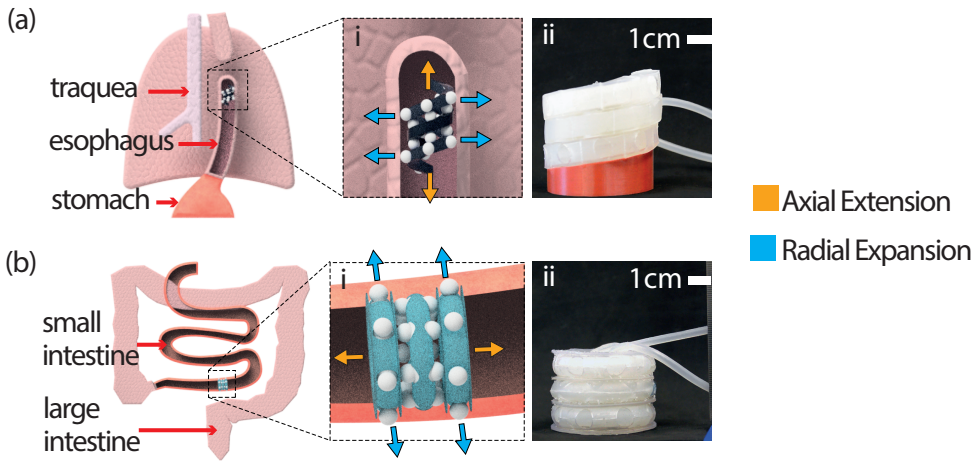

Fig. 5.1: Envisaged application of the Multi-Modal Hybrid (M2H) and Hyperelastic Ballooning Membrane Actuators (HBMAs). Potential implantation of the M2H-HBMAs inside tubular organs, such as (a) the esophagus (b) and small intestine to treat long-gap conditions. i, detail conceptual views of the helical and toroidal M2H-HBMAs. ii, the manufactured M2H-HBMAs in a relaxed state. Arrows in the diagrams represent the two motions that the M2H-HBMAs can produce, axial extension and radial expansion.

an entirely soft robotic implant for tissue regeneration via mechanotherapy, capable of axially extending 36%, exerting forces up to 7 N and standing loads of 800 g under pressurization without buckling. Although this design advances existing tissue repair strategies, tissue shortage severity can vary, imposing more drastic tissue elongation and mechanical resistance challenges, which derive into the following requirements:

Axial Extensibility: To be able to treat different ranges of tissue shortage and therefore reduce the gap between the two stubs or regenerate tissue in a tubular organ affected by, for example, a resection or congenital defect, the design of these new actuators should allow them to highly extend. These actuators should be able to displace from a few to tens of centimeters to support the GI tract. By extending, the actuators will exert traction forces to the host organ and elongate the tissue where it resides (Fig. 5.1). Although the extension of the actuators is only relevant if they are capable to exert forces to promote cell proliferation, providing them with high axial extensibility can potentially cover a wider range of severities in tissue-shortage conditions. In our previous work (Chapter 3) we introduced a soft actuator capable of axially extending 36% by pressurizing both of its pneumatic chambers configured in a four coil structure. In this work, we advance those axial extensibility capabilities by achieving higher axial extension while pressurizing only one pneumatic chamber and needing only one coil or level in its configuration (Fig. 5.2).

Multi-modal: Physiological behaviour of human organs involves morphological changes caused by specific anatomical functions, such as peristalsis, performed by the longitudinal and radial muscles in the gastrointestinal tract. To provide anatomically congruent stimulation during mechanical treatment of tubular organs and decrease the risk of pathological responses, the design of these new actuators should provide stimulation on multiple-degrees of freedom simultaneously and independently. Given that one envisaged application for the new actuators is to be used inside tubular organs, additionally to being able to axially extend, they should be capable of radial expansion (Fig. 5.1). In this way, the implants could reduce fibrosis by providing massage to the walls of the host organ [83]. Although our previous work (Chapter 3) introduced an actuator that features multi-functionality, this capability came at the expense of interdependent actuation between its modules, which made accurate control of the device difficult. Here, we advance this feature by providing each of the modules with independent and negligible non-pure motion.

Modularity: To increase versatility in their applications across different clinical needs, as well as to adapt to specific anatomical or therapeutical conditions, specialized medical devices should adopt modular strategies. This allows the system to be configured according to the physical requirements of the area where it will reside or the therapy to be performed. In this Chapter, we advance the concept of modularity through coiling presented in Chapter 3 by introducing a module-stacking approach that allows the assembly of its modules as required.

Structural strength: Devices that provide mechanical support and stimulation inside the human body, for example in mechanotherapeutical treatments, need to sustain and exert forces for several weeks [43]. Therefore, they should be capable of resisting considerable loads, while maintaining their structure and softness, preventing the system from collapsing, buckling, damaging its surroundings or misshaping the target organ. They should also be capable of extending under loaded conditions in order to stimulate the tissue itself. The actuator previously introduced (Chapter 3) was capable of standing an axial load of 800 g without buckling. In this work, we introduce two new actuators that exceed the load-bearing capacity of our previous design and we demonstrate their ability to extend under loaded conditions at low pressures.

Although there have been investigations that provide relevant approaches to address one or two of the previously described requirements, the design of soft robotic implants for tissue regeneration via mechanostimulation must comply to all of them. Martinez, *et al* [124] proposed a paper-elastomer composite pneumatic actuator capable of axially extending 250%

and standing up to 1 kg of weight without buckling. Despite its impressive axial extension and load-bearing capabilities, its morphology does not allow for multi-function, a crucial requirement for the physiological well-being of the target organ during mechanotherapy treatment. Digumarti, *et al* [52] designed a soft pneumatic actuator based on the principle of bellows, that axially extend and radially expand up to 450% and 80% respectively. However, its radial expansion is only an effect of its axial extension, preventing the device from providing independent axial and radial stimulation, critical in mechanotherapy. Meng, *et al* [128] designed pneumatic honeycomb-like modular pneumatic structures, capable of axially extending and bending. By adding up to five modules to the structure, the actuator can enhance its extension capabilities. Despite this actuator fulfilling the requirements of axial extensibility, modularity and structural strength impressively, it could not provide radial stimulation, preventing its use in mechanotherapy. A promising approach was introduced by Blumenschein and Mcngüç [21], in which 3D printed bellow actuators unfold to extend up to 340%. Although this principle has the potential to provide motion in multiple degrees of freedom thanks to its assembly modularity, its working principle does not allow a cylindrical configuration with an empty luminal space, a critical feature for implantation of these type of devices. Lindenroth, *et al* [113] introduced a pure-extension fluidic actuator that can extend 49% and exert up to 34.83 N/mm of force. Despite its impressive force capabilities, this actuator cannot provide multi-modal actuation and is entirely wrapped in a stiff material that may trigger fibrotic response. Cianchetti, *et al* [36] introduced a manipulator that can axially extend 86.3% and exert 41.4 N of force, but it was not capable of providing independent multi-modal actuation.

By encoding the capabilities provided by the compliance of the aforementioned requirements into the design of two novel Multi-Modal Hybrid (M2H) actuators we introduce the following contributions to this area of research: (1) Introduction of the concept of stacked Hyperelastic Ballooning Membrane Actuators (HBMAs) realized by 3D arrangements of ballooning membranes; (2) a series of numerical analyses to define the M2H-HBMAs design features; (3) proposal of two modular and versatile tubular actuators designs, helical and toroidal, based on HBMAs, capable of hyper extensibility and load-bearing; (4) experimental characterization and validation of the two types of soft actuators.

5.3 Materials and Methods

In this section, we describe the conceptual design, actuation approach, numerical and experimental analyses we conducted to address the design requirements previously described, as well as to validate and empirically predict the performance of two novel M2H-HBMAs.

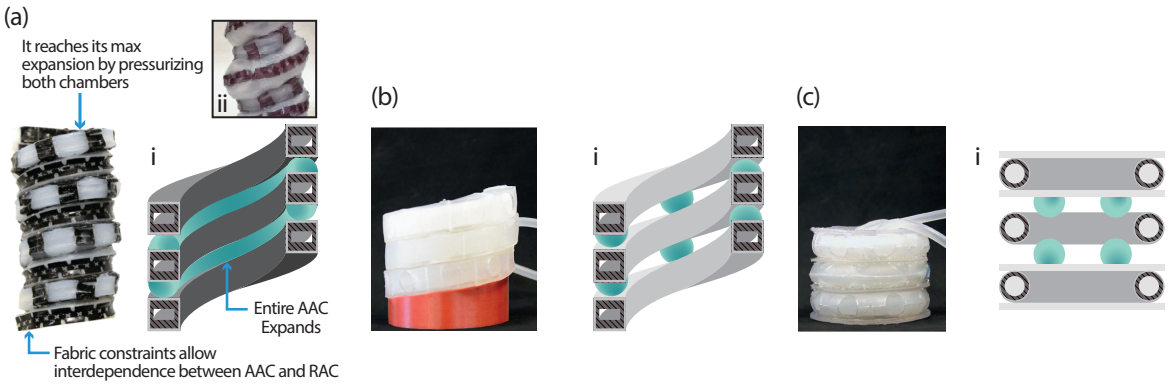

Fig. 5.2: Overview of the design advancements for linear extensibility from (a) our previous work (Chapter 3) and (b) the HBMA-based helical and (c) toroidal actuator configurations presented in this Chapter. Inserts i show a cross-sectional view of the actuators and their AAC extension principle. Insert ii shows a detail view of this principle in reality.

5.3.1 Conceptual Design of the M2H-HBMA

We introduce the concept of stacked Hyperelastic Ballooning Membrane Actuators (HBMAs) [80] in orchestrated 3D expansions, which can be realized using two configurations: helical (Fig. 5.3(e)) and toroidal (Fig. 5.4(e)). Membrane ballooning has been extensively researched in material and mechanical engineering [205, 64, 19], mainly in regard to phenomenon modeling and actuation technologies. However, their capabilities in configurable 3D expansions has not been yet addressed. We are using this fundamental membrane ballooning phenomenon with two notable advantages: (1) to compose versatile and load-bearing designs using 3D spatially combined ballooning membranes; (2) to provide those designs with hyperextensibility at reduced initial volume. By restraining the HBMAs isotropic expansion deterministically using a semi-soft exoskeleton, the Helical (HA) and Toroidal Actuators (TA) are provided with axial extension and radial expansion capabilities. The modules with axial extension capabilities are referred to as Axial Actuation Chambers (AAC). The modules with radial expansion capabilities are referred to as Radial Actuation Chambers (RAC). The exoskeleton can be a flat substrate [80] or 3D structure, but in this work we will cover the latter. Based on the concept of stacked HBMAs and the previously described requirements, we designed two multi-modal actuators (M2H-HBMAs), which conceptual design we describe next. Dimensions and cross-sectional geometries of both M2H-HBMAs are based on our previous work (Chapter 4) and were selected a cm scale for ease of fabrication and because of their simple design they may be scaled up or down easily in future works. Additionally, we conducted a series of numerical analyses to define the M2H-HBMAs design features, such as the comparison between two of the most used unconstrained openings, circular and squared

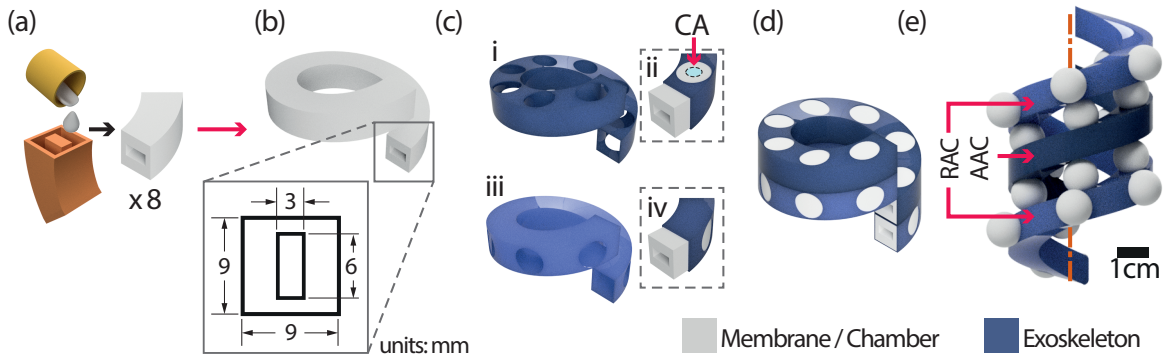

Fig. 5.3: Helical configuration of the stacked balloons concept to shape the Helical Actuator (HA). (a) Fabrication mold for casting of the units that conform to (b) the helical chambers and a detailed view showing the dimensions of their cross-sectional area. (c) The exoskeletons for the (i) AAC and (iii) RAC. Inserts ii and iv show how we introduced the elastomeric units into the exoskeleton for the AAC and RAC respectively. (ii) To assemble AAC and RAC, we glued the centre of the AAC membranes to the stacked RAC exoskeleton using chemical bonding (CA). (d) The assembled Helical Hybrid Actuator (HA). (e) Conceptual image of the HA actuated with one turn of the AAC and two turns of the RAC.

(Section B.1), and to evidence the behavior of the silicone chambers of both actuators without the inclusion of a semi-soft exoskeleton (Section B.3).

5.3.1.1 Helical Configuration

The Helical Actuator (HA) is shaped out of two helical chambers (Fig. 5.3(b)) made of 8 sections (Fig. 5.3(a)) encased into a semi-soft exoskeleton (Fig. 5.3(c)) to form the Axial (AAC) and Radial (RAC) Actuation Chambers (Fig. 5.3(e)). The conceptual design of this helical actuator is based on our previous work (Chapter 3). In this Chapter, we advance the fabrication and extension principles by applying an improved HBMAs approach (Section B.1). When pressurized, the membranes in the AAC expand and shape two balloons, on the top and bottom of the chamber. These balloons displace the stacked levels in the helix, extending it axially. When pressurized, the membranes in the RAC expand and shape balloons in the radial direction ((Fig. 5.3(e)).

5.3.1.2 Toroidal Configuration

The Toroidal Actuator (TA) is shaped out of toroidal chambers ((Fig. 5.4(b)) encased in a two-part semi-soft exoskeleton to form the AAC and RAC (Fig. 5.4(c)). Following the concept of stacked balloons, the TA axially extends by expanding balloons out of its AAC, displacing the stacked RACs. Similarly to the HA, when pressurized, the membranes in the TA's RAC expand and shape balloons in the radial direction ((Fig. 5.4(e)). There are

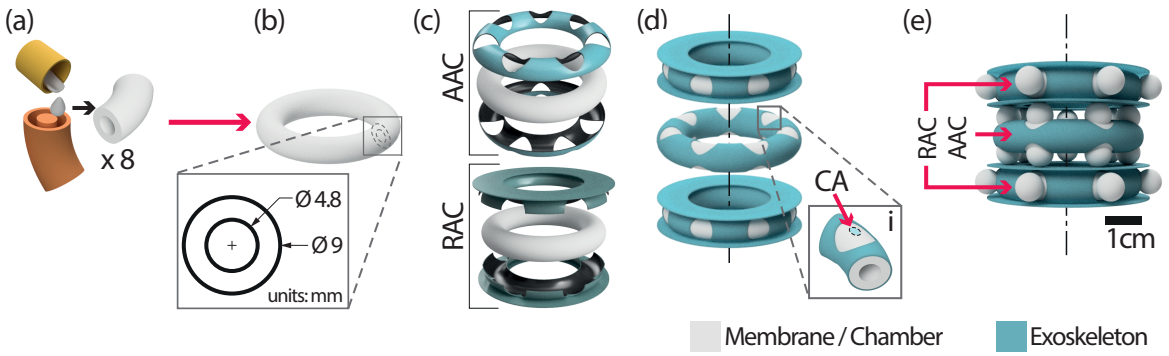

Fig. 5.4: Toroidal configuration of the stacked balloons concept to shape the Toroidal Actuator (TA). (a) Fabrication mold for casting of the units that conform (b) the toroidal chambers and a detail view showing the dimensions of their cross-sectional area. (c) Exploded views of the different parts that conform the toroidal AAC and RAC. (d) Exploded view showing the assembled independent chambers. Insert (i) shows that to bond the different chambers, we glued the AAC membranes to the RAC's exoskeleton using chemical bonding (CA). (e) Conceptual image of the TA actuated with one AAC and two RACs.

two conceptual differences related to modularity between the HA and TA: (1) in the HA, the height and number of coils depends on the uncoiled length of the two chambers that shape the helix (Fig. 5.4(b)) while in the case of the TA, it will depend on the amount of independent units stacked (Fig. 5.4(d)), therefore, one turn in the HA corresponds to one unit in the TA. This equivalence is useful to describe the setup used in Section 5.4.1.3. (2) Given that the HA relies on only two strands that shape the whole actuator's body, only two air inlets are needed, while in the TA, each unit requires an independent inlet, supplied with air from a common input, independent for the AAC and the RAC. These air input configurations allow the M2H-HBMAs to perform independent and simultaneous axial extension and radial expansion. Diagrams describing the locations of the air inlets are shown in Fig. B.8 of the Supporting Materials.

5.3.2 Fabrication Procedure

After defining the conceptual design for the HA and TA based on the design features numerical analyses (Sections B.1 and B.2 of the supporting material) and requirements described previously, we proceeded to fabricate them. PLA 3D printed molds (PRUSA, i3 mk3s) were used to cast the chambers and caps of both actuators. Ecoflex 00-30 (Smooth On Inc.) was mixed and defoamed (Thinky ARE-250 Mixer) and then poured into the molds (Fig. 5.3(a) and (Fig. 5.4(a)). We cured them at room temperature for four hours. Then, we thermally post-cured them at 80°c for two hours and then at 100°c for one hour. After the post-curing process is complete, we bonded the different sections of the helix and

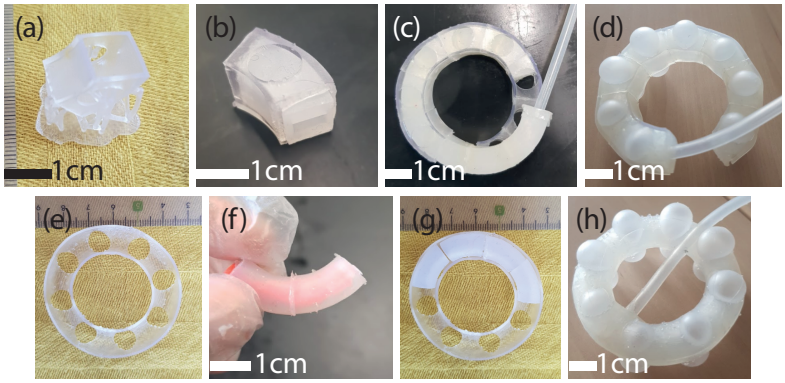

Fig. 5.5: Fabrication procedure. (a) 3D printed HA's exoskeleton section. (b) HA's silicone chamber section inserted into the exoskeleton section. (c) elastomeric chamber being inserted into the exoskeleton bonded units and (d) an actuated HA's AAC. (e) 3D printed TA's exoskeleton section, (f) toroidal silicone sections being glued using a guiding insert. (g) Demonstration on how the toroidal sections fit into the exoskeleton section before bonding and encasing them to shape an AAC. (h) An actuated TA's AAC.

torus (Fig. 5.5(b,f)) until shaping the entire chambers (Fig. 5.3(b) and (Fig. 5.4(b)) using uncured silicone. Because adding extra layers of silicone to an elastomeric chamber can create stiffer sections and cause heterogeneous expansion, the bonded surfaces are covered by the exoskeleton, while the ballooning membranes remain unaffected. The exoskeletons were 3D printed out of an elastic resin (Fig. 5.5(a,e)) with a Shore hardness 50A (Form2, FormLabs©), a Young's modulus of 2800 MPa and a Poisson's Ratio of 0.43. To assemble the silicone chambers with their respective exoskeletons we followed different processes, described next.

Assembly of the Helical Actuator: To assemble the parts of the helical actuator, we introduced the silicone chamber into the exoskeleton and pulled gently from one end (Fig. 5.5(c)). To make this procedure easier, we oiled the chamber with vacuum oil, so it reduced the friction between the silicone and the exoskeleton. After the chamber was placed into the exoskeleton, we sealed both ends and added a medical grade silicone tube as an air inlet that allows pressurization (Fig. 5.1(d)). Finally, to bond the different coils in the helix and to ensure the AAC's balloons push the stacked chambers, we added a drop of cyanoacrylate adhesive between the AAC's membranes and the RAC's exoskeletons (Fig. 5.3(c)ii).

Assembly of the Toroidal Actuator: To assemble the parts of the TA, we encased a toroidal chamber between the two parts of the AAC and RAC exoskeletons (Fig. 5.5(g)). Then, they were sealed using cyanoacrylate adhesive. Finally, we bonded the AAC (Fig. 5.5(h)) and RAC units in the same manner as described previously for the HA (Fig. 5.4(d)i).

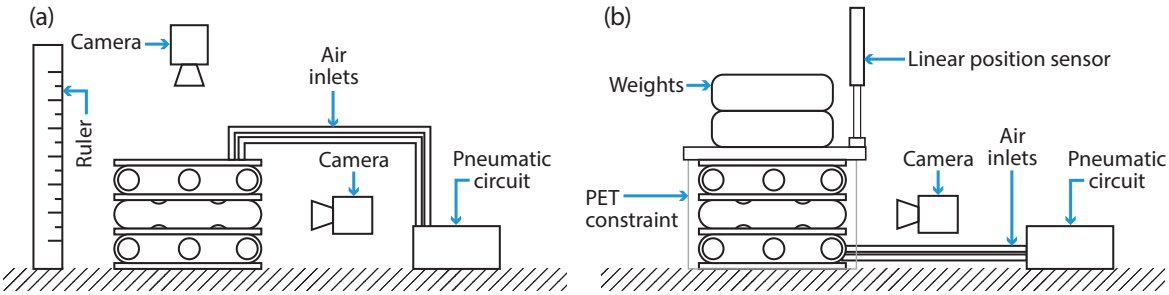

Fig. 5.6: Experimental setups. (a) Axial extension, radial expansion and intraluminal deformation experiments. The upper camera was only used on the latter. (b) Structural strength experiments. For simplification, only the TA is shown in the diagrams, but the conditions were identical for the HA. Please, find a more detailed description of the setup used in this set of experiments in [80].

5.3.3 M2H-HBMAs Characterization

We conducted a set of bench-top experiments to characterize the extension, multi-modality capabilities and structural strength of the two M2H-HBMAs. In this section, we describe the corresponding setups and protocols.

5.3.3.1 Control Platform

The control system is composed of a primary printed circuit board that houses the microcontroller, communication and power input, while modular circuit boards contain the pneumatic components for each of the pneumatic chambers: axial (AAC) and radial (RAC). Each of these chambers are inflated and deflated by dedicated DC pumps and closed solenoid valves respectively. Pressurization of each chamber is triggered by a position proportional integral controller and tracked by Honeywell (ASDXAVX005PGAA5) pressure sensors. Further details about the pneumatic control platform can be found in [156].

5.3.3.2 Extension Capabilities

In this set of experiments, we measured the freeload elongation of the HA and TA when pressurized from 14 kPa with steps of 2 kPa until they failed to find their maximal axial extension. We define the failure point as when the M2H-HBMAs break either at the exoskeleton or membrane level. After reaching each target pressure, it was kept for 4 seconds to ensure the system reached equilibrium. Since its base is not flat, we added an adaptor to the HA to avoid slanted extension (Fig. 5.7 (c)). We performed five trials. Extension was recorded and then measured using ImageJ (NIH) (Fig. 5.6 (a)).

5.3.3.3 Pure-motion Capabilities

The M2H-HBMAs are envisaged to be used as multi-modal implantable devices, therefore, their motions should be able to be carried out simultaneously and independently without affecting the physiology of the organ where they reside. For this reason, we conducted two studies. First, we pressurized the RAC of both M2H-HBMAs at 18 kPa. After reaching each target pressure, it was kept for 4 seconds to ensure the system reached equilibrium. Then, we recorded and measured the axial extension provided by the expansion mode of each M2H-HBMAs. Second, since we envisage the use of M2H-HBMAs to internally or externally repair tubular organs, its intraluminal deformation is a relevant feature to test under actuation. Therefore, we activated the extension and expansion modes in both M2H-HBMAs and recorded their behaviour from a top-view. Then, we measured the changes in their intraluminal area out of five trials. Both studies were recorded and then analyzed using ImageJ (NIH). A diagram for the entire setup used in the experimental characterization of the actuators is shown in Fig. 5.6(a).

5.3.3.4 Structural Strength

Finally, since the HA and TA need to exert and sustain forces over a long period of time when used as mechanotherapy implants, their structural strength is an important feature to test. Therefore to compare the behaviour of both actuators under varying loads we first conducted a study in which the actuator was initially pressurized and weights were incrementally added. Following on from this, a second study was conducted in which the weights were incrementally added before pressurization, to evaluate the extension of the actuator in active motion under external loads. In the two experiments, the AAC only of both the HA and the TA was used and pressurized to 24kPa. The actuators were also radially constrained by a sheet of PET to simulate the clinical environment in which they would exert these forces. The displacement of the actuator was measured using the experimental setup from [80] (Fig. 5.6 (b)). The experiments were repeated six times.

5.3.4 M2H-HBMAs Extension Prediction

Having designed, fabricated and tested the HA and TA, we proceeded to predict their extension capabilities using a Finite Element Analysis modeled in Abaqus/CAE (Simulia, Dassault Systemes^{TM}). This was a multi-step analysis, under pressure loads from 14 to 24 kPa with steps of 2 kPa, identical to the experimental protocol described in Section 5.3.3.2. The silicone chambers models were meshed using a quadratic triangular, 2D planar shell elements (CPS6M). To capture the hyperelastic behavior of silicone, we used the Ogden

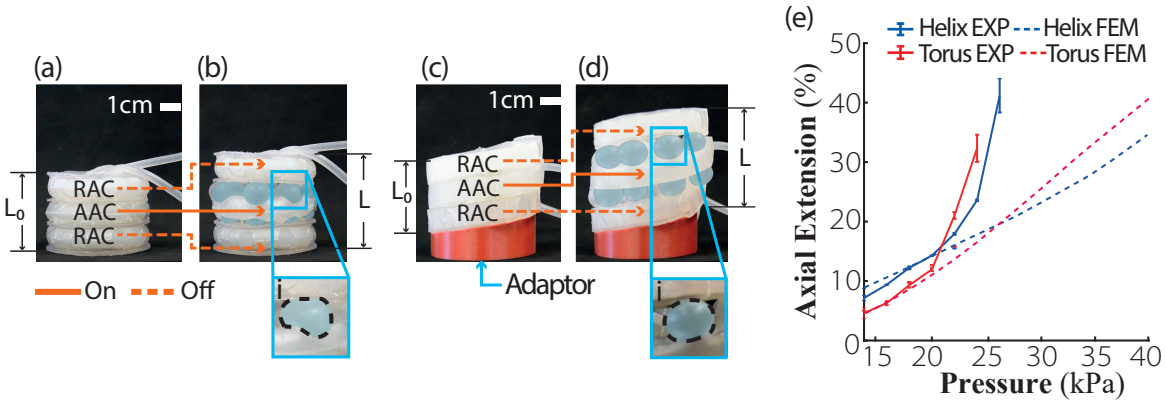

Fig. 5.7: Characterization of extension capabilities of the M2H-HBMAs. (a) The relaxed and (b) pressurized TA at 24 kPa. (c) The relaxed and (d) pressurized HA at 26 kPa. (e) M2H-HBMAs extension capabilities comparison and Finite Element Modeling (FEM) results.

material model, with parameters described in [4]. The exoskeletons were modeled using the mechanical properties provided by the manufacturer, described in Section 5.3.2. These settings were kept constant across all simulations using 2D planar shell elements. In this test, we measured the total axial extension of the two M2H-HBMAs under free-load conditions, considering gravity, density and weight of each of their elements. Additionally, using the same settings, we measured the stacking effects on extension by calculating the decrease on the expansion of the ballooning membranes per stacking level, using three levels for both M2H-HBMAs. Evaluated geometries and boundary conditions for the numerical analysis are described in Figs. 5.8(a,c).

5.4 Results

5.4.1 M2H-HBMAs Characterization

5.4.1.1 Extension Capabilities

The TA extends up to 32% (13 mm) (Fig. 5.7(b)) with a maximum standard deviation of 2.28% (0.9 mm) before failing at 24 kPa of pressure. The HA extends up to 41% (16 mm) (Fig. 5.7(d)) with a maximum standard deviation of 2.85% (1.08 mm) before failing at 26 kPa of pressure.

If the axial extension module (AAC) was to be used separately, its axial extension capacity increases by $>140\%$ and $>170\%$ for the TA and HA respectively (Fig. B.9). All percentages of extension presented throughout this work were calculated using this formula: $\frac{L-L_0}{L_0} * 100$, where L is final length and L_0 is initial length of the actuators. Fig. 5.7(e) shows a plot

that compares the M2H-HBMAs axial extension capabilities and their numerical modeling. We calculated the root-mean-square error (RMSE) between the experimental trials and the numerical model, resulting in an average RMSE of 8% and 13% for the TA and HA respectively. We assume that the differences between the experimental and numerical results correspond to the simplicity of the numerical model (Fig. 5.8(a-d)) and human error during fabrication. This limitation is further discussed in Section 5.5.2.

5.4.1.2 Impact of the Actuators' Weight on Balloons

As can be seen in Fig. 5.7(b) and (d), the upper balloons expand more than the lower balloons in both AAC for the HA and TA. This is more evident in the TA. Therefore, with the objective of testing if this corresponds to a physical phenomenon or simply fabrication errors, we proceeded to measure the displacement differences between the upper and lower balloons at different AACs of multilevel M2H-HBMAs using the same settings in a numerical model as for the extension prediction reported in Section 5.4.1.1. Fig. 5.8(g) and (h) verify our observations, also showing that the difference between upper and lower balloons is higher for the TA than for the HA, and that these results prevail when stacking more levels.

5.4.1.3 Numerical Extension Prediction

Fig. 5.8 (e,f) shows the stacking effects on axial extension affecting all the levels of three-leveled stacked M2H-HBMAs. The axial extension of the TA's and HA's AACs is decreased by $\sim 4\%$ and $\sim 3.7\%$ respectively per added level.By using the results from our experimental (Section 5.4.1.1) and numerical data for one and multiple stacking levels we can empirically predict the amount of extension per number of stacked levels, assuming every level keeps the configuration seen in Fig. 5.8 (a,c), where the two M2H-HBMAs have two RACs and one interlayered AAC. This can be done using the following equation where E is the amount of extension for an actuator with N levels:

$$E = X - (N-1)D/2 \tag{5.1}$$

where X is the percentage of extension for one level (Fig. 5.7) and D is the unit of decrease in extension of the first level in a two-level actuator (Fig. 5.8(e,f)). This effect is assumed to be constant and is multiplied by the number of upper levels each level has. Fig. 5.8(i) provides an empirical prediction of the extension for multiple levels of an actuator.

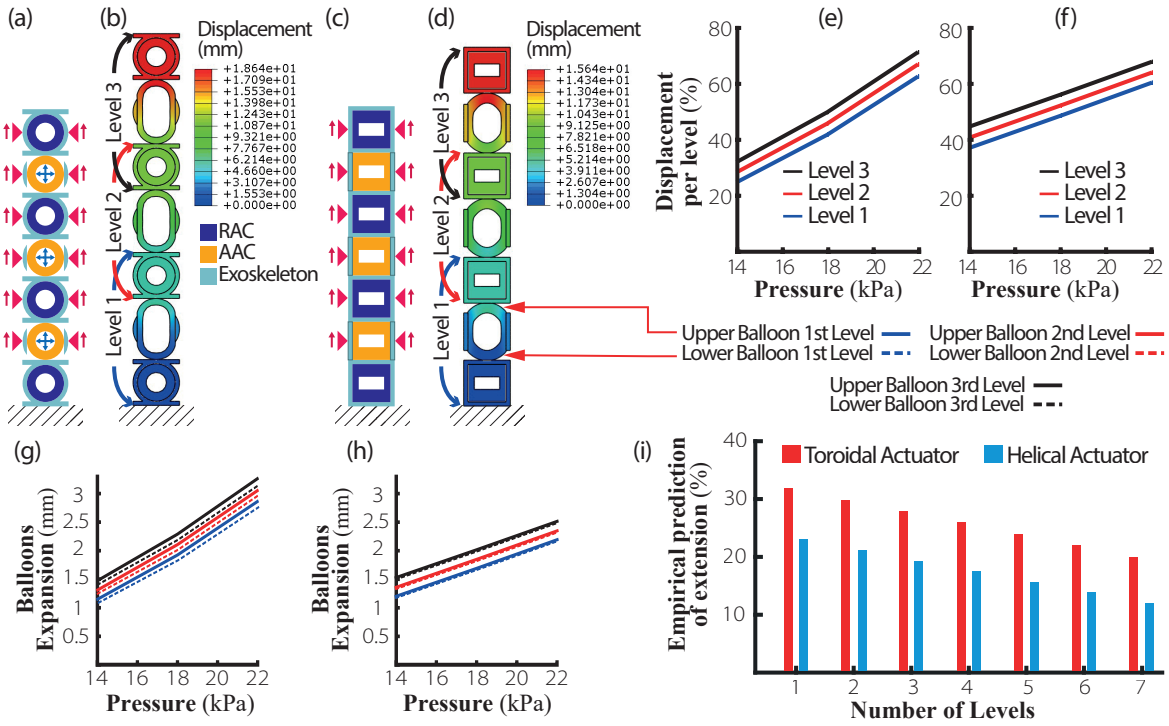

Fig. 5.8: Numerical analysis of the extension capabilities of the M2H-HBMAs. (a,c) Geometry, boundary conditions, load identification and (b,d) numerical analysis results for the TA and HA respectively. The axial displacement of the (e) TA's and (f) HA's AACs per level. (g) Plots showing the differences in displacement between upper and lower balloons for every level in the stacked TA and (h) HA . (i) Empirical prediction of the M2H-HBMAs axial extension with additional stacked levels.

5.4.1.4 Pure-motion Capabilities

The M2H-HBMAs are envisaged to perform specific functions in the body, therefore, their motions should be able to be carried out independently to avoid affecting the therapy and for easier control. By pressurizing the RAC of the HA, the actuator axially extends only 0.5%, while the TA extends by only 1.9%. The intraluminal area of the MHBAs is deformed by 4.8% and 2.3% in the HA and TA respectively (Fig. 5.9). These results show a negligible non-pure expansion and intraluminal deformation. Section B.3 in the Supplementary Materials shows the behaviour of the helical and toroidal chambers without exoskeletons, which evidences the efficiency of the M2H-HBMAs exoskeletons designs to allow ballooning membranes (Fig. B.9) to expand over 300% without deforming the overall structure.

5.4.1.5 Structural Strength

The TA shows the best performance of the two M2H-HBMAs, with over 150% maximum extension for both the pre-loaded and post-loaded conditions compared to a maximum

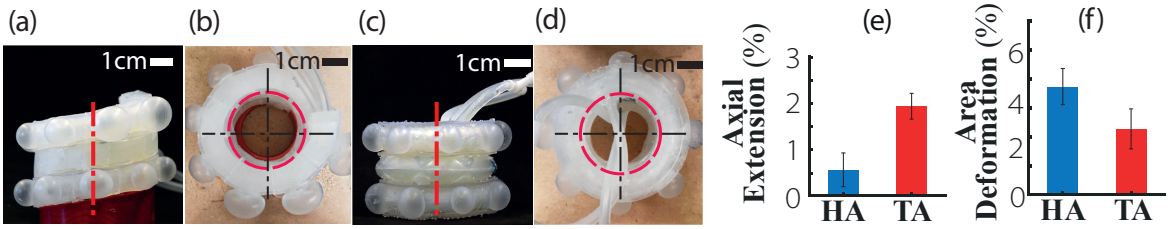

Fig. 5.9: Pure-motion capabilities. (a) The HA and (c) TA, with their RAC pressurized at 18 kPa. (e) Change in extension as a result of expansion for the TA and HA. (b) Top-view of the HA and (d) TA pressurized at 24 kPa (AAC) and 18 kPa (RAC). (f) Intraluminal area deformation as result of expansion and extension for the TA and HA.

extension of 115% for the HA (Fig. 5.10(c)). The TA is also capable of greater extension when pre-loaded with extensions of more than 150% as compared to less than 30% for the HA. The HA and TA both perform better when post-loaded, showing and maintaining greater extension under heavy loads, demonstrating extensions of 60% and 160% with 1 kg loads respectively compared to less than 20% extension for both when pre-loaded with 1 kg. Finally, the extension of the TA is considerably more consistent for the post-loaded condition showing an average drop of around 15% extension from 0 kg load to 1 kg load compared to around 160% for the pre-loaded condition.

Fig. 5.10 (d,e) shows the extension of the HA and TA under gradual pressurization to 24 kPa. Both the HA and TA require pressures of around 15 kPa to begin extending under no load conditions. For the TA, as the load increases, the input pressure needed to begin extension also increases, from around 15 kPa under no load to around 20 kPa for 0.4 and 0.6 kg loads. A similar behaviour is observed for the HA, although much less distinct due to the poor overall extension.

5.5 Discussion

We introduced two novel Multi-Modal Hybrid Hyperelastic Ballooning Membrane Actuators (M2H-HBMAs), capable of axially extending, radially expanding and load-bearing resistance with negligible intraluminal deformation and a modular design that can be adapted to different anatomical and therapeutical needs. We envisage the use of these actuators as rehabilitation wearables, when mechanical stimulation is needed outside of the body, or internally, as implants for tissue regeneration. Although various publications address the challenges in the trade-off of force vs softness, and pure-motion vs multi-modality, they do not synthesize the benefits of axial extensibility, multi-modality, modularity and load-bearing capabilities into one design approach, that can be arranged in more than one configuration, as in the TA

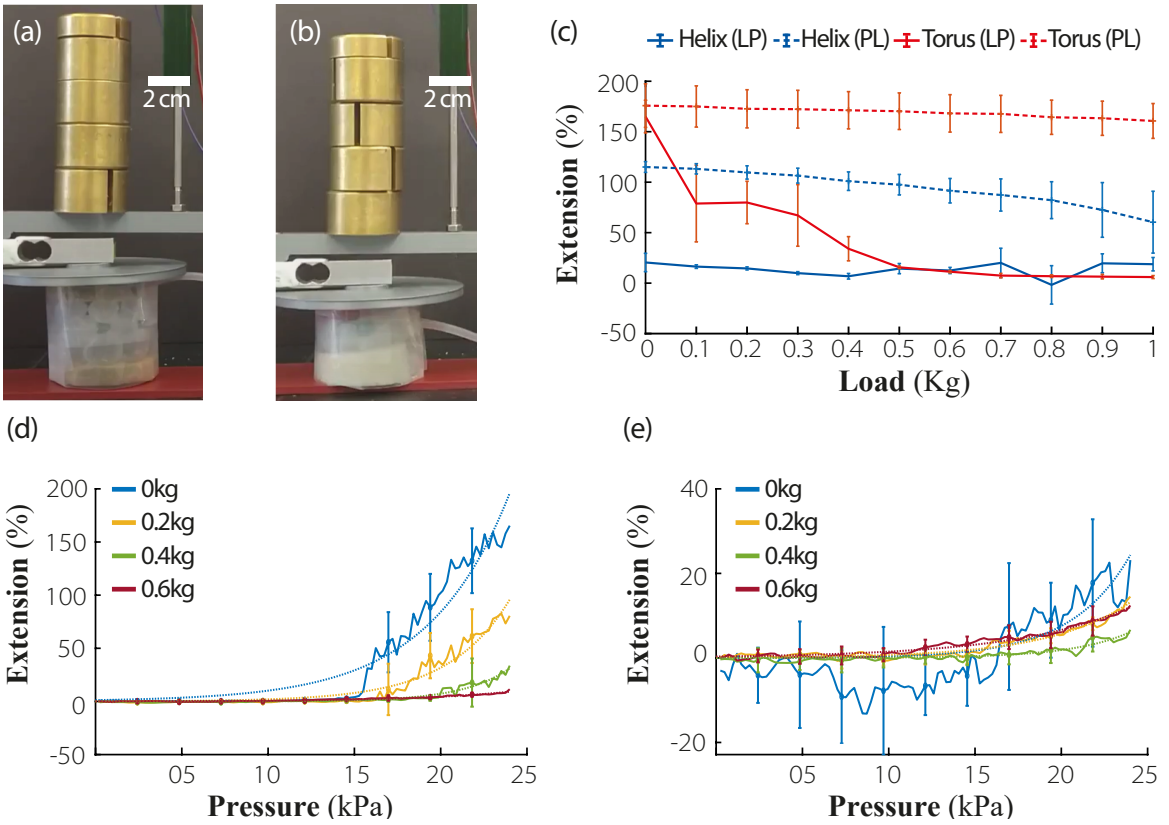

Fig. 5.10: Structural Strength Test. (a) The TA and (b) HA pressurized at 24 kPa and then loaded by 1 kg. (c) Plot showing the axial extension capabilities of the M2H-HBMAs under varying loads and under two conditions: Loaded and then pressurized (LP) and pressurized and then loaded (PL). (d) Extension of the TA and (e) extension of the HA for gradual pressurization to 24 kPa under loads of 0, 0.2, 0.4, and 0.6 kg. The solid lines represent the averaged data with the error bars representing the standard deviation across six trials. The dashed lines represent an exponential curve-fit.

and HA. In Chapter 3, we have demonstrated it is possible to provide a device with such capabilities, however, in this work we advance all of those requirements as described next (Fig. 5.2).

5.5.1 Requirements Compliance

Axial Extensibility: we used a numerical analyses to design, analyze and predict the behaviour of the two M2H-HBMAs, as well as experimental characterization to validate and describe their capabilities. The Helical (HA) and Toroidal (TA) Actuators can axially extend up to 41% and 32% respectively, by activating only one actuation chamber.

The two Radial Actuation Chambers (RAC) in one level of the M2H-HBMAs are passive modules during axial extension. Therefore, if we derive the obtained axial extension values considering the thickness of the ballooning membranes we obtain that the membranes

showed 250% and 300% of extension in the HA and TA respectively. If we consider L_0 as the elastomeric chambers we obtain an extension of 120% and 150% in the HA and TA respectively (Fig. B.9). Because of this, we envisage the development of hyper-extensible machines applying the HBMAs principle and the M2H actuators stacking modules approach.

Modularity: By numerically calculating the decrease in extension per added level and experimentally validating its expansion capabilities we were able to empirically predict the axial extension for both M2H-HBMAs if we add additional modules (Fig. 5.8). These results validate the compliance to the modularity requirement, as demonstrate that the system is still functional and capable of providing high extensibility under multilevel configurations, making it versatile to be adapted to different anatomical or therapeutical needs. We also envisage the use of different modular combinations to provide, for example, pure-expansion only using RACs, or pure-extension using only AACs without the weight of RACs affecting this motion. Additionally, we see the potential to implement bending motions to the TA and HA by selectively pressurizing membranes in the M2H actuators, although this would require to adapt the air connections to this application. We recognize that the re-configurability of the modules is limited by the need to bond them using cyanoacrylate in the current setup, classifying the M2H-HBMAs as Assembled Modular Soft Robots [228]. However, we envisage that designers and clinicians will be able to pre-configure the modules to fit their needs before bonding, making use of the M2H-HBMAs modularity principles.

Multi-Modality: the M2H-HBMAs demonstrated exertion of non-pure extension of only $< 2\%$ and 1% when the RAC is pressurized for the TA and HA, and an intraluminal area deformation of $< 2.5\%$ and 5% when both, the RAC and AAC are pressurized for the TA and HA respectively. These results demonstrate the efficacy of the semi-soft exoskeleton in constraining expansion of the silicone chambers, as it is highlighted by Fig. B.6 in the Supplementary Materials and providing multi-modal capabilities to the M2H-HBMAs, while keeping softness in their structure.

Structural Strength: the M2H-HBMAs showed the ability to extend when loaded before and after pressurization with up to 1 kg (Fig. 5.10 (c)). Both the HA and the TA were able to withstand greater loads whilst maintaining extension levels when loaded after pressurization, showing good structural strength once pressurized. When pressurizing under load, the TA performed better, showing greater active motion under external loads. The difference in extension when pre-loaded could be from a more uniform distribution of the load across the balloons of the actuator in the TA or from the different cross-sectional shape of membrane, with the load only being in contact with the top of the balloon for the circular cross-section in the TA compared to the whole area for the square cross-section in the HA. It has been demonstrated though that tubular tissues tend to comply to the exerted force

which could allow both the TA and HA to achieve full extensibility irrespective of loading [43]. The extension of the actuator could also be increased through greater pressurization when constrained and under heavier loads, as the level of required input pressure to induce extension was shown to be greater for heavier loads (Fig. 5.10 (d,e)). Finally, in the clinical setting the traction forces exerted on the tissue will also depend on the attachment methods used as an interface between the actuator and the organ [154].

5.5.2 Future Directions

Resilience: the type of forces required to promote tissue growth are still unknown. However, as mentioned in Section 5.2, D. Damian, *et al* [43] achieved the elongation of esophageal tissue in-vivo, providing relevant quantitative data, that we can use to assess the applicability of the M2H-HBMAs, such as the actuators having operated ~ 9 days inside the body to elongate 77% while exerting a constant force of ~ 2.5 N. Recurring actuation during those 9 days may lead to weakening or bursting of the soft matrices internal walls, causing failure. We acknowledge that, although the robots presented in this work could provide real-time information about their extension, force and pressure conditions in bench-top tests, their use inside the body would be affected by the aforementioned disadvantage. Nevertheless, different approaches have been developed by the soft robotics community to overcome this challenge and make soft robots resilient, such as self-healing techniques [169] and advanced proprioceptive sensing strategies [79] that could be adopted in future works.

Biocompatibility: the materials used to fabricate the M2H-HBMAs were selected due to their inherent compliance, stretching capacity, ease of use, low cost, high availability and versatility that allow rapid prototyping, however, they are not biocompatible, which prevents its use in direct contact with organs and tissues. There are two approaches to overcome this limitation and expand the reach of this work outside of proof-of-concept: (1) encapsulation and (2) replacement of the elastomeric matrix using a biocompatible material, such as silastic [43].

Fabrication: although the manufacturing process steps are straight-forward and well defined, they require performing manual procedures that might compromise the reliability of the system, such as bonding the AACs membrane to the RACs surfaces (Fig. 5.3(c,ii) and 5.4(d,i)) or assembling the exoskeletons (Fig. 5.5(a)). Using multi-material additive manufacturing technologies to print simultaneously chambers and exoskeletons can overcome this challenge.

Exoskeleton stiffness/extension dependency: the modular approach used in the TA is not affected by the mechanical properties of its exoskeleton as long as it has a higher elastic modulus than its silicone chamber and membranes. However, the stiffness of the HA's

exoskeleton and its extension capabilities are interdependent. Decreasing the stiffness of the HA exoskeleton, for example, by varying its wall thickness or material's shore hardness might achieve higher or lower axial extension rates. This is caused by the resistance of the helix to increase or decrease its pitch. An analytical model that expresses the relationship between the HA's pitch behavior and axial extension as function of its exoskeleton stiffness can overcome this challenge.

Implant-to-tissue forces evaluation: while the M2H-HBMA's axial extension is promising and although we have demonstrated that the M2H-HBMAs can sustain at least 1 Kg of force while axially extending this should be evaluated in function of the forces that they can apply to biological tissue in order to confirm that their design is capable of addressing the mechanotherapy requirements. Furthermore, in order to fully demonstrate the suitability of the M2H-HBMA's design as a tissue repair tool we need to evaluate their reliability over several weeks [43].

In conclusion, we have designed and conducted a series of numerical analyses to define the M2H-HBMAs design features and experimentally validated the design of two M2H-HBMAs that can sustain considerable loads and provide pure-extension motions with minimal intraluminal deformations. These actuators achieve axial extension by using a hyperelastic ballooning membrane principle in combination with a stacked balloon approach in helical and toroidal configurations. We envisage the use of these tools to assist tissue repair or function recovery in surgical, implantable and wearable applications by providing mechanical stimulation to the limb, organ or tissue where they are placed. Future work includes: (1) a systematic study of the effect of external forces on the actuator, (2) ex-vivo testing to analyse tissue and organs response to mechanical stimulation provided by the M2H-HBMAs, and (3) the development of an analytical model to describe their behaviour.

Chapter 6

Discussion

This work proposes an approach for the development of implants, that combines the capabilities of regenerative medicine and the field of robotics, to overcome the clinical and technical challenges of designing a physiologically, anatomically, metabolically and mechanically compatible smart and safe device for tissue regeneration and growth. Growing tissue via mechanotherapy has shown to overcome the limitations of poor patient variation, vascularity and lack of organ multi-layer repair capabilities in tissue engineering, and, despite the limitations of mechanical treatments of specificity, selectivity and timeliness, by applying robotics techniques, a controlled therapy regimen that overcome those limitations can be provided. Traditional robots are made of stiff components that may be unsafe to use within the human body. On the other hand, soft robotics, a branch of the field of robotics, has shown to develop technology that safely interacts with humans due its low (young's) modulus that matches the ones in human organs and tissues. This strategy has shown to assist in the decrease of fibrotic response, improving the regenerated tissue quality. Based on this approach and the design criteria for the development of regenerative robotics (Section 1.2), this thesis have achieved the objectives laid out in Chapter 1, as detailed below:

A. To design, fabricate and validate a soft actuator that can be can be configured in versatile geometries.

B. To configure a soft robot able to provide multi-modal functions that can be implanted through minimally invasive procedures.

C. To develop and validate a control scheme that regulates the behaviour of the robot's multi-modal functions.

D. To analyze, characterize and validate the reliability performance of the building blocks of a multi-modal soft robot under variable loads and configurations.

E. To design, optimize, characterize and validate the capabilities of the robot based on the integrated knowledge.

6.1 Fulfillment of Objectives

6.1.1 Objective A and B

In Chapter 3, we described the conceptual design, fabrication, analytical modeling, experimental characterization and simulation of an entirely soft robotic implant for tissue regeneration. By using a geometrically simple building block (actuation chamber) that can be coiled from a one to a three-dimensions actuator, we were able to configure mechanically compliant pneumatic modules into a cylinder that fits to various diameters of hollow organs and tubular tissues, making it a versatile medical tool. By varying the orientation of the chambers, we can address different conditions. For example, the RAC could be oriented to expand inwards in order to stimulate the intestine during SBS treatment (Appendix A.3). It can also be oriented to expand outwards during LGEA treatment. The helical shape also provides interlayered multi-modal function to yield extension and expansion, as well as structural support, with air pressure distributed uniformly across the diameter and height of the actuator. We showed that the implant can support up to 800 g without buckling. This feature is clinically important as buckling could lead to a misshaped organ. Furthermore, extension and load-bearing capabilities were further investigated and optimized in Chapter 5 to provide the implant with the capacity to treat more severe atresias and resections. By the fulfillment of these objectives, we have met the requirements of safety and universality described in Section 1.2.

6.1.2 Objective C

In Chapter 3, we introduced a proportional–integral control based pneumatic system, capable of pressurizing each of the two chambers that make up the implantable device, simultaneously and independently. By doing this, we were able to provide the SoPHIA with multi-modality, autonomy and programmability, fulfilling the clinical requirements of multi-functionality and controlled operation. Additionally, we developed a staged-position gain-scheduled controller, which emulates the daily tissue stretch within the existing clinical treatment, keeping a steady-state error of less than 1 mm that provides safe operation for the envisaged clinical procedure and successfully validated the implant control in a physiologically-relevant scenario.

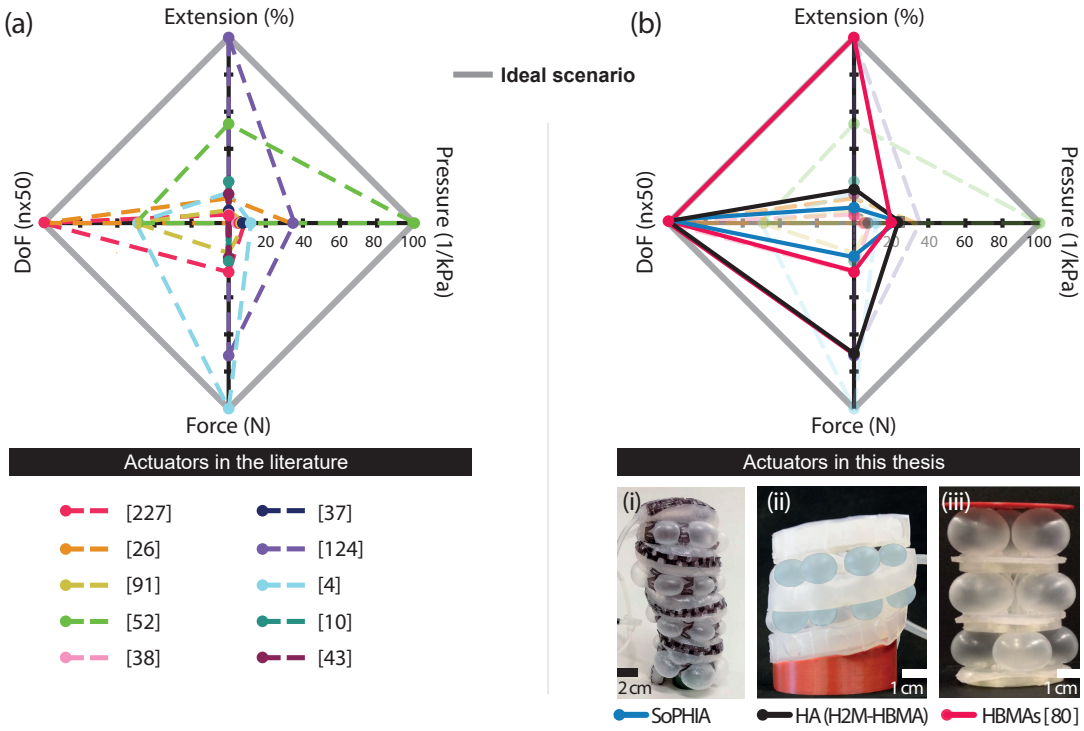

Fig. 6.1: Radar plots comparing the performance of (a) existing soft actuators in the literature vs (b) the actuators presented in this thesis. Metrics values are normalized to a scale from $0-100$ for clarity of comparison, evaluating each of the actuators in the literature based on their reported capabilities in their respective publications . Inserts i and ii show actuators described in Chapters 3 and 5 respectively. Insert iii shows an HBMAs actuator developed by our group using only membranes, which show its potential for high axial extension [80].

6.1.3 Objective D

In Chapter 4, by performing numerical, analytical and statistical analyzes and validating them experimentally we quantified the reliability performance of three SPA designs with different actuation response to deflection under variable loading conditions. Based on the study results, we provided a set of design principles that address the challenges of developing soft robots with predictable and reliable behaviour. We identified three main factors that impact SPAs reliable performance: (1) viscoelasticity of the SPAs' material, (2) elastic energy storage related to the SPAs chamber 3D shape and deflections and (3) the SPAs cross-sectional geometry. The proposed set of principles provide designers with a useful tool for soft robots design to overcome those effects and provided me with design insights for the optimization of the soft robotic implant for tissue regeneration developed in Chapter 1.

6.1.4 Objective E

Due to their compliant nature, soft robots typically present a trade-off between the force they can exert or the load they can sustain and the range of motion they can provide [231, 128], which may limit its use as a regenerative tool via mechanostimulation. In Chapter 5, we introduced the design, fabrication, testing and numerical and experimental validation of Multi-Modal Hybrid (M2H) Hyper-elastic Ballooning Membrane Actuators (HBMAs) that help to overcome those limitations, superseding the capabilities of the SoPHIA and all the actuators in the literature, as, to the best of my understanding, there are no soft robots with high extension, expansion, modular and anti-buckling capabilities embedded into one structure. In Fig. 6.1, we show a comparison between the actuators presented in this work and actuators in the literature [227, 26, 91, 52, 38, 37, 124, 4, 10, 43] that are able to produce at least an extension motion plus one of the previously mentioned capabilities. The considered performance metrics are (1) extension: percentage of axial extension. (2) Pressure: Amount of pressure (kPa) needed to achieve the highest extension. (3) Force: either the amount of force (N) that the actuator is able to exert axially or its load-bearing capacity. (4) Multi-modality: the number (n) of motions that the actuators are capable to perform without modifying their axial shape, e.g. bending, as in soft grippers and manipulators. Fig. 6.1 highlights the technical impact of the research conducted in this work.

M2H-HBMAs are actuators based on the design principles proposed in Chapter 4 that consist of expandable elastomeric membranes in semi-soft exoskeletons configured as toroidal or helical structures. By deterministically placing areas for the membranes to expand axially and radially, the M2H-HBMAs can extend and expand respectively. These actuators feature modularity, to adapt its design to different physiological and therapeutical needs; multi-modality, to provide anatomically congruent stimulation; and to maintain shape under external forces. The helical and toroidal M2H-HBMAs are capable of extending 34.7% and 25.8% more respectively than its SoPHIA (normalized to one coil for consistency) counterpart. The M2H-HBMAs were also able to sustain $>$ 1Kg of axial load, 25% higher than the SoPHIA. The extension improvement validates the use of the design principles proposed in Chapter 4 as a useful tool for the design of soft robots and provides the soft robotic implant for tissue regeneration via mechanostimulation with enhanced capabilities in comparison with its SoPHIA version. Another important improvement between the SoPHIA and the M2H-HBMAs is that the former required simultaneous pressurization of its chambers and to have 4 turns in its structure to achieve $>$ 30% of extension, while the latter supersede those extension rates only with one turn (level) and only pressurizing their AAC (Fig. 6.1 (c,d)) .

6.2 Limitations and Future Work

Despite of the promising results obtained in this work, we recognize it presents a number of limitations. In the following sections we provide a list of the most important limitations and a brief discussion on how these can be addressed to extend the findings of this work.

6.2.1 Biocompatibility

Thanks to their inherent compliance, stretching capacity, ease of use, low cost, high availability and versatility that allows rapid prototyping by using traditional casting techniques, elastomers are widely used in the soft robotics community. Three of the most used elastomers in the fabrication of soft robots are Smooth-Sil 950, Sylgard 184 and Ecoflex 00-30 [31]. In this work, we used the latter to fabricate the chambers of all the developed actuators for the previously mentioned reasons. However, Ecoflex 00-30 is a platinum-catalyzed silicone rubber that is not biocompatible, which prevents its use in direct contact with organs and tissues. There are two approaches to overcome this limitation and extend the reach of this work outside of proof-of-concept:

1. **Encapsulation:** it has been shown that by encapsulating an implant built of non-biocompatible components in a biocompatible case, the device can operate safely inside a living body [43]. The soft robotic implants presented in this work might be encapsulated in, for example, a Silastic® skin, a biocompatible silicone. By implementing this approach, the forces exerted by the RAC against the wall of tubular organs would need to be re-assessed, because having an additional element between the emerging RAC balloon and the tissue might decrease the contact force and therefore, reduce the stimulation force provided by the RAC.

2. **Replacement:** another approach includes replacing Ecoflex 00-30 with a biocompatible material capable of providing soft implants with similar mechanical properties to the ones presented in this work. Popular examples include other types of silicone-based materials, such as Polydimethylsiloxane (PDMS), particularly Sylgard 184 [149], Silastic® skin and NuSil Med4-4220 (avantor®)[49]. However, these materials face the limitation of having greater (Young's) modulus values, higher shore hardness and lower elongation at break than Ecoflex 00-30. Other type of materials that could be used to provide the implants with biocompatibility are medical grade thermoplastics such as Tecoflex®[197]. However, this type of materials face the same mechanical limitations as the silicone-based alternatives. Double network biocompatible hydrogels are another alternative to replace Ecoflex 00-30 as the main structural material in soft

robotic implants. This type of hydrogels have demonstrated to have similar mechanical properties to silicone-based alternatives, with the advantage of reaching elongations of $\sim 851\%$ and a maximum tensile strength of 0.273 MPa [15].

Both approaches are feasible options to provide the soft robotic implants presented in this work with biocompatibility. However, if the chosen strategy to make the implants biocompatible is to replace the structural materials with silicone or thermoplastics options, design alterations need to be put in place to compensate for the increment in stiffness and reduced elongation, for example, increasing pressure rates and decreasing the thickness of the expandable membranes, however, this may make manufacturing more challenging. On the other hand, if hydrogels were to be used, a validation of the structural strength of the devices would be needed.

6.2.2 Scalability

By using geometrically simple building blocks that can be helically configured (SoPHIA and HA) or stacked (TA), the soft robotic implants described in this work can be adapted to a number of medical applications. The simplicity of the SPAs 3D shapes, cross-sectional geometries and their constraints/exoskeletons allow the designer to scale up or down the design easily. However, one of the limitations of this work is the lack of information regarding the impact on the performance of the implants if these were to be miniaturized. Although growth has been simulated in a clinically relevant scenario (Section 3.8.1.1) and demonstrated the tissue-elongation capabilities in an *ex vivo* test (Section 3.7.4) that can be used at centimeter scale, we cannot claim that the performance of the soft robotic implants for tissue regeneration via mechanostimulation will be satisfactory if these were reduced 60% their current size to fit inside a human esophagus (diameter $\sim$ 2cm [65]).

Fabricating the proposed soft implants at millimeter scale may become challenging using traditional manual casting techniques such as 3D molding. Because of this, we recommend to fabricate these scaled down versions using additive manufacturing techniques, capable of 3D printing at millimeter scale. This solution does not contradict the suggestions given in Section 6.2.1, since it is already possible to 3D print elastomers [192, 190]. Therefore, future work includes design miniaturization, fabrication and characterization of the extension, expansion and load-bearing capabilities of these scaled down versions of the soft robotic implants proposed in this thesis.

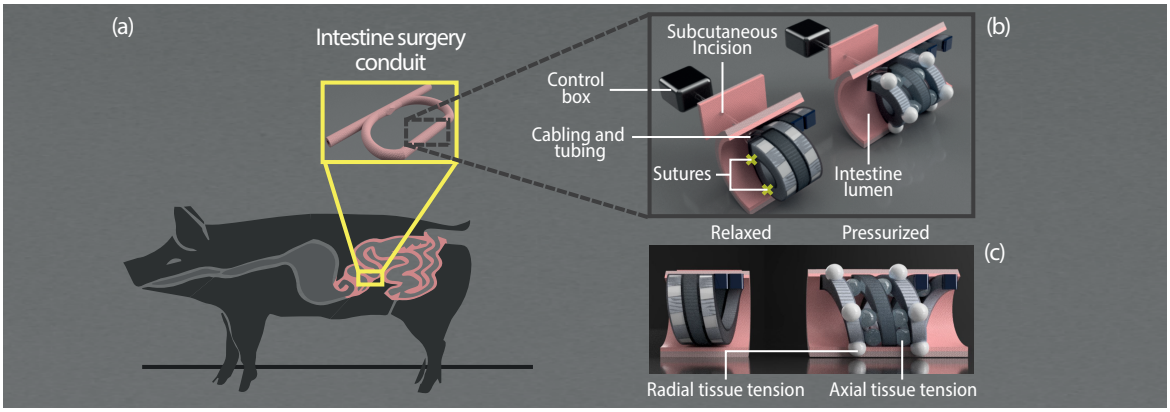

Fig. 6.2: Concept of a potential pre-clinical test protocol to use the SoPHIA inside of an American Yorkshire pig to evaluate its regenerative capabilities. (a) Detail of the intestine surgery conduit that the surgeons would perform to implant the SoPHIA. (b) Isometric and (c) side-view of the implanted relaxed and pressurized SoPHIA, components and tension types identification.

6.2.3 Implantation

The ease of configuration and modularity of the implants presented in this work could facilitate clinical intervention on different organs (Appendix A.3). In the case of the soft pneumatic strands used to built the SoPHIA, implantation potentially could be done by performing a small incision near the target organ, through which the AAC and RAC could be inserted, coiled, implanted and removed employing minimally invasive surgery procedures. An example of preliminary implantation of a soft pneumatic strand using this method is described in Appendix A.4.

The HA and TA have been designed so they could be introduced into the body via laparoscopic procedures to overcome the technical challenge of easing surgical protocol. In the case of esophagus regeneration due to long-gap esophageal atresia, the implants can be introduced trough the mouth and then mounted on the stub caused by an atresia. Then, the surgeon could fix the bottom and top ends of the device using over-the-scope clips [94] or a TachoSil® adhered to soft attachments (Appendix A.9). However, a systematic assessment of the impact of implantation to the host organ is needed, including analysis of its tissue histology. Finally, a pre-clinical study to quantify the levels of fibrotic response and muscle cells proliferation generated by the proposed implants is necessary to determine its real replacement and regenerative capabilities respectively. At the time of publication of this thesis, our group have started conversations with vets based on our achievements to validate the use of the SoPHIA *in vivo* using American Yorkshire pigs (Fig. 6.2).

6.2.4 Resilience

Additional to the clinical benefit of using soft matrices to build the robots presented in this work in decreasing fibrosis, it shows several technical advantages including their relatively easier manufacturing, high scalability, low pressure requirements and back-drivability that makes them ideal for human-robot interaction [134]. Moreover, their polymer base eases their sterilisation and the integration of mechatronic components in robotic implants [202]. One of the disadvantages of current soft systems made of elastomeric matrices is the trade-off offered by their soft bodies, which consist in providing safety in tissue interaction at the expense of performance reliability [128]. Additionally, recurring actuation leads to weakening and bulging of the soft matrices internal walls, driving to failure. We acknowledge that, although the robots presented in this work can provide real-time information about their extension, force and pressure conditions in bench-top tests, their use inside the body would be affected by the aforementioned disadvantage. Nevertheless, different approaches have been developed by the soft robotics community to overcome this challenge and make soft robots resilient, such as self-healing techniques [169] and advanced prioperceptive sensing strategies [79]. In our group, we are tackling this challenge following two different approaches: (1) Implementing fault detection at global controller level and actively using the shape-change robot capability to identify, disambiguate and compensate faults [14]; (2) by developing an in-situ sensing strategy that could complement and/or replace the already existing ex-situ pressure, distance and force sensors aiming to increase fault-tolerance and resilience [90].

6.3 Conclusion and Outlook

Effective tissue regeneration is a critical medical need that requires novel strategies to improve the body's endogenous capacity to restore organs' function [62]. The complexity of tissue repair processes and the intricate arrangement of layers in the GI tract have impaired distinct branches of regenerative medicine to effectively grow fully functional organs. However, it was demonstrated that by combining tissue growth principles from regenerative medicine, such as mechanostimulation, and control strategies from the robotics field into a implant it is possible to overcome that challenge. However, using traditional robotics approaches have shown to trigger fibrotic response, producing collagen formations in the treated area and avoiding the generation of vascular networks. In this thesis, we have implemented a soft-matter approach to match the stiffness of the implants to the tissue where it resides as a strategy to decrease or avoid fibrotic response. The obtained results confirm that soft robotic implants have the potential to treat short-tissue conditions while being safe, physiologically and metabolically effective and mechanically compatible, fulfilling the clinical and technical

Fig. 6.3: Soft robotics: the cornerstone that is blurring away the limitations of human-robot interaction. Scene from Big Hero 6, produced by ©Walt Disney Animation Studios, 2014.

aims posed at the beginning of this work. Although the designs introduced show limitations in resilience, implantation, scalability and biocompatibility different methods have been proposed to overcome or mitigate them which can be addressed as future work.

This thesis deepens the design of soft devices that aim to restore organs and tissue functions, providing relevant insights to both, the soft robotics and bionics fields. Since its initial appearances, soft robotics has been highly intertwined with the development of bionic devices, as in the 1950s, when Joseph L. McKibben developed a braided pneumatic actuator for an orthotic appliance for his daughter with polio [140]. This event gave birth to the McKibben Muscle, a lightweight, simple and safe actuator widely used even today.

But, why is soft robotics becoming such an important tool for bionics, as demonstrated by its exponential growth in academia and public media [16], since it was a field that until relatively recently has been dominated mainly by their hard counterparts? Conventional hard robots are usually marvelous at performing tasks *for humans*, such as carrying heavy weights or moving fast, replacing them entirely in performing those tasks. Instead, soft robots have demonstrated to be highly proficient in working in interaction *with humans*, extending their capabilities [206] (Fig. 6.3). Because of this, we envisage a future that is not necessarily entirely soft, but hybrid, in which we exploit the combination of speed, precision and force of hard robots with the safety, compliance and high-deformations of soft robots in the design of bionic technology. I believe that, because of the way soft robots and their soft-rigid versions interact with humans, acceptance of this technology will advance at a fast pace, causing to see soft-matter systems based on bionic solutions even as toys for children more frequently in a near future. From my point of view, this will depend on achieving the following objectives:

Standardization: From a technical point of view, there is a lack of precise and uniform terminology across bionic/soft systems-related publications that might be caused by the continuous advances in the field [190]. For example, what is compliance, what is softness? Although there are accepted definitions on how to define a soft robot one can still find himself in discussions about if this or that robot is soft or not, or if it is compliant or not. Clinically, the use of already accepted materials and techniques in the development of soft bionics can ease their acceptance into the medical setting, contributing to standardization.

Regulation and inclusion: While several hard robots have been approved to be used in the medical setting by regulation entities such as the U.S. Food and Drug Administration (FDA) and the European Medicines Agency (EMA) only a few soft-bionic devices have passed through this rigorous process. In order to achieve this, research and development of such systems should involve different stakeholders in the design process that provide human-centered insights, including patients and clinicians, which is not done enough currently. As a result, the resistance to adopt these new technologies might decrease, positively changing the perception of people about having soft robots inside their body to treat them.

Expansion: Bionic systems based on soft or semi-soft approaches have been highly dominated by the design and fabrication of grippers, such as human-like hands and fingers. I think this driven by the achievement of providing a "gentle" touch with a robot. It is only recently that soft roboticists started looking at cardiac diseases and minimally invasive tools while grippers continued to emerge. By expanding the range of applications (e.g. parts of the body or clinical conditions) and coming up with creative ways to use soft bionic systems (not only for health purposes but for leisure and human enhancement) we will boost their acceptance in the society.

Interdisciplinary convergence: Individual efforts from different branches of regenerative medicine and robotics have definitely shown progress in growing tissue as discussed in Chapter 2. However, as discussed in this work, it is the interdisciplinary effort that has the higher potential to achieve innovation. By formally merging regenerative medicine and robotics, as well as their sub-disciplines, into a unified tissue therapy strategy, future developments can easily succeed where multidisciplinary approaches have failed.

Current stereotypes that society has about bionics are changing rapidly as we get closer to fulfilling the aforementioned objectives. The future envisages a closer coexistence between

soft-bionic systems and humans that will definitely happen inside us and I am confident that this will one day be the standard in healthcare, as it is now to use a cast on a fractured bone.

Appendix A

Supplementary Information from Chapter 3

A.1 RAC Design Optimization

In this section of the appendix we describe the experiment we conducted to determine the most efficient RAC constraint configuration to be used in the SoPHIA's design (Fig. 3.2 (a)). Efficiency was measured in terms of homogeneity of expansion across balloons and the relation between pressure and expansion in the unconstrained sections. Three different samples were fabricated (Fig. A.1 (a)), following the procedure described in Fig. A.3 (d-g) and Fig. A.4. Their cross-sectional dimensions are given in Fig. 3.2 (a). Each configuration had a different size correlation between the the fabric-constrained (CS) and unconstrained sections (US). The size ratio of each configuration in the samples was as follows: (1) 10 mm of US and 10 mm of CS; (2) 10 mm of US and 5 mm of CS; (3) 5 mm of US and 10 mm of CS. A DC pneumatic pump was used to pressurize the samples to 14, 16 and 18 kPa while a pressure sensor measured the changes of pressure inside the chambers. Data was acquired via a NI-DAQ and processed using LabVIEW. This system is presented in more detail in Section 3.6.1. The experiments were recorded and repeated three times per sample. Then, we measured the size of the expanded sections using ImageJ software (NIH). Finally, the average size and standard deviation of the expanded US sections were obtained from each sample at the mentioned target pressures. Sample number one, which had identical US and CS dimensions, yielded the greatest and most uniform expansion in relation to the pressure Fig. A.1(b). Because of this, it was selected to conform the design of the RACs constraints.

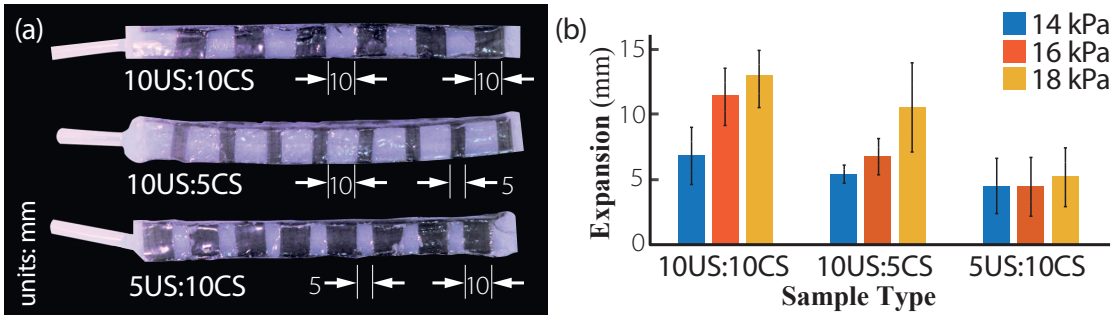

Fig. A.1: Design of the RAC constraints. (a) Experimental samples used to determine the most efficient configuration in relation to expansion and uniformity. (b) Performance of the three samples. The sample 10US:10CS shows the most efficient configuration, as it achieves the most homogeneous expansion across its balloons as demonstrated by shorter error bars and the higher expansion across the three types of samples.

A.1.1 Finite Element Modelling of the RAC

To validate our physical experiments we numerically modeled the mechanical behaviour of the hydro-static deformation of the unconstrained sections in the three samples. We developed the 3D models and analysis of the samples on Abaqus/CAE (Simulia, Dassault Systemes^{TM}) using hybrid 8-node solid element (C3D8RH). To capture the hyperelastic behavior of silicone, we used a 3-term Ogden model, which parameters are described in Section 4.4.3. Following the conditions used in the physical experiments, the numerical analysis was conducted on three different models: (1) 10 mm of US and 10 mm of CS; (2) 10 mm of US and 5 mm of CS; (3) 5 mm of US and 10 mm of CS (Fig. A.2). The pressure load was 14 kPa, 16 kPa, 18 kPa. It can be seen that the sample 10US:10CS shows to be the most efficient configuration by yielding the greatest and more homogeneous expansion in co-relation with pressure (Fig. A.2(b)). This verification validates our design for the RAC constraints.

A.2 SoPHIA's Detailed Fabrication Procedure

The pneumatic chambers that constitute the building blocks of SoPHIA are fabricated by a combination of 3D molding techniques, inextensible layers principle (Section 2.6.2) and manual configuration and assembly.

A.2.1 3D Molding

First, we developed 3D printed molds, designed in AutoCAD (Autodesk^{TM}) and fabricated out of ABS material (Stratasys Mojo^{TM}) (Fig. A.3(a-d)). This molds were used to cast the

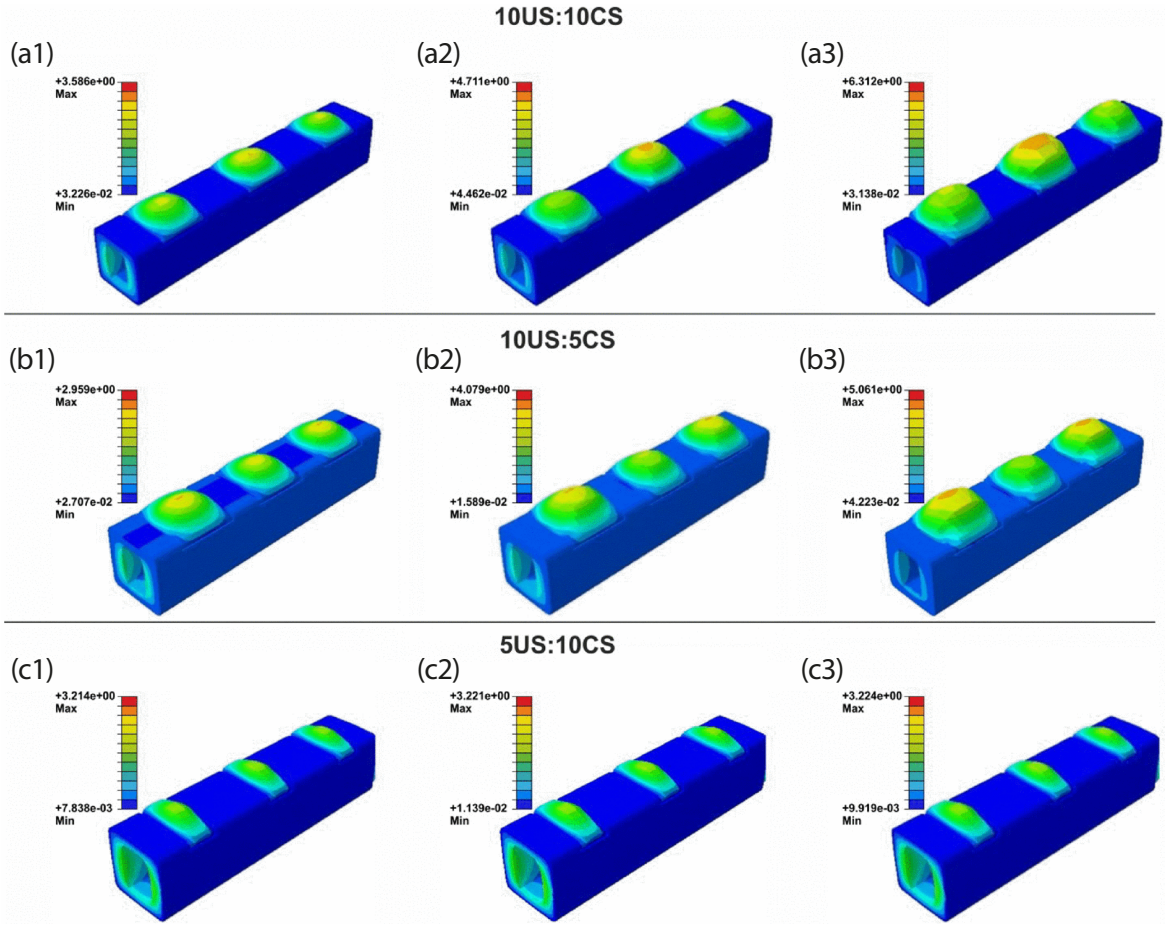

Fig. A.2: Finite Element Analysis of the three elastomeric samples under 14kPa, 16kPa and 18kPa of pressure. (a1), (a2) and (a3) show the pressure response of the sample with ratio of 10US:10CS. The maximum expansion of the balloon was 39.8%, 52.3% and 70.1% respectively; (b1), (b2) and (b3) show the pressure response of the sample with ratio of 10US:5CS. The maximum displacement of the balloon was 32.9%, 45.3%, 56.2% respectively; (c1), (c2) and (c3) show the pressure response of the sample with ratio of 5US:10CS. The maximum displacement of the balloon was 35.7%, 35.8%, 35.8% respectively. Percentages with regard to the size height of the chambers (9mm).

RAC and AAC out of Ecoflex 00-30 (Smooth On Inc.) silicone. To do this, first we sprayed inside the molds with release agent and left it curing for 5 minutes. Meanwhile, we mixed and defoamed part A and B of the silicone using a centrifugal mixer (ARE-250 Mixer, Thinky^{TM}). While the silicone was being mixed, we assembled the molds and visually ensured the spray has cured. Then, we degassed the mixed silicone in a desiccator for 3 minutes and poured the silicone into the molds. Next, we left the molds to cure at room temperature for three hours and then we thermally post-cured them at 80°c for two hours and then at 100°c for one hour. Finally, the cured silicone chambers were disengaged from the molds (Fig. A.3(d)). To shape SoPHIA, four modules were assembled together using uncured silicone to achieve a final length of each chamber of 48 cm. This length can be varied by assembling more units into one pneumatic chamber, increasing the amount of coils and height of the SoPHIA (Fig. A.5).

A.2.2 Embedding Fabric Constraints

The constraints were designed in AutoCAD (Autodesk^{TM}) and fabricated out of laser-cut polyester fabric (SoftCrepe-59 Polyester fabric, Minerva Crafts^{TM}) (Fig. A.3(e-f)). The cutout patterns make a "mesh effect" in the fabric, easing the embedding into the silicone chamber. To embed the constraints in the actuation chambers, we painted with uncured silicone the walls were the polyester will be placed as seen in Fig. A.3(h). Then, we carefully placed the fabric on the silicone chamber face by face (Fig. A.3(g)) and heated the area to accelerate embedding into the chamber using a heat gun, avoiding misalignment of the fabric.

A.2.3 Sealing and Tubing

Following an identical process as for the fabrication of the silicone chambers, we casted the caps that will seal them. These caps also constitute the interface by which the tubing is inserted into the chambers to pressurize them. Fig. A.4(a-c) shows the dimensions of the molds, a diagram of casting of the caps and a resulting cap that will seal the chambers. To shape the air inlet and pressurize the chambers, we pierced the center of the silicone cap with a tweezer to create an inlet for a platinum-cured silicone tube (Masterflex Transfer Tubing, Cole-Parmer) (Fig. A.3(d)). The tube was introduced until it passes through the entire cap's thickness and then we applied Silpoxy^{TM} to the cross-sectional area of the chamber to fix the tube to the cap. Finally, we attached the cap to the chamber and waited 12 minutes for the Silpoxy^{TM} to cure.

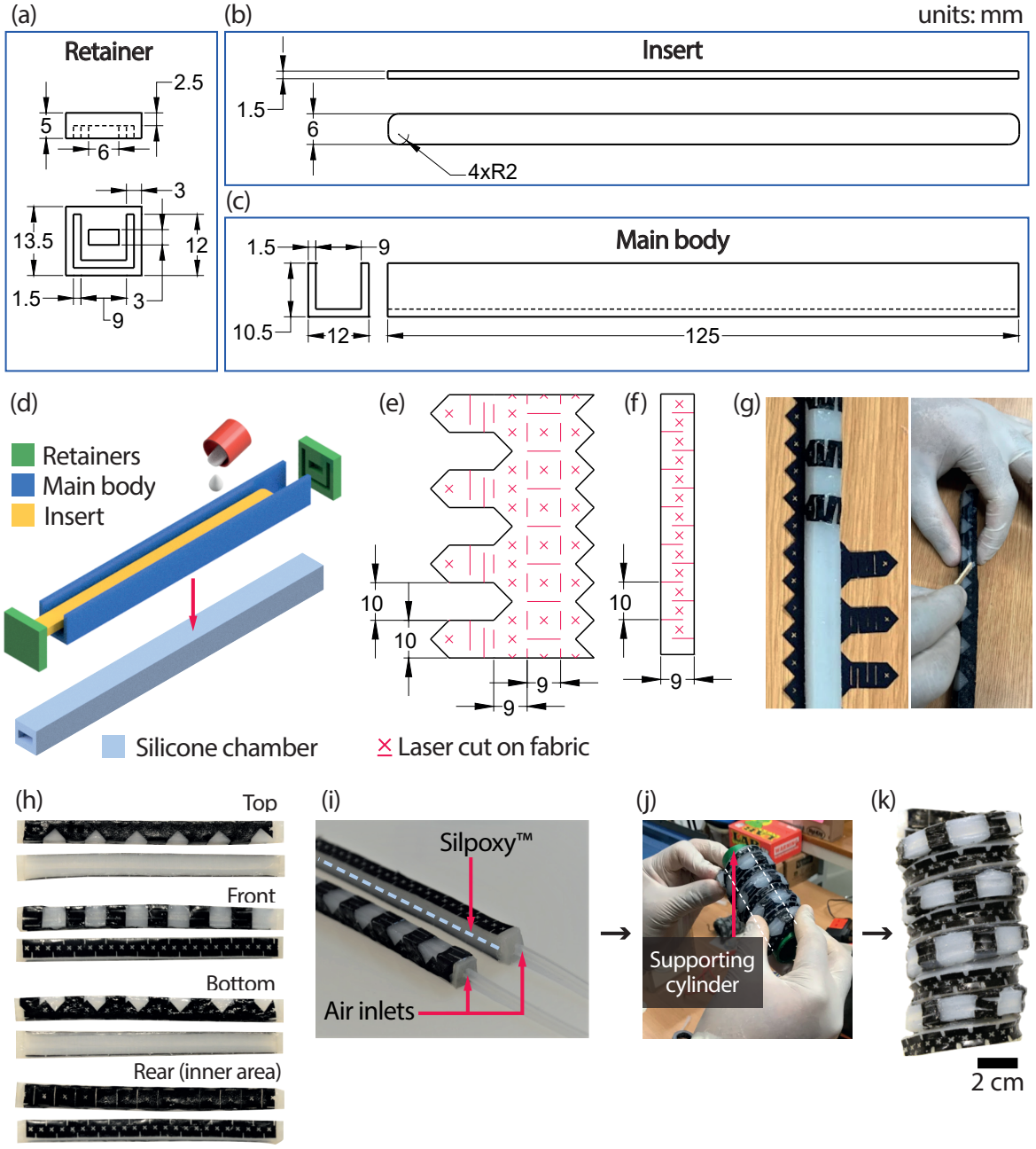

Fig. A.3: SoPHIA's fabrication procedure. (a) Dimensions of mold components: retainer, (b) insert and (c) main body. (d) Explosive view of the mold components and isometric view of the resulting silicone chamber. (e) Section of the constraints design for the RAC and (f) AAC. (g) Embedding of the constraints into the silicone chamber. (h) Different views of the RAC and AAC sections after embedding the polyester constraints with respect to their final configuration in SoPHIA. (i) Isometric detail of the RAC and AAC showing where the Silpoxy™ is applied to bond both chambers and where the air inlets are placed. Given that SoPHIA relies on only two chambers that shape the whole actuator's body, only two air inlets are needed, one per chamber. (j) The constrained soft pneumatic strands after being coiled around a cylindrical support and being held for 12 minutes until the Silpoxy™ cures. Then, we removed the cylinder. (k) The resulting SoPHIA.

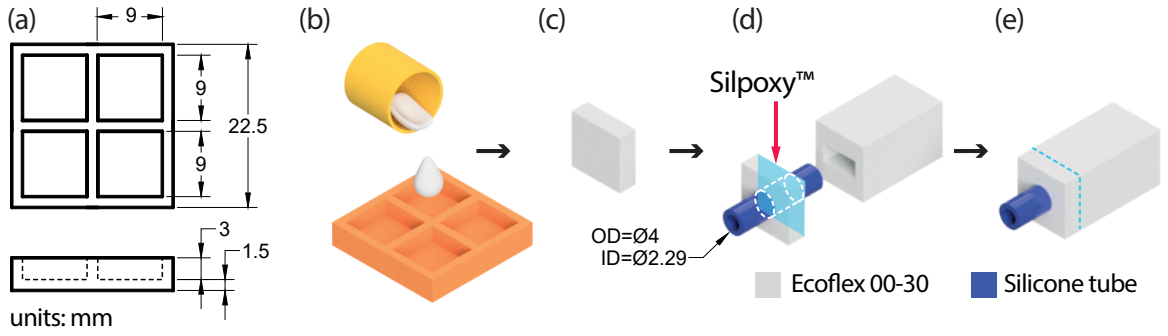

Fig. A.4: Sealing of the silicone chambers. (a) Dimensions of the mold to fabricate the caps. (b) Mold and (c) the resulting cap. (d) Diagram showing how the air inlet is assembled. (e) A sealed silicone chamber.

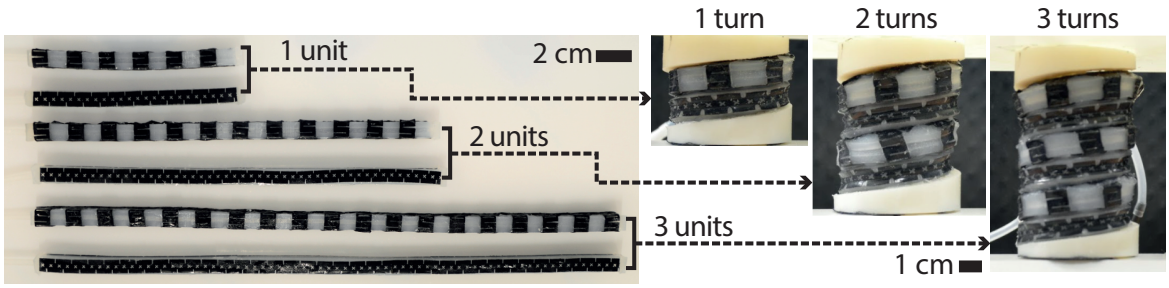

Fig. A.5: Modularity in SoPHIA. The height and amount of coils depend on the length of the two initial chambers that shape the helix.

A.2.4 Coiling The Pneumatic Strands

We bonded the two chambers by adding a thin line of Silpoxy^{TM} at the center of the top face of the AAC (Fig. A.3(i)) and placed the RAC on top of it. We left the Silpoxy^{TM} to cure for 12 minutes and then proceeded to configure the chambers into a helix. We added a thin line of Silpoxy^{TM} at the center of the bottom face of the AAC this time and coiled the chambers around a 3D printed cylinder that works as a supporting structure (Fig. A.3(j)). This cylinder creates the inner tubular space in the actuator, that remains constant across all sections in this work with a diameter of 30 mm. After the Silpoxy^{TM} cured in between chambers, We removed the cylinder without damaging the SoPHIA (Fig. A.3(k)).

A.3 Configurable Soft Tool for Mechanotherapy Based Tissue Repair

In this appendix, we test the SoPHIA's RAC configuration capabilities to be used as a stand-alone tool for mechanotherapy based tissue repair. This tool has the potential to be configured

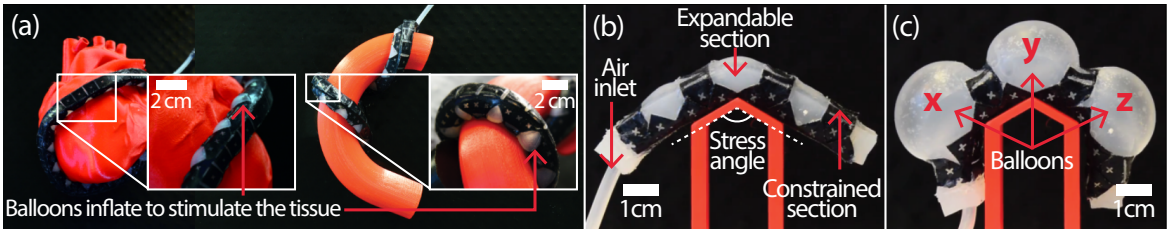

Fig. A.6: The SoPHIA's RAC used as a configurable soft tool for mechanotherapy based tissue repair based. (a) Examples of how the RAC can be configured around different organs. (b) Experimental rig and the RAC in a relaxed state. (c) The RAC expanded at 18 kPa of pressure under a stress angle of 15°.

to different organs' anatomies to apply mechanical stimulation via tissue tension to repair and regenerate tissue [40]. Broader applications include muscle repair and regeneration using mechanotherapy that can be applied to various organs such as intestine growth for short bowel syndrome (SBS), esophageal growth for long-gap esophageal atresia (LGOA) or aorta growth for mid aortic syndrome treatments and heart conditioning (Fig. A.6(a)).

We aimed to identify the expansion response of the RAC to different angular configurations to test its configuration capabilities to be used as a stand-alone tool for mechanotherapy based tissue repair. To do this we fixed the RAC section using cyanoacrylate to 3D printed supports under various angles of bending from 15° to 120° (Fig. A.6(b,c)). Then, we pressurized the RAC at 18 kPa.

The results showed that balloons X,Y and Z (Fig. A.7) are affected differently by the stress angles. X (the balloon closer to the air inlet and placed before the angle) showed the maximum expansion among all stress angles and trials, while balloon Y expanded more than balloon Z until reaching 90° of stress angle, where their expansion became similar. This implies that the change in volume of the chamber caused by the stress angle decreases the airflow that pressurises different sections of the RAC. The error bars in Fig. A.7, represent the standard deviation across five trials.

The RAC is a potentially versatile clinical tool for tissue stimulation that could be configured into different geometries. Although the body does not have sharp angles, we evaluated the RAC under extreme scenarios. Intricate shapes may require the RAC to adopt different bending angles and radii, causing the balloons to expand at different sizes. However, we demonstrated that the RAC can be configured around different anatomical geometries without stopping its function.

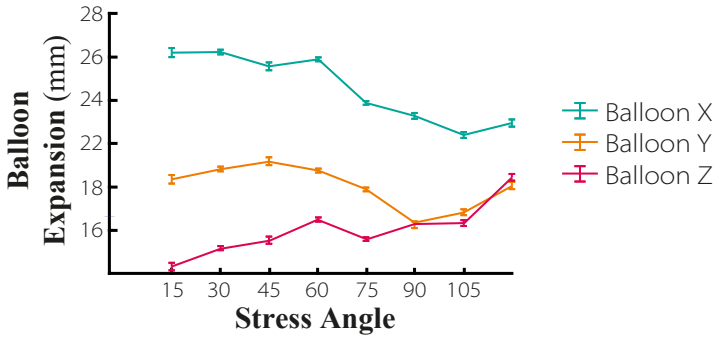

Fig. A.7: Expansion of the balloons X, Y and Z under different stress angles. Acute angles show more heterogeneity among the balloons expansion, while obtuse angles show more uniform expansion. However, the RAC remains functional under all stress angles.

A.4 SoPHIA's Module Preliminary Implantation Test

In this appendix we describe a preliminary test using one of the SoPHIA's unconstrained building blocks or Soft Pneumatic Strand (SPS) to obtain insights into their implantation as a regenerative tool on tis own. We performed this test using a New Zealand White rabbit carcass. The short intestine of the specimen was exposed and then, we sutured one of the SPS extremes to the organ using a piece of polyester fabric attached to the elastomer using uncured silicone. Then, we coiled the strand around the intestine until we wrapped it with the entire SPS' length. Finally, we proceeded to pressurize the SPS to observe the effects and assess them qualitatively.

Fixation of the SPS to the intestine using a piece of polyester fabric as interface was effective (Fig. A.8 (a)), as it provides enough surface area for the surgeon to perform suturing that can withstand the manipulation during coiling. Coiling of the SPS around the organ while keeping its shape was challenging (Fig. A.8 (b)), as the intestine tends to start twisting. We

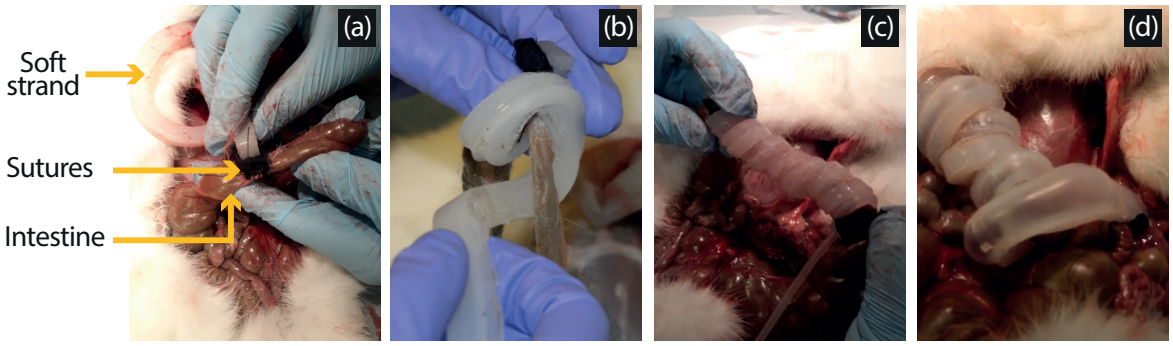

Fig. A.8: Preliminary tests of mounting and pressurizing a soft pneumatic strand (SPS) on a rabbit carcass. (a) Suturing of one extreme of the SPS to the rabbit's intestine. (b) Coiling of the SPS (c) until wrapping the intestine section with the entire strand body. (d) The SPS in place and pressurized.

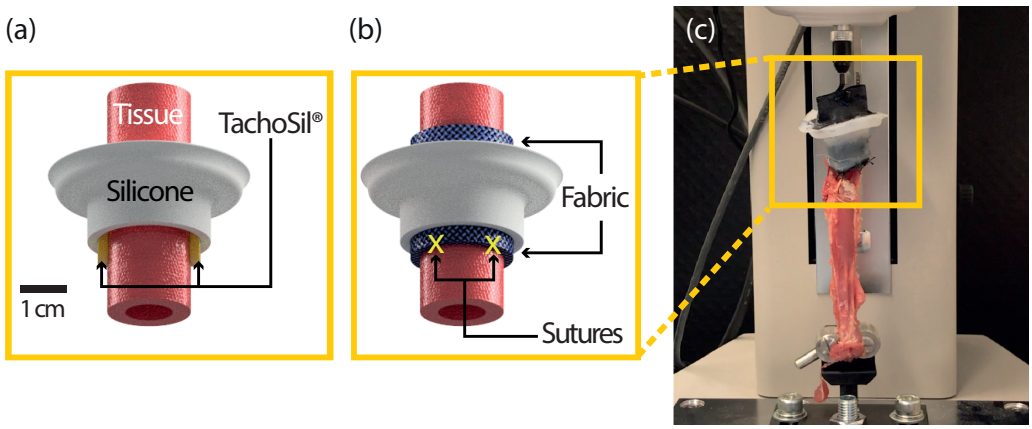

Fig. A.9: The tissue attachments for soft implantable devices. (a) Attachment tissue-implant using TachoSil® membrane and (b) sutures. (c) The experimental setup.

observed as well that the squared profile of the SPS is prone to be affected by lateral-torsional buckling instabilities, causing it to deform as it is coiled (Fig. A.8 (c)). Adding fabric reinforcements to maintain shape, as in the constrained version of the SPS (Fig. 3.2) or using a circular cross-sectional geometry for the strand, as in the toroidal actuator in Chapter 5 might help reducing this effect. Additionally, we observed that, because the intestine was full of food, it was challenging to manipulate. We envisage that implantation of this type of technology should be performed after the patient undertake fasting. Finally, because coiling is challenging to be done uniformly, the SPS undergoes stiffness differently throughout its body, causing it to expand heterogeneously (Fig. A.8 (d)). We envisage that the use of fabric reinforcements or selecting specific cross-sectional geometries for the strand might reduce heterogeneity. Heterogeneity problems in soft pneumatic actuators is further discussed in Chapter 4.

A.5 A Preliminary Evaluation of Fully Soft Tissue Attachment Interfaces for Soft Implantable Devices

In this section, we extend our previous work investigating a suitable interface between soft implants and biological tissues by presenting a preliminary comparative study of tissue attachment interfaces for soft robotic implants such as SoPHIA (Section 3.6.5). These interfaces are based on two methods: (1) attachment using a fibrinogen matrix (FM) (Fig. A.9(a)) and (2) suturing with surgical needle and wire using a fabric interface (Fig. A.9(b)). The two candidate solutions are evaluated based on their rupture resistance measured by a tensile testing machine (Fig. A.9(c)).

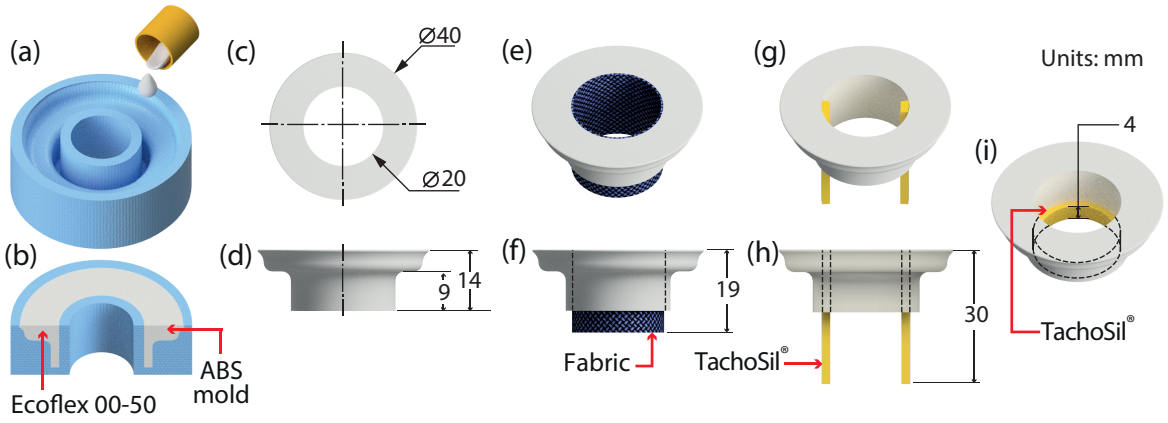

Fig. A.10: Fabrication process for the soft attachments. (a) Mold for casting of the soft attachments. (b) Cross-sectional view of the soft attachment inside the mold. (c) General top and (d) side dimensions of the soft attachments. (e) The attachment method using sutures. (f) General dimensions of the attachment with the embedded fabric for suturing. (g) Method using an FM: (h) General dimensions of the attachment with the glued TachoSil® strips used for rabbit and (i) pig tissue.

A.5.1 Soft Tissue Attachments Fabrication

Molds were fabricated via rapid prototyping out of ABS material (Prusa© 3D printer) to cast the soft attachments. We mixed and degassed (Thinky Mixer ARE-250) silicone rubber (Ecoflex 00-50, Smooth-On Inc.) that we then poured into the ABS molds (Fig. A.10(a)). The silicone parts were left to cure at room temperature for three hours, followed by a post-curing process of two hours at 80° and then one hour at 100° using an oven (SciQuip©). For the attachment method using an FM, two strips of TachoSil® were glued to the silicone rubber using cyanoacrylate adhesive (Fig. A.10(h,i)). For the method using sutures, we embedded polyester fabric into the silicone attachment using uncured Ecoflex 00-50 (Fig. A.10(e,f)). It was then left to cure at room temperature for three hours.

A.5.2 Attachment to tissue procedure

To attach the FM to the tissue, we pressed the two together for 3 minutes to bond them, around the circumference of the porcine esophagus (Fig. A.10(i)) and longitudinally along the rabbit esophagi (Fig. A.10(h)). One sample of porcine tissue and three samples of New Zealand white rabbit tissue were used in this preliminary study. These numbers were limited by the tissue that was available. Each tissue sample was first tested with the FM and then with the sutures. To attach the polyester fabric to the tissue, we used four simple interrupted sutures made with black braided non-absorbable suture silk and a X-1 CONV 22 mm needle (MERSILK® kit). This suturing technique is commonly used in surgery to close wounds. Fig. A.9(a,b) show a schematic of the TAs with FM and suture attachments respectively.

The extra layer of fabric was added for the suturing method as we found that when directly suturing the silicone rubber, the wires were tearing the silicone, even for small applied shear forces. This was first explored in Appendix A.4.

A.5.3 Tensile Experiment Procedure

We used the EMX-5N IMADA tensile test machine to measure the force exerted on the tissue and TA along with the displacement. The porcine and rabbit esophagi bonded to the TAs were placed on the tensile test machine. The soft cap was used in replacement of the soft robot and was hooked to the top of the tensile testing machine, the *ex vivo* tissues were clamped to the lower part of the machine (Fig. A.9(c). The tissue was then stretched at a speed of 50mm/min until either the failure of the attachment or the force sensor limit (5N) was reached. During the trial, the displacement of the tensile test machine and the traction force were acquired at 1kHz. *Ex vivo* experimentation was considered the only suitable type of experimentation where rupture force can be investigated with animal tissue. This is due to the ethical implications of rupturing tissue *in vivo*, which would cause significant harm to the animal.

A.5.4 Results

(Fig. A.11(a)) shows the increasing force as the tissue was stretched before failure for both interfaces for one trial of each tissue. It should be noted that, in this figure, the force signals have been filtered (with a moving average filter) and down-sampled to reduce the measurement noise. In Fig. A.11(c), the rupture forces for the three trials on the rabbit esophagi and the single trial on the porcine esophagus, conducted for the two different attachment methods, are shown. The rupture force was defined as the maximum force achieved before the attachment failed. The FM withstood a maximum of 3N and 4N for the rabbit and porcine trials respectively. In each trial the FM interface failed, leaving the mesh adhered to the attachment. For the sutures method, a force greater than 4N was withstood in all of the trials, with the suturing method reaching the 5N limit of the load cell for the porcine trial. For the trial where the 5N limit was not reached, the tissue ripped before the sutures failed.

Additionally to the maximum forces achieved, some sudden drops of force can be observed during the tests. To highlight these drops, the force gradient $\frac{\partial F}{\partial x}$ has been computed and shown in Fig. A.11(b). This gradient can be seen as the equivalent stiffness of the TA in series with the tissue sample. It can be seen that this stiffness tends to increase slowly with the elongation, but reaches some local plateaus before the gradient finally drops at the

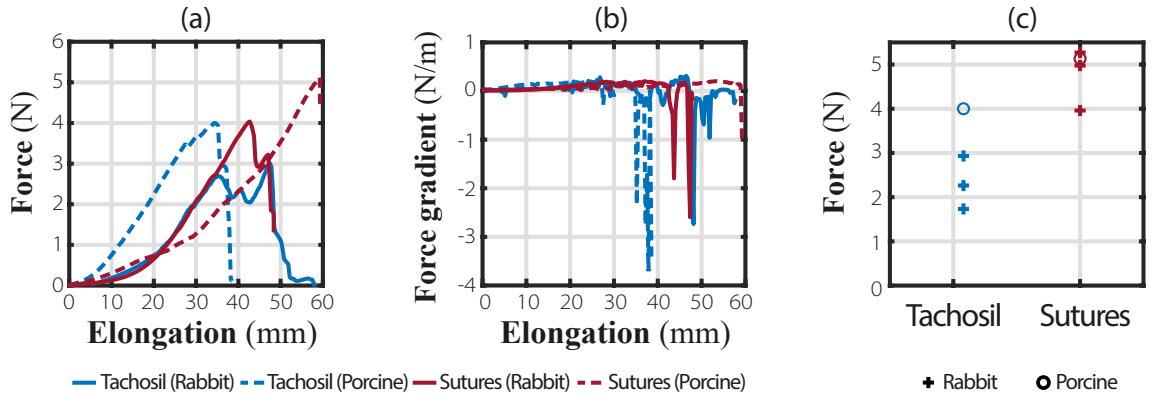

Fig. A.11: Forces measured during elongation and at rupture. (a) Force response to the elongation of the tissue for both attachment methods and for a single trial of both the rabbit and porcine esophagi. (b) Gradient of force during elongation of the tissue. The negative peaks represent local force drops indicative of rupture. (c) Rupture force, maximum force applied before attachment failed, of the attachments for both rabbit and porcine esophagi.

rupture. The local force drops are also highlighted in Fig. A.11(b) by the negative peaks in the gradient.

A.5.5 Discussion

In a previous study by our group [43], we have shown that a 2.5N force was enough to grow tissue by mechanotherapy with a robotic implant. The current study demonstrates not only that the classic suturing approach easily withstands this force, but also that with the TachoSil®, the rupture force of the attachment was on average 2.4N for the rabbit esophagi and 2.8N for the porcine esophagus. These results suggest that an FM could be used to replace traditional suturing methods to attach soft robots to tissue. The difference in the rupture force between the rabbit and the porcine tissue can be explained by the difference in the size of the tissues or the placement of the FM. Indeed, the porcine tissue has a larger diameter which allows for a more uniform contact between the FM and the tissue.

The tissue morphology also influenced the direction in which the FM was attached and differed for the two types of tissue samples, as shown in Fig. A.10(h,i). Although the area of FM used to attach the TA to the tissue was consistent throughout all the experiments, the attachment technique varied. This could have affected the rupture force, as although the forces are being exerted in the same direction, the attachments for the rabbit (Fig. A.10(g,h)) are likely to induce more localized stresses. Furthermore, the FM was secured to the tissue over a larger area than the sutures. The sutures were attached at multiple localized points. It can be hypothesized that the sutures generate greater localized forces in the tissue. These forces are also dependent on the tightness of the suture which is difficult to control as it

is dependant on the surgical practice [213]. These variable localized forces can alter the surrounding cell morphology or damage the tissue [193]. The observation of the samples after failure shows that the rupture with the FM attachment occurred when the latter was peeled off the esophageal tissue. Moreover, this happened without apparent damage at the tissue level. On the other hand, for the suture attachment, excessive forces applied may result in the attachment not failing, but tearing damage on the tissue nearby the suture.

In Fig. A.11(b), we can see a slight upwards trend of all samples in the force gradient, regarded as the equivalent stiffness. This trend is due to the non-linear elasticity of tissue. The purpose of the attachment is not to induce cellular response, but to secure the implant *in vivo*. A stiffness that is more homogeneous and compliant to the tissue is therefore less likely to cause adverse effects, such as fibrosis. In this study, there is no clear difference in overall stiffness between the FM and the sutures. The sudden drops seen in Fig. A.11(b) could be explained by two phenomena. Firstly, this may be the result of a partial rupture of the attachments. The second is a possible tearing or plastic deformation of the tissue. However, in real case applications, these scenarios should be detected and avoided. There were some limitations in the materials and methods used that should be addressed in future works. Firstly, due to limited tissue availability, the method was only tried on three rabbit esophagi and one porcine, so future work would include more trials on tissue. With regards to the tissue, each sample was first tested with an FM and then with sutures, given the limited availability. The FM detached from the tissue before any damage to the tissue was visible, but any plastic deformation induced by the initial tensile testing with the FM, may have impacted the results of the latter tests with sutures. Some materials used in this study (cyanoacrylate adhesive, polyester fabric and Ecoflex 00-50) are not graded as biocompatible. Non-biocompatible materials are generally cheaper than their biocompatible alternatives and share similar physical properties. They can therefore be substituted for future experimentation. Finally, the study outlined in this appendix was entirely *ex vivo* and was not conducted under sterile conditions. For future *ex vivo* and *in vivo* experimentation, the tissue attachments can be fabricated under sterile conditions in a biosafety cabinet, to improve the condition of the biological samples.

Appendix B

Supplementary Information from Chapter 5

B.1 Effect of the exoskeleton's unconstrained areas geometry on expansion and stress in the membrane

To maximize the expansion rates of the membranes that consequently benefits the overall motion of the M2H-HBMAs, we developed a numerical model that analyzes the effect of the exoskeleton's unconstrained area geometry on expansion and stress in the membrane. These are the exposed areas where the membrane will expand out of the exoskeleton (Fig. B.1(a-b)). Given that the interaction between the exoskeleton and the silicone balloon impacts on the behaviour of the latter, this is a relevant design parameter to consider. For example, higher stress concentrations in the exoskeleton-membrane interface might lead to bursting of the balloon. In this analysis, we considered circular (Fig. B.1(a,i)(b,i)) and squared geometries (Fig. B.1(a,ii)(b,ii)) because they are the most basic shapes for the unconstrained areas. Also, circular and squared openings were selected because they produce the least amount of stress in the elastomeric matrix and for consistency with our previous works respectively. For the shape of the chamber of the fluidic actuator contained in the exoskeleton, we also selected circular and squared geometries, two of the most common shapes for fluidic actuators. The used dimensions (Fig. B.1(e-f)) are set for a prototype that at this point would fit to be mounted externally to human tubular organs, though scaling down is envisaged as a subsequent phase of development. Fig. B.1(c,d) shows the boundary and load conditions, as well as Δ, used to measure performance efficiency with the following equation:

$$i = \frac{\Delta}{\sigma} \tag{B.1}$$

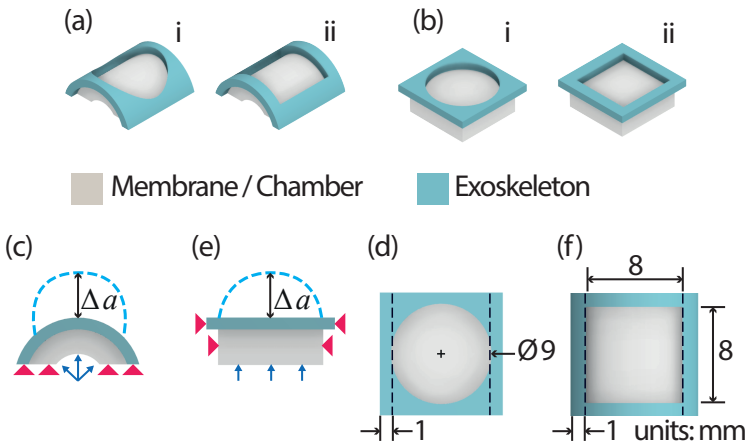

Fig. B.1: Setup for the numerical analysis of the unconstrained area's geometry in the exoskeleton to assess the membrane expansion and stress concentrations. The simplified geometries tested in this analysis for the (a) circular and (b) squared chambers. For both shapes, the inserts i and ii show circular and squared unconstrained areas respectively. Identification of the load, boundary conditions and measured displacement (Δ) used in this analysis for the (c) circular and (d) squared chambers. General dimensions of the tested geometries for the (e) circular and (f) squared chambers.

where Δ is the maximum expansion of the ballooning membrane when pressurized and σ is the highest stress concentration value in the interface between the ballooning membrane and the constraining surface. The most efficient combination of chamber and constraint geometry will allow the silicone to expand higher with lower amount of stress, potentially increasing the actuator's fatigue life. The technical implication is that the more the membrane expands without bursting, the higher the axial extension and radial expansion of the actuator. An inefficient configuration is represented by either, high expansion rates with high stress concentrations, low expansion rates with low stress, or low expansion with high stress concentrations. The settings for the simulation are described in Section B.3. The material modeled for the constraining surface is a 3D printed polymer, further described in Section 5.3.2.

As can be seen in Fig. B.2(a), both exoskeleton's unconstrained sections geometries in the simplification of the squared chamber, showed to achieve the highest expansion among all the designs when they are pressurized. However, also both of the unconstrained sections in the simplification of the circular chambers, showed the lowest stress concentrations around the interface between the exoskeleton and the ballooning membrane (Fig. B.2(b)) under the same pressure conditions. By using Eq. B.1, we identified the design with higher efficiency in terms of expansion and stress. Fig. B.2(c) shows that the circular unconstrained geometries are the best trade-off between expansion and stress concentrations for both M2H-HBMAs. This means that the design of both actuators should include circular unconstrained areas for the

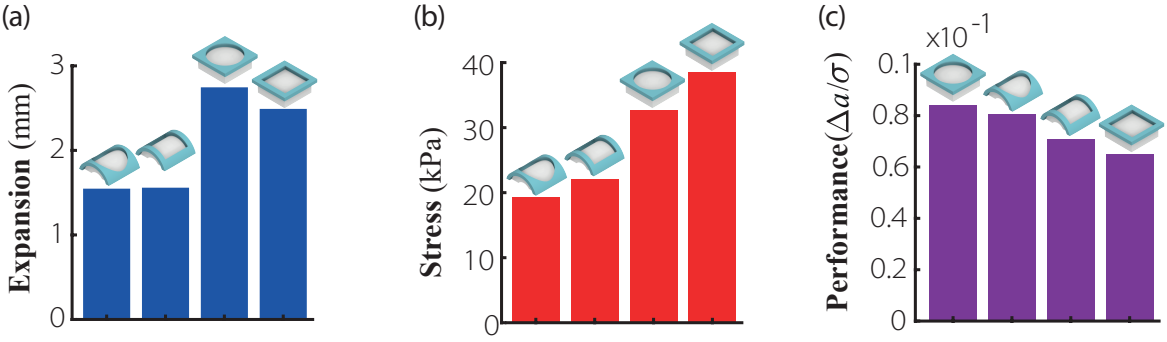

Fig. B.2: Effect of the exoskeleton's unconstrained areas geometry on (a) expansion (Δ) and (b) stress (σ) of ballooning membranes when pressurized at 32 kPa. (c) Performance index of the expandable ballooning membrane, showing that circular unconstrained areas yield higher expansion rates at lower stresses in comparison to the squared unconstrained areas.

membrane to expand instead of squared to reduce the risk of tearing without compromising expansion rates.

B.2 Contact Analysis

Expansion of the membranes enables the motion of the M2H-HBMAs and their envisaged configuration is a set of stacked modules. Due to this, it is relevant to describe the interaction between the ballooning membrane and the surfaces they are pushing to achieve axial extension or to provide stimulation through radial expansion. We developed a numerical model to determine the most efficient interface between the ballooning membrane and the exoskeleton of the stacked chambers in function of their contact pressure and exerted force.

For this analysis, we used two types of interface shapes: a convex shape (Fig. B.3(a)) and a flat shape (Fig. B.3(b)). We modeled a simplified version of the membrane and exoskeleton and placed them below the convex and flat shapes with three variations for each of them: 1 ((Fig. B.3(c,f)), 2 (Fig. B.3(d,g)) and 3 mm ((Fig. B.3(e,h)) of separation between the relaxed membrane and the contact surface. These incremental levels of separation allow us to define the evolution in contact pressure and force in stages. The settings for the simulation are described in Section B.3. The material properties for the constraining shapes are described in Section 5.3.2. The boundary conditions and load identification are shown in Fig. B.3.

The convex shape (Fig. B.4(a-c)) produces up to $\sim$ 30 kPa of contact pressure, while the flat shape produces only $\sim$ 17 kPa (Fig. B.4(d-f)), almost 50% lower contact pressures. Although these results do not necessarily imply that the convex shapes are $\sim$ 50% more prone to failure than the flat shapes as a result of contact interaction, lower stresses in the silicone membrane should contribute to increase longevity of the system. Despite exerting

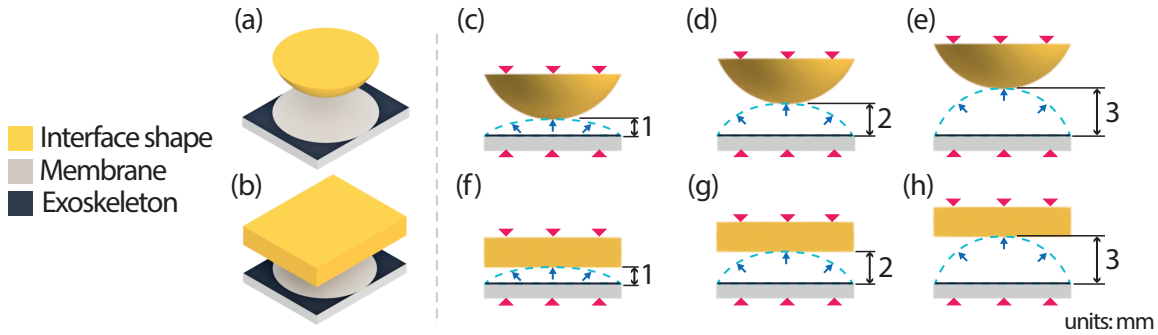

Fig. B.3: Numerical modeling setup for the contact analysis of a pressurized membrane. Isometric view of the geometries and components used in the analysis for the (a) convex and (b) flat interfaces. Diagrams showing the location of the boundary conditions and forces for 3 scenarios, varying the distance from 1 to 3 mm between a silicone membrane and (c-e) convex and (f-h) flat interfaces.

higher contact pressures, the ballooning membrane exerts higher forces, of up to 30% against the flat shape than the convex one (Fig. B.4 g). This is relevant for the design of the two M2H-HBMAs, as their axial extension relies on ballooning membranes that push upwards downwards the stacked levels above and bellow the Axial Actuation Chambers (AACs). Additionally, Fig. B.4(a-c, ii) shows a higher deformation of the membrane for the convex interface than for the flat interface Fig. B.4(d-f, ii). These results motivated the inclusion of the flat surface on top and bottom of the TA's RAC (Fig. 5.4(d)). In this way, the AAC's ballooning membranes will be pushing the stacked RACs using a flat interface.

B.3 Intraluminal Deformation

Given that the M2H-HBMAs could be implanted intraluminally or extraluminally, it is highly relevant to analyze their luminal behavior under pressurization. To demonstrate the efficacy in the design of the TA and HA exoskeletons to keep their intraluminal geometry, we numerically modeled their silicone chambers (Fig. 5.3(b) and (Fig. 5.4(b)), unconstrained and under pressurization. Typically, a spring or helical-like element extends by increasing its pitch [156] as it displaces each coil in order to axially extend. Because of this, we modeled three variations of the helical actuator (HA) (Fig. B.5(a-c, a'-c')), each of them with a different coiling pitch, to determine the relationship between pitch increase and intraluminal deformation, as well as modeling the TA chamber (Fig. B.5(d,d')). First, we developed 3D models of the soft actuators on Fusion 360 (Autodesk®) and then, imported them into Abaqus/CAE (Simulia, Dassault Systemes^{TM}). The actuators models were meshed using quadratic tetrahedral, 3D solid hybrid elements (C3D10H). To capture the hyperelastic behavior of silicone, we used the Ogden material model, which parameters are described

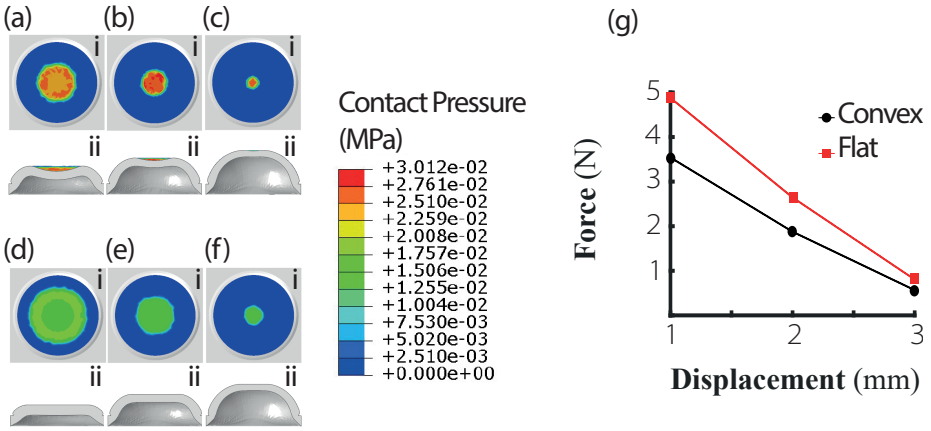

Fig. B.4: Contact analysis results. Top undeformed-view of the plotted contours showing contact pressure concentrations in the ballooning membrane against (a-c) the convex shape (d-f) and the flat shape, with a separation of 1, 2 and 3 mm respectively. Inserts ii of (a-c) show a deformed side cross-sectional view of the convex shape. Inserts ii of (d-f) show a deformed side cross-sectional view of the flat shape. (g) Comparison of the evolution in the contact force exerted for both contact interfaces.

in [4]. These settings were kept constant across all simulations using 3D Solid objects. Boundary conditions and loads are represented in Fig. B.5(a'-d').

B.3.1 Intraluminal Deformation of the Helical Actuator

By comparing the top (Fig. B.6(a-c)) and front views (Fig. B.6(a'-c')) of the helical chambers, it can be observed that the intraluminal area tends to deform in a drop-like shape and decrease when pressurized. This size reduction is confirmed by Fig. B.6(e) and (f) that shows that the intraluminal area and circumference of the helical chambers decreases with pressurization. A helical chamber with a pitch of 9 mm increases its intraluminal area at a pressure of 16 kPa by 0.5%, however, it decreases by 12%, 37% and 66% at 18, 20 and 22 kPa respectively. When the pitch is 18 mm, the intraluminal area is reduced by 3%, 17%, 41%, and 70% respectively, and when the pitch is 36 mm, the intraluminal area is reduced by 5%, 20%, 43% and 69% respectively. Since the changes in area might not suffice to describe the deformation of the intraluminal area, we also measured the changes in circumference. A helical chamber with a pitch of 9 mm increases its intraluminal circumference by 3% and 0.67% at a pressure of 16 and 18 kPa respectively. However, it decreases by 7.9% and 26.4% at 20 and 22 kPa respectively. When the pitch is 18 mm, the helical intraluminal circumference increases by 1.6% at a pressure of 16 kPa. However, it decreases by 1.76%, 10.5% and 29% at 18, 20 and 22 kPa respectively. When the pitch is 36 mm, the intraluminal circumference increases by

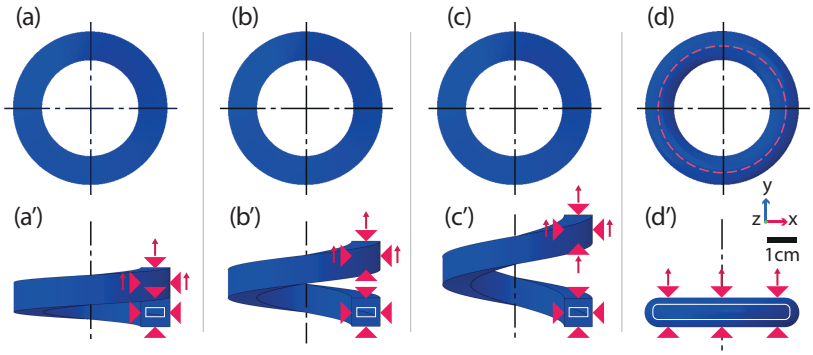

Fig. B.5: Numerical modeling setup for the evaluation of intraluminal deformation showing geometries and boundary conditions. (a-d) Top and (a'-d') front view of the relaxed helices with a pitch of 9, 18 and 36 mm and a torus respectively. For clarity, the boundary conditions of the torus were also marked as a dashed line in the top view. The load was applied throughout the channels in the chambers, which cross-sectional profile is highlighted as a solid line.

0.67% at a pressure of 16 kPa. However, it decreases by 3.45%, 11.4% and 28.5% at 18, 20 and 22 kPa respectively.

B.3.2 Intraluminal Deformation of the Toroidal Actuator

By comparing the top (Fig. B.6(d)) and front views (Fig. B.6(d')) of the toroidal chamber, it can be observed that the intraluminal area tends to keep its circular shape. However, Fig. B.6(e) and (f) show that there are variations in the intraluminal area and circumference in relation to the pressure applied to the chamber. The intraluminal area of the toroidal chamber decreases by 23%, 32%, 38% and 43% at 16, 18, 20 and 22 kPa respectively and its intraluminal circumference increases by 12%, 17%, 21% and 24% at 16, 18, 20 and 22 kPa respectively.

In summary, intraluminal deformation of the helical chambers is directly proportional to its inner pressure and the pitch between coils. However, the effects of the different pitch on the lumen deformation become similar at $\sim$ 22 kPa. The toroidal chamber showed to keep the circular shape consistently among pressures, with reductions in area and circumference of up to 43% and 24% respectively; 39% and 14% lower area and circumference reduction than the helical chamber. These results are an indication of the efficacy of the semi-soft exoskeletons used in the M2H-HBMAs to achieve pure-motions in the HA (Section 5.4.1.4).

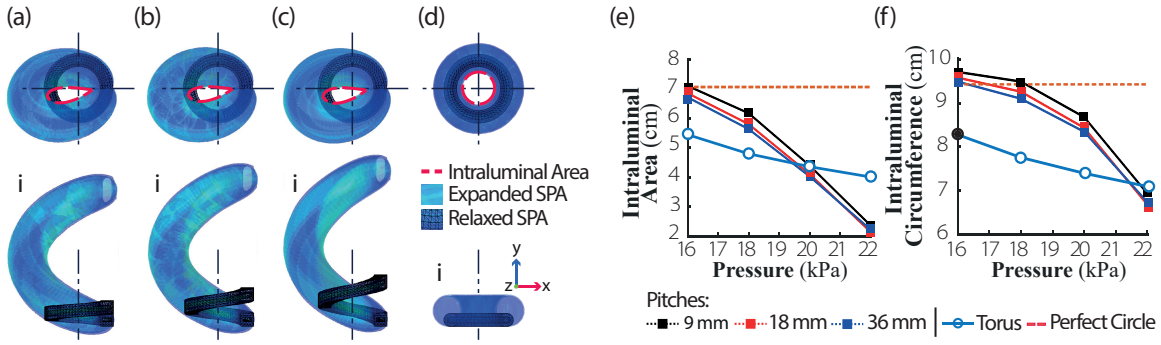

Fig. B.6: Intraluminal deformation of unconstrained helices and a torus. (a-c) Top and (a'-c') front views of the actuated helices with a pitch of 9, 18 and 36 mm respectively at 22 kPa of pressure. (d) Top and (d') front view of an actuated torus also actuated at 22 kPa of pressure. (e) Intraluminal deformation in function of pressure based on area and (f) circumference. The dashed lines in both (e) and (f) show the ideal behavior of the actuators for the clinical application, in which the luminal area remains undeformed regardless of the pressure conditions which is the ideal scenario.

B.4 Comparison to braided pure-extension actuators

We fabricated a set of three pure-extension soft braided actuators (BA) with normalized dimensions (Fig. B.7(a)) to one module of the M2H-HBMAs ((Fig. 5.3(b) and (Fig. 5.4(b)) to provide a preliminary comparison to the actuators presented in this work in terms of extension and strength. We selected this type of actuator because they have demonstrated to reach pure-extension and compression of $\sim 300\%$ [78] at relatively low levels of pressure in comparison to their hard counterparts. Details on the design and operating principle of the BAs can be found in [37]. The experimental setup is shown in Fig. B.7(b). The pressure conditions were kept consistent for all the BAs and M2H-HBMAs.

The experimental results show that the BA can axially extend only 7.8% (Fig. B.7(c)) under the same pressure conditions than the M2H-HBMAs and withstand up to 0.8 N of load before buckling under the same pressure and load conditions as the M2H-HBMAs. This represents 300% and more than a thousand percent lower axial extension and strength capabilities than the M2H-HBMAs respectively. The reason for the low performance of the BAs is that, although pure-extension soft BAs can reach higher extensions than the M2H-HBMAs, they also require 280% [78] higher pressure levels to reach similar extensions of $\sim 30-40\%$ of the M2H-HBMAs.

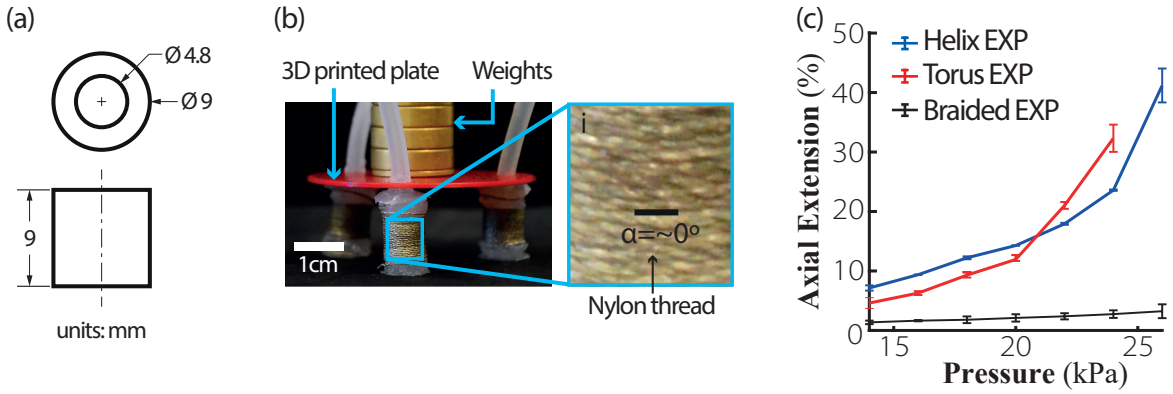

Fig. B.7: Braided actuator: (a) General dimensions and (b) experimental setup for the structural strength characterization. The axial extension characterization was conducted without the weights. (c) Plot showing a comparison of the axial extension performance under identical conditions between the M2H-HBMAs and the BAs.

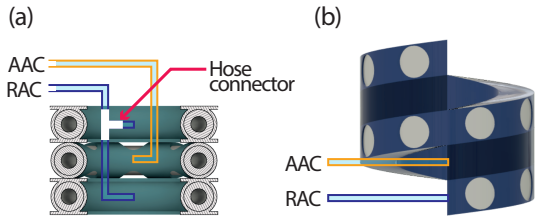

Fig. B.8: Diagrams showing the locations of the air inlets for the (a) TA and (b) HA.

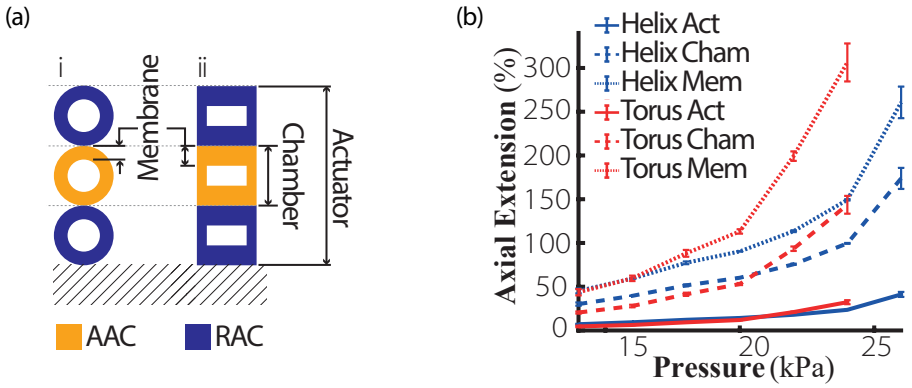

Fig. B.9: Axial extension capabilities of the M2H-HBMAs at actuator, chamber and membrane levels. (a) Schematic of the cross-sectional view of the M2H-HBMAs that identifies the experimentally measured sections highlight their extension capabilities. The exoskeletons were removed for clarity. (b) Plot comparing the extension capabilities of the membrane thickness, a chamber alone and as part of one level of the M2H-HBMAs.

References

[1] Aarabi, S., Bhatt, K. A., Shi, Y., Paterno, J., Chang, E. I., Loh, S. A., Holmes, J. W., Longaker, M. T., Yee, H., and Gurtner, G. C. (2007). Mechanical load initiates hypertrophic scar formation through decreased cellular apoptosis. *The FASEB Journal*, 21(12):3250–3261.

[2] Abbasi, P., Nekoui, M. A., Zareinejad, M., Abbasi, P., and Azhang, Z. (2020). Position and force control of a soft pneumatic actuator. *Soft Robotics*, pages 550–563.

[3] Abolmaesumi, P., Fichtinger, G., Peters, T. M., Sakuma, I., and Yang, G.-Z. (2013). Introduction to special section on surgical robotics. *IEEE transactions on biomedical engineering*, 60(4):887–891.

[4] Agarwal, G., Besuchet, N., Audergon, B., and Paik, J. (2016). Stretchable materials for robust soft actuators towards assistive wearable devices. *Scientific reports*, 6(1):1–8.

[5] Al-Ibadi, A., Nefti-Meziani, S., and Davis, S. (2017). Novel models for the extension pneumatic muscle actuator performances. In *2017 23rd IEEE international conference on automation and computing (ICAC)*, pages 1–6.

[6] Ansari, Y., Manti, M., Falotico, E., Cianchetti, M., and Laschi, C. (2017). Multiobjective optimization for stiffness and position control in a soft robot arm module. *IEEE Robotics and Automation Letters*, 3(1):108–115.

[7] Asbeck, A. T., De Rossi, S. M., Galiana, I., Ding, Y., and Walsh, C. J. (2014). Stronger, smarter, softer: next-generation wearable robots. *IEEE Robotics & Automation Magazine*, 21(4):22–33.

[8] Asbeck, A. T., De Rossi, S. M., Holt, K. G., and Walsh, C. J. (2015). A biologically inspired soft exosuit for walking assistance. *The International Journal of Robotics Research*, 34(6):744–762.

[9] Atala, A., Kasper, F. K., and Mikos, A. G. (2012). Engineering complex tissues. *Science translational medicine*, 4(160):3307–3339.

[10] Atwya, M., Kavak, C., Alisse, E., Liu, Y., and Damian, D. (2020). Flexible and expandable robot for tissue therapies-modeling and design. *IEEE Transactions on Biomedical Engineering*, 68(2):568–578.

[11] Awad, L. N., Bae, J., O'Donnell, K., De Rossi, S. M. M., Hendron, K., Sloot, L. H., Kudzia, P., Allen, S., Holt, K. G., Ellis, T. D., and Walsh, C. J. (2017). A soft robotic exosuit improves walking in patients after stroke. *Science translational medicine*, 9(400):eaai9084.

[12] Awang, M. S. and Abdullah, M. Z. (2011). Robotic neurosurgery: a preliminary study using an active vision-guided robotic arm for bone drilling and endoscopic manoeuvres. *The Malaysian journal of medical sciences: MJMS*, 18(2):53.

[13] Babu, S. M., Sadeghi, A., Mondini, A., and Mazzolai, B. (2019). Antagonistic pneumatic actuators with variable stiffness for soft robotic applications. In *2019 2nd IEEE International Conference on Soft Robotics (RoboSoft)*, pages 283–288.

[14] Balasubramanian, L., Wray, T., and Damian, D. D. (2020). Fault tolerant control in shape-changing internal robots. In *2020 IEEE International Conference on Robotics and Automation (ICRA)*, pages 5502–5508. IEEE.

[15] Banerjee, H. and Ren, H. (2017). Optimizing double-network hydrogel for biomedical soft robots. *Soft robotics*, 4(3):191–201.

[16] Bao, G., Fang, H., Chen, L., Wan, Y., Xu, F., Yang, Q., and Zhang, L. (2018). Soft robotics: Academic insights and perspectives through bibliometric analysis. *Soft robotics*, 5(3):229–241.

[17] Bar-Cohen, Y., Cardoso, V., Ribeiro, C., and Lanceros-Méndez, S. (2017). Electroactive polymers as actuators. *Advanced piezoelectric materials*, pages 319–352.

[18] Barrett, A., Davies, B., Gomes, M., Harris, S., Henckel, J., Jakopec, M., Kannan, V., Rodriguez y Baena, F., and Cobb, J. (2007). Computer-assisted hip resurfacing surgery using the acrobot® navigation system. *Proceedings of the Institution of Mechanical Engineers, Part H: Journal of Engineering in Medicine*, 221(7):773–785.

[19] Baumgartner, R., Kogler, A., Stadlbauer, J. M., Foo, C. C., Kaltseis, R., Baumgartner, M., Mao, G., Keplinger, C., Koh, S. J. A., Arnold, N., et al. (2020). A lesson from plants: High-speed soft robotic actuators. *Advanced Science*, 7(5):1903391.

[20] Bertoldi, K., Vitelli, V., Christensen, J., and van Hecke, M. (2017). Flexible mechanical metamaterials. *Nature Reviews Materials*, 2(11):1–11.

[21] Blumenschein, L. H. and Mcngüç, Y. (2019). Generalized delta mechanisms from soft actuators. In *2019 2nd IEEE International Conference on Soft Robotics (RoboSoft)*, pages 249–256. IEEE.

[22] Blumenschein, L. H., Usevitch, N. S., Do, B. H., Hawkes, E. W., and Okamura, A. M. (2018). Helical actuation on a soft inflated robot body. In *2018 IEEE International Conference on Soft Robotics (RoboSoft)*, pages 245–252.

[23] Boonvisut, P. and Çavuşoğlu, M. C. (2012). Estimation of soft tissue mechanical parameters from robotic manipulation data. *IEEE/ASME Transactions on Mechatronics*, 18(5):1602–1611.

[24] Boyraz, P., Runge, G., and Raatz, A. (2018). An overview of novel actuators for soft robotics. *Actuators*, 7(3):48.

[25] Bützer, T., Lambercy, O., Arata, J., and Gassert, R. (2020). Fully wearable actuated soft exoskeleton for grasping assistance in everyday activities. *Soft Robotics (Ahead of print)*.

[26] Calderón, A. A., Ugalde, J. C., Zagal, J. C., and Pérez-Arancibia, N. O. (2016). Design, fabrication and control of a multi-material-multi-actuator soft robot inspired by burrowing worms. In *2016 IEEE international conference on robotics and biomimetics (ROBIO)*, pages 31–38.

[27] Calisti, M., Giorelli, M., Levy, G., Mazzolai, B., Hochner, B., Laschi, C., and Dario, P. (2011). An octopus-bioinspired solution to movement and manipulation for soft robots. *Bioinspiration & biomimetics*, 6(3):036002.

[28] Cao, S., Zhao, Y., Hu, Y., Zou, L., and Chen, J. (2020). New perspectives: In-situ tissue engineering for bone repair scaffold. *Composites Part B: Engineering*, page 108445.

[29] Carnicer-Lombarte, A., Barone, D. G., Dimov, I. B., Hamilton, R. S., Prater, M., Zhao, X., Rutz, A. L., Malliaras, G. G., Lacour, S. P., Bryant, C. E., et al. (2019). Mechanical matching of implant to host minimises foreign body reaction. *bioRxiv*, page 829648.

[30] Carpi, F., Salaris, C., and De Rossi, D. (2007). Folded dielectric elastomer actuators. *Smart Materials and Structures*, 16(2):S300.

[31] Case, J. C., White, E. L., and Kramer, R. K. (2015). Soft material characterization for robotic applications. *Soft Robotics*, 2(2):80–87.

[32] Cezar, C. A., Roche, E. T., Vandenburgh, H. H., Duda, G. N., Walsh, C. J., and Mooney, D. J. (2016). Biologic-free mechanically induced muscle regeneration. *Proceedings of the National Academy of Sciences*, 113(6):1534–1539.

[33] Chattaraj, R., Bhaumik, S., Khan, S., and Chatterjee, D. (2018). Soft wearable ionic polymer sensors for palpatory pulse-rate extraction. *Sensors and Actuators A: Physical*, 270:65–71.

[34] Chossat, J.-B., Shin, H.-S., Park, Y.-L., and Duchaine, V. (2015). Soft tactile skin using an embedded ionic liquid and tomographic imaging. *Journal of mechanisms and robotics*, 7(2):021008.

[35] Chua, A. W. C., Khoo, Y. C., Tan, B. K., Tan, K. C., Foo, C. L., and Chong, S. J. (2016). Skin tissue engineering advances in severe burns: review and therapeutic applications. *Burns & trauma*, 4:1–14.

[36] Cianchetti, M., Ranzani, T., Gerboni, G., De Falco, I., Laschi, C., and Menciassi, A. (2013). Stiff-flop surgical manipulator: Mechanical design and experimental characterization of the single module. In *2013 IEEE/RSJ international conference on intelligent robots and systems*, pages 3576–3581. IEEE.

[37] Connolly, F., Polygerinos, P., Walsh, C. J., and Bertoldi, K. (2015). Mechanical programming of soft actuators by varying fiber angle. *Soft Robotics*, 2(1):26–32.

[38] Connolly, F., Walsh, C. J., and Bertoldi, K. (2017). Automatic design of fiber-reinforced soft actuators for trajectory matching. *Proceedings of the National Academy of Sciences*, 114(1):51–56.

[39] Copeland, J. G., Smith, R. G., Arabia, F. A., Nolan, P. E., Sethi, G. K., Tsau, P. H., McClellan, D., and Slepian, M. J. (2004). Cardiac replacement with a total artificial heart as a bridge to transplantation. *New England Journal of Medicine*, 351(9):859–867.

[40] Damian, D. D. (2020). Regenerative robotics. *Birth defects research*, 112(2):131–136.

[41] Damian, D. D., Arabagi, S., Fabozzo, A., Ngo, P., Jennings, R., Manfredi, M., and Dupont, P. E. (2014). Robotic implant to apply tissue traction forces in the treatment of esophageal atresia. In *2014 IEEE International Conference on Robotics and Automation (ICRA)*, pages 786–792.

[42] Damian, D. D., Arieta, A. H., and Okamura, A. M. (2011). Design and evaluation of a multi-modal haptic skin stimulation apparatus. In *2011 Annual International Conference of the IEEE Engineering in Medicine and Biology Society*, pages 3455–3458.

[43] Damian, D. D., Price, K., Arabagi, S., Berra, I., Machaidze, Z., Manjila, S., Shimada, S., Fabozzo, A., Arnal, G., Van Story, D., et al. (2018). In vivo tissue regeneration with robotic implants. *Science Robotics*, 3(14):eaaq0018.

[44] Daneshmand, M., Bilici, O., Bolotnikova, A., and Anbarjafari, G. (2017). Medical robots with potential applications in participatory and opportunistic remote sensing: A review. *Robotics and Autonomous Systems*, 95:160–180.

[45] Daya, M. and Nair, V. (2008). Traction-assisted dermatogenesis by serial intermittent skin tape application. *Plastic and reconstructive surgery*, 122(4):1047–1054.

[46] De Falco, I., Cianchetti, M., and Menciassi, A. (2017). A soft multi-module manipulator with variable stiffness for minimally invasive surgery. *Bioinspiration & biomimetics*, 12(5):056008.

[47] de Payrebrune, K. M. and O'Reilly, O. M. (2016). On constitutive relations for a rod-based model of a pneu-net bending actuator. *Extreme Mechanics Letters*, 8:38–46.

[48] de Payrebrune, K. M. and O'Reilly, O. M. (2017). On the development of rod-based models for pneumatically actuated soft robot arms: a five-parameter constitutive relation. *International Journal of Solids and Structures*, 120:226–235.

[49] Debelle, A., Hermans, L., Bosquet, M., Dehaeck, S., Lonys, L., Scheid, B., Nonclercq, A., and Vanhoestenberghe, A. (2016). Soft encapsulation of flexible electrical stimulation implant: Challenges and innovations. *European journal of translational myology*, 26(4).

[50] Della Santina, C., Katzschmann, R. K., Biechi, A., and Rus, D. (2018). Dynamic control of soft robots interacting with the environment. In *2018 IEEE International Conference on Soft Robotics (RoboSoft)*, pages 46–53.

[51] Dieffenbach, J. F. (1822). *Nonnulla de regeneratione et transplantatione*. Richter.

[52] Digumarti, K. M., Conn, A. T., and Rossiter, J. (2017). Euglenoid-inspired giant shape change for highly deformable soft robots. *IEEE Robotics and Automation Letters*, 2(4):2302–2307.

[53] Diteesawat, R. S., Helps, T., Taghavi, M., and Rossiter, J. (2020). Characteristic analysis and design optimization of bubble artificial muscles. *Soft Robotics (Ahead of print)*.

[54] Dorr, L. D., Jones, R. E., Padgett, D. E., Pagnano, M., Ranawat, A. S., and Trousdale, R. T. (2011). Robotic guidance in total hip arthroplasty: the shape of things to come. *Orthopedics*, 32(9):652–652.

[55] Driller, J. and Neumann, G. (1967). An electromagnetic biopsy device. *IEEE Transactions on Biomedical Engineering*, 1:52–53.

[56] Dua, K. S., Hogan, W. J., Aadam, A. A., and Gasparri, M. (2016). In-vivo oesophageal regeneration in a human being by use of a non-biological scaffold and extracellular matrix. *The Lancet*, 388(10039):55–61.

[57] Dua, K. S. and Sasikala, M. (2018). Repairing the human esophagus with tissue engineering. *Gastrointestinal endoscopy*, 88(4):579–588.

[58] Eça, R. and Barbosa, E. (2016). Short bowel syndrome: treatment options. *Journal of Coloproctology (Rio de Janeiro)*, 36(4):262–272.

[59] Eder, M., Hisch, F., and Hauser, H. (2018). Morphological computation-based control of a modular, pneumatically driven, soft robotic arm. *Advanced Robotics*, 32(7):375–385.

[60] Elgeneidy, K., Lohse, N., and Jackson, M. (2016). Data-driven bending angle prediction of soft pneumatic actuators with embedded flex sensors. *IFAC-PapersOnLine*, 49(21):513–520.

[61] Elshahat, A. (2011). Management of burn deformities using tissue expanders: A retrospective comparative analysis between tissue expansion in limb and non-limb sites. *Burns*, 37(3):490–494.

[62] Eming, S. A., Martin, P., and Tomic-Canic, M. (2014). Wound repair and regeneration: mechanisms, signaling, and translation. *Science translational medicine*, 6(265):265sr6–265sr6.

[63] Eming, S. A., Wynn, T. A., and Martin, P. (2017). Inflammation and metabolism in tissue repair and regeneration. *Science*, 356(6342):1026–1030.

[64] Feng, W. W. and Pangnan, H. (1975). On the general contact problem of an inflated nonlinear plane membrane. *International Journal of Solids and Structures*, 11(4):437–448.

[65] Ferhatoglu, M. F. and Kıvılcım, T. (2017). Anatomy of esophagus. In *Esophageal Abnormalities*. IntechOpen.

[66] Florez, J. M., Shah, M., Moraud, E. M., Wurth, S., Baud, L., Von Zitzewitz, J., van den Brand, R., Micera, S., Courtine, G., and Paik, J. (2016). Rehabilitative soft exoskeleton for rodents. *IEEE Transactions on Neural Systems and Rehabilitation Engineering*, 25(2):107–118.

[67] Foker, J. E., Krosch, T. C. K., Catton, K., Munro, F., and Khan, K. M. (2009). Long-gap esophageal atresia treated by growth induction: the biological potential and early follow-up results. In *Seminars in pediatric surgery*, volume 18, pages 23–29.

[68] Foker, J. E., Linden, B. C., Boyle, E. M., and Marquardt, C. (1997). Development of a true primary repair for the full spectrum of esophageal atresia. *Annals of surgery*, 226(4):533–43.

[69] Fujie, M. G. and Zhang, B. (2020). State-of-the-art of intelligent minimally invasive surgical robots. *Frontiers of Medicine*, pages 1–13.

[70] Gerboni, G., Henselmans, P. W., Arkenbout, E. A., van Furth, W. R., and Breedveld, P. (2015). Helixflex: bioinspired maneuverable instrument for skull base surgery. *Bioinspiration & biomimetics*, 10(6).

[71] Gorissen, B., Chishiro, T., Shimomura, S., Reynaerts, D., De Volder, M., and Konishi, S. (2014). Flexible pneumatic twisting actuators and their application to tilting micromirrors. *Sensors and Actuators A: Physical*, 216:426–431.

[72] Gorissen, B., Reynaerts, D., Konishi, S., Yoshida, K., Kim, J.-W., and De Volder, M. (2017). Elastic inflatable actuators for soft robotic applications. *Advanced Materials*, 29(43):1604977.

[73] Gough, Z., Chaminade, C., Barclay-Monteith, P., Kallinen, A., Lei, W., Ganesan, R., Grace, J., and McKenzie, D. R. (2017). Laser fabrication of electrical feedthroughs in polymer encapsulations for active implantable medical devices. *Medical Engineering & Physics*, 42:105–110.

[74] Grazioso, S., Di Gironimo, G., and Siciliano, B. (2019). A geometrically exact model for soft continuum robots: The finite element deformation space formulation. *Soft robotics*, 6(6):790–811.

[75] Gu, G., Wang, D., Ge, L., and Zhu, X. (2020). Analytical modeling and design of generalized pneu-net soft actuators with three-dimensional deformations. *Soft Robotics (Ahead of print)*.

[76] Hao, Y., Wang, T., Ren, Z., Gong, Z., Wang, H., Yang, X., Guan, S., and Wen, L. (2017). Modeling and experiments of a soft robotic gripper in amphibious environments. *International Journal of Advanced Robotic Systems*, 14(3):1729881417707148.

[77] Harris, S., Arambula-Cosio, F., Mei, Q., Hibberd, R., Davies, B., Wickham, J., Nathan, M., and Kundu, B. (1997). The probot—an active robot for prostate resection. *Proceedings of the Institution of Mechanical Engineers, Part H: Journal of Engineering in Medicine*, 211(4):317–325.

[78] Hawkes, E. W., Christensen, D. L., and Okamura, A. M. (2016). Design and implementation of a 300% strain soft artificial muscle. In *2016 IEEE International Conference on Robotics and Automation (ICRA)*, pages 4022–4029. IEEE.

[79] Helps, T. and Rossiter, J. (2018). Proprioceptive flexible fluidic actuators using conductive working fluids. *Soft robotics*, 5(2):175–189.

[80] Herzig, N., Jones, J., Perez-Guagnelli, E., and D. Damian, D. (2021). Model and validation of a highly extensible and tough actuator based on a ballooning membrane. *2021 IEEE International Conference on Robotics and Automation (In Press)*.

[81] Hines, L., Petersen, K., Lum, G. Z., and Sitti, M. (2017). Soft actuators for small-scale robotics. *Advanced materials*, 29(13):1603483.

[82] Hisch, F., Giusti, A., and Althoff, M. (2017). Robust control of continuum robots using interval arithmetic. *IFAC-PapersOnLine*, 50(1):5660–5665.

[83] Huang, C., Holfeld, J., Schaden, W., Orgill, D., and Ogawa, R. (2013). Mechanotherapy: revisiting physical therapy and recruiting mechanobiology for a new era in medicine. *Trends in molecular medicine*, 19(9):555–564.

[84] Huang, C. and Ogawa, R. (2010). Mechanotransduction in bone repair and regeneration. *The FASEB Journal*, 24(10):3625–3632.

[85] Hussain, M., Choa, Y.-H., and Niihara, K. (2001). Conductive rubber materials for pressure sensors. *Journal of Materials Science Letters*, 20(6):525–527.

[86] Hussey, G. S., Cramer, M. C., and Badylak, S. F. (2018). Extracellular matrix bioscaffolds for building gastrointestinal tissue. *Cellular and molecular gastroenterology and hepatology*, 5(1):1–13.

[87] Ilievski, F., Mazzeo, A. D., Shepherd, R. F., Chen, X., and Whitesides, G. M. (2011). Soft robotics for chemists. *Angewandte Chemie*, 123(8):1930–1935.

[88] Jensen, A. R., McDuffie, L. A., Groh, E. M., and Rescorla, F. J. (2020). Outcomes for correction of long-gap esophageal atresia: A 22-year experience. *Journal of Surgical Research*, 251:47–52.

[89] Jiang, M., Zhou, Z., and Gravish, N. (2020). Flexoskeleton printing enables versatile fabrication of hybrid soft and rigid robots. *Soft Robotics*, 7(6):770–778.

[90] Jones, J., Gillett, Z., Perez-Guagnelli, E., and Damian, D. D. (2020). Resistance tuning of soft strain sensor based on saline concentration and volume changes. In *Annual Conference Towards Autonomous Robotic Systems*, pages 49–52. Springer.

[91] Kalisky, T., Wang, Y., Shih, B., Drotman, D., Jadhav, S., Aronoff-Spencer, E., and Tolley, M. T. (2017). Differential pressure control of 3d printed soft fluidic actuators. In *2017 IEEE/RSJ International Conference on Intelligent Robots and Systems (IROS)*, pages 6207–6213. IEEE.

[92] Kanetaka, K. and Eguchi, S. (2020). Regenerative medicine for the upper gastrointestinal tract. *Regenerative Therapy*, 15:129–137.

[93] Katz, R. D., Rosson, G. D., Taylor, J. A., and Singh, N. K. (2005). Robotics in microsurgery: use of a surgical robot to perform a free flap in a pig. *Microsurgery: Official Journal of the International Microsurgical Society and the European Federation of Societies for Microsurgery*, 25(7):566–569.

[94] Keren, D., Eyal, O., Sroka, G., Rainis, T., Raziel, A., Sakran, N., Goitein, D., and Matter, I. (2015). Over-the-scope clip (otsc) system for sleeve gastrectomy leaks. *Obesity surgery*, 25(8):1358–1363.

[95] Khan, F. and Tanaka, M. (2018). Designing smart biomaterials for tissue engineering. *International journal of molecular sciences*, 19(1):17.

[96] Khan, K. M. and Scott, A. (2009). Mechanotherapy: how physical therapists' prescription of exercise promotes tissue repair. *British journal of sports medicine*, 43(4):247–252.

[97] Kim, J., Kim, J. W., Kim, H. C., Zhai, L., Ko, H.-U., and Muthoka, R. M. (2019). Review of soft actuator materials. *International Journal of Precision Engineering and Manufacturing*, pages 1–21.

[98] Kim, S., Laschi, C., and Trimmer, B. (2013). Soft robotics: a bioinspired evolution in robotics. *Trends in biotechnology*, 31(5):287–294.

[99] Kim, Y., Yuk, H., Zhao, R., Chester, S. A., and Zhao, X. (2018). Printing ferromagnetic domains for untethered fast-transforming soft materials. *Nature*, 558(7709):274–279.

[100] Koller, T. (2020). Mechanosensitive aspects of cell biology in manual scar therapy for deep dermal defects. *International Journal of Molecular Sciences*, 21(6):2055.

[101] Kotev, V., Boiadjiev, G., Mouri, T., Delchev, K., Kawasaki, H., and Boiadjiev, T. (2013). A design concept of an orthopedic bone drilling mechatronics system. In *Applied Mechanics and Materials*, volume 302, pages 248–251.

[102] Krafts, K. (2014). Tissue repair. In Wexler, P., editor, *Encyclopedia of Toxicology (Third Edition)*, pages 577 – 583. Academic Press, Oxford, third edition edition.

[103] Kumar, N., Wirekoh, J., Saba, S., Riviere, C. N., and Park, Y.-L. (2020). Soft miniaturized actuation and sensing units for dynamic force control of cardiac ablation catheters. *Soft Robotics (Ahead of print)*.

[104] Lai, Y.-C., Deng, J., Liu, R., Hsiao, Y.-C., Zhang, S. L., Peng, W., Wu, H.-M., Wang, X., and Wang, Z. L. (2018). Actively perceiving and responsive soft robots enabled by self-powered, highly extensible, and highly sensitive triboelectric proximity-and pressure-sensing skins. *Advanced Materials*, 30(28):1801114.

[105] LaMattina, J. C., Alvarez-Casas, J., Lu, I., Powell, J. M., Sultan, S., Phelan, M. W., and Barth, R. N. (2018). Robotic-assisted single-port donor nephrectomy using the da vinci single-site platform. *Journal of Surgical Research*, 222:34–38.

[106] Lancerotto, L. and Orgill, D. P. (2014). Mechanoregulation of angiogenesis in wound healing. *Advances in wound care*, 3(10):626–634.

[107] Lane, T. (2018). A short history of robotic surgery. *Annals*, 100(6):5–7.

[108] Laschi, C., Rossiter, J., Iida, F., Cianchetti, M., and Margheri, L. (2016). Soft robotics: Trends, applications and challenges. *Livorno, Italy*.

[109] Lee, J. Z., Mulpuru, S. K., and Shen, W. K. (2018). Leadless pacemaker: Performance and complications. *Trends in Cardiovascular Medicine*, 28(2):130–141.

[110] Lee, S. H., Lee, Y. B., Kim, B. H., Lee, C., Cho, Y. M., Kim, S.-N., Park, C. G., Cho, Y.-C., and Choy, Y. B. (2017). Implantable batteryless device for on-demand and pulsatile insulin administration. *Nature communications*, 8(1):1–10.

[111] Li, C., Armstrong, J. P., Pence, I. J., Kit-Anan, W., Puetzer, J. L., Carreira, S. C., Moore, A. C., and Stevens, M. M. (2018). Glycosylated superparamagnetic nanoparticle gradients for osteochondral tissue engineering. *Biomaterials*, 176:24–33.

[112] Lim, C. T., Bershadsky, A., and Sheetz, M. P. (2010). Mechanobiology.

[113] Lindenroth, L., Housden, R. J., Wang, S., Back, J., Rhode, K., and Liu, H. (2019). Design and integration of a parallel, soft robotic end-effector for extracorporeal ultrasound. *IEEE Transactions on Biomedical Engineering*, 67(8):2215–2229.

[114] Liu, S.-Q., Lv, Y., Fang, Y., Luo, R.-X., Zhao, J.-R., Luo, R.-G., Li, Y.-M., Zhang, J., Zhang, P.-F., Guo, J.-Z., et al. (2020). Magnetic compression for anastomosis in treating an infant born with long-gap oesophageal atresia: A case report. *Medicine*, 99(42).

[115] Liu, T., Wang, Y., and Lee, K. (2017). Three-dimensional printable origami twisted tower: Design, fabrication, and robot embodiment. *IEEE Robotics and Automation Letters*, 3(1):116–123.

[116] Louis, V., Chih-Sheng, L., Chevallier, D., Selber, J., Xavier, F., and Liverneaux, P. (2018). A porcine model for robotic training harvest of the rectus abdominis muscle. In *Annales de Chirurgie Plastique Esthétique*, volume 63, pages 113–116. Elsevier.

[117] Lu, N. and Kim, D.-H. (2014). Flexible and stretchable electronics paving the way for soft robotics. *Soft Robotics*, 1(1):53–62.

[118] Luo, M., Pan, Y., Skorina, E. H., Tao, W., Chen, F., Ozel, S., and Onal, C. D. (2015). Slithering towards autonomy: a self-contained soft robotic snake platform with integrated curvature sensing. *Bioinspiration & biomimetics*, 10(5):055001.

[119] Mac Murray, B. C., An, X., Robinson, S. S., van Meerbeek, I. M., O'Brien, K. W., Zhao, H., and Shepherd, R. F. (2015). Poroelastic foams for simple fabrication of complex soft robots. *Advanced Materials*, 27(41):6334–6340.

[120] MacCurdy, R., Katzschmann, R., Kim, Y., and Rus, D. (2016). Printable hydraulics: A method for fabricating robots by 3d co-printing solids and liquids. In *2016 IEEE International Conference on Robotics and Automation (ICRA)*, pages 3878–3885.

[121] Mahadevan, V. (2017). Anatomy of the oesophagus. *Surgery-Oxford International Edition*, 35(11):603–607.

[122] Marchese, A. D., Katzschmann, R. K., and Rus, D. (2015). A recipe for soft fluidic elastomer robots. *Soft robotics*, 2(1):7–25.

[123] Martinez, R. V., Branch, J. L., Fish, C. R., Jin, L., Shepherd, R. F., Nunes, R. M., Suo, Z., and Whitesides, G. M. (2013). Robotic tentacles with three-dimensional mobility based on flexible elastomers. *Advanced materials*, 25(2):205–212.

[124] Martinez, R. V., Fish, C. R., Chen, X., and Whitesides, G. M. (2012). Elastomeric origami: programmable paper-elastomer composites as pneumatic actuators. *Advanced functional materials*, 22(7):1376–1384.

[125] Martinez, R. V., Glavan, A. C., Keplinger, C., Oyetibo, A. I., and Whitesides, G. M. (2014). Soft actuators and robots that are resistant to mechanical damage. *Advanced Functional Materials*, 24(20):3003–3010.

[126] McCracken, K. W., Aihara, E., Martin, B., Crawford, C. M., Broda, T., Treguier, J., Zhang, X., Shannon, J. M., Montrose, M. H., and Wells, J. M. (2017). Wnt/β-catenin promotes gastric fundus specification in mice and humans. *Nature*, 541(7636):182–187.

[127] Mehendale, H. M. (2005). Tissue repair: an important determinant of final outcome of toxicant-induced injury. *Toxicologic pathology*, 33(1):41–51.

[128] Meng, C., Xu, W., Li, H., Zhang, H., and Xu, D. (2017). A new design of cellular soft continuum manipulator based on beehive-inspired modular structure. *International Journal of Advanced Robotic Systems*, 14(3):1–12.

[129] Meyer, U., Handschel, J., Wiesmann, H. P., and Meyer, T., editors (2009). *The History of Tissue Engineering and Regenerative Medicine in Perspective*, pages 5–12. Springer Berlin Heidelberg, Berlin, Heidelberg.

[130] Miron, G. and Plante, J.-S. (2016). Design principles for improved fatigue life of high-strain pneumatic artificial muscles. *Soft Robotics*, 3(4):177–185.

[131] Miyashita, S., Guitron, S., Yoshida, K., Li, S., Damian, D. D., and Rus, D. (2016). Ingestible, controllable, and degradable origami robot for patching stomach wounds. In *2016 IEEE International Conference on Robotics and Automation (ICRA)*, pages 909–916. IEEE.

[132] Mochizuki, K., Obatake, M., Taura, Y., Inamura, Y., Kinoshita, A., Fukuda, A., Kosaka, T., Takatsuki, M., Nagayasu, T., and Eguchi, S. (2012). A modified foker's technique for long gap esophageal atresia. *Pediatric surgery international*, 28(8):851–854.

[133] Mosadegh, B., Polygerinos, P., Keplinger, C., Wennstedt, S., Shepherd, R. F., Gupta, U., Shim, J., Bertoldi, K., Walsh, C. J., and Whitesides, G. M. (2014). Pneumatic networks for soft robotics that actuate rapidly. *Advanced functional materials*, 24(15):2163–2170.

[134] Moseley, P., Florez, J. M., Sonar, H. A., Agarwal, G., Curtin, W., and Paik, J. (2016). Modeling, design, and development of soft pneumatic actuators with finite element method. *Advanced engineering materials*, 18(6):978–988.

[135] Moshayedi, P., Ng, G., Kwok, J. C. F., Yeo, G. S. H., Bryant, C. E., Fawcett, J. W., Franze, K., and Guck, J. (2014). The relationship between glial cell mechanosensitivity and foreign body reactions in the central nervous system. *Biomaterials*, 35(13):3919–3925.

[136] Nasab, A. M., Sabzehzar, A., Tatari, M., Majidi, C., and Shan, W. (2017). A soft gripper with rigidity tunable elastomer strips as ligaments. *Soft robotics*, 4(4):411–420.

[137] Nejad, A. R., Hamidieh, A. A., Amirkhani, M. A., and Sisakht, M. M. (2020). Update review on five top clinical applications of human amniotic membrane in regenerative medicine. *Placenta*, 103:104–119.

[138] Nejad, S. P., Blaser, M. C., Santerre, J. P., Caldarone, C. A., and Simmons, C. A. (2016). Biomechanical conditioning of tissue engineered heart valves: Too much of a good thing? *Advanced drug delivery reviews*, 96:161–175.

[139] Nguyen, P. H., Lopez-Arellano, F., Zhang, W., and Polygerinos, P. (2019). Design, characterization, and mechanical programming of fabric-reinforced textile actuators for a soft robotic hand. In *2019 IEEE/RSJ International Conference on Intelligent Robots and Systems, IROS 2019*, pages 8312–8317.

[140] Nickel, V. L., Perry, J., and Garrett, A. L. (1963). Development of useful function in the severely paralyzed hand. *JBJS*, 45(5):933–952.

[141] Nigam, R. and Mahanta, B. (2014). An overview of various biomimetic scaffolds: Challenges and applications in tissue engineering. *Journal of Tissue Science & Engineering*, 5(2).

[142] O'brien, F. J. (2011). Biomaterials & scaffolds for tissue engineering. *Materials today*, 14(3):88–95.

[143] Ogura, K., Wakimoto, S., Suzumori, K., and Nishioka, Y. (2009). Micro pneumatic curling actuator-nematode actuator. In *2008 IEEE International Conference on Robotics and Biomimetics*, pages 462–467. IEEE.

[144] Onal, C. D., Tolley, M. T., Wood, R. J., and Rus, D. (2014). Origami-inspired printed robots. *IEEE/ASME transactions on mechatronics*, 20(5):2214–2221.

[145] Orabi, H., AbouShwareb, T., Zhang, Y., Yoo, J. J., and Atala, A. (2013). Cell-seeded tubularized scaffolds for reconstruction of long urethral defects: a preclinical study. *European urology*, 63(3):531–538.

[146] Paez, L., Agarwal, G., and Paik, J. (2016). Design and analysis of a soft pneumatic actuator with origami shell reinforcement. *Soft Robotics*, 3(3):109–119.

[147] Pal, A., Goswami, D., and Martinez, R. V. (2019). Elastic energy storage enables rapid and programmable actuation in soft machines. *Advanced Functional Materials*, page 1906603.

[148] Pang, C., Lee, G.-Y., Kim, T.-i., Kim, S. M., Kim, H. N., Ahn, S.-H., and Suh, K.-Y. (2012). A flexible and highly sensitive strain-gauge sensor using reversible interlocking of nanofibres. *Nature materials*, 11(9):795–801.

[149] Park, S., Mondal, K., Treadway III, R. M., Kumar, V., Ma, S., Holbery, J. D., and Dickey, M. D. (2018). Silicones for stretchable and durable soft devices: Beyond sylgard-184. *ACS applied materials & interfaces*, 10(13):11261–11268.

[150] Park, Y.-L., Chen, B.-r., Pérez-Arancibia, N. O., Young, D., Stirling, L., Wood, R. J., Goldfield, E. C., and Nagpal, R. (2014). Design and control of a bio-inspired soft wearable robotic device for ankle–foot rehabilitation. *Bioinspiration & biomimetics*, 9(1).

[151] Payne, C. J., Wamala, I., Abah, C., Thalhofer, T., Saeed, M., Bautista-Salinas, D., Horvath, M. A., Vasilyev, N. V., Roche, E. T., Pigula, F. A., et al. (2017). An implantable extracardiac soft robotic device for the failing heart: mechanical coupling and synchronization. *Soft robotics*, 4(3):241–250.

[152] Peraza-Hernandez, E. A., Hartl, D. J., Malak Jr, R. J., and Lagoudas, D. C. (2014). Origami-inspired active structures: a synthesis and review. *Smart Materials and Structures*, 23(9):094001.

[153] Perez-Guagnelli, E. and D. Damian, D. (2021). Deflected vs pre-shaped soft pneumatic actuators: A design and performance analysis towards reliable soft robots. *Soft Robotics (Under review)*.

[154] Perez-Guagnelli, E., Jones, J., and Damian, D. D. (2019). Evaluation of a soft helical actuator performance with hard and soft attachments for tissue regeneration. In *Proceedings of the 12th Hamlyn Symposium on Medical Robotics*, pages 3–4. The Hamlyn Centre.

[155] Perez-Guagnelli, E., Jones, J., Tokel, A. H., Herzig, N., Jones, B., Miyashita, S., and Damian, D. D. (2020). Characterization, simulation and control of a soft helical pneumatic implantable robot for tissue regeneration. *IEEE Transactions on Medical Robotics and Bionics*, 2(1):94–103.

[156] Perez-Guagnelli, E. R., Nejus, S., Yu, J., Miyashita, S., Liu, Y., and Damian, D. D. (2018). Axially and radially expandable modular helical soft actuator for robotic implantables. In *2018 IEEE International Conference on Robotics and Automation (ICRA)*, pages 1–9. IEEE.

[157] Pinheiro, P. F. M., e Silva, A. C. S., and Pereira, R. M. (2012). Current knowledge on esophageal atresia. *World journal of gastroenterology*, 18(28):3662–3672.

[158] Poghosyan, T., Catry, J., Luong-Nguyen, M., Bruneval, P., Domet, T., Arakelian, L., Sfeir, R., Michaud, L., Vanneaux, V., Gottrand, F., et al. (2016). Esophageal tissue engineering: Current status and perspectives. *Journal of visceral surgery*, 153(1):21–29.

[159] Poghosyan, T., Sfeir, R., Michaud, L., Bruneval, P., Domet, T., Vanneaux, V., Luong-Nguyen, M., Gaujoux, S., Gottrand, F., Larghero, J., et al. (2015). Circumferential esophageal replacement using a tube-shaped tissue-engineered substitute: an experimental study in minipigs. *Surgery*, 158(1):266–277.

[160] Polygerinos, P., Correll, N., Morin, S. A., Mosadegh, B., Onal, C. D., Petersen, K., Cianchetti, M., Tolley, M. T., and Shepherd, R. F. (2017). Soft robotics: Review of fluid-driven intrinsically soft devices; manufacturing, sensing, control, and applications in human-robot interaction. *Advanced Engineering Materials*, 19(12):1700016.

[161] Polygerinos, P., Wang, Z., Overvelde, J. T., Galloway, K. C., Wood, R. J., Bertoldi, K., and Walsh, C. J. (2015). Modeling of soft fiber-reinforced bending actuators. *IEEE Transactions on Robotics*, 31(3):778–789.

[162] Qin, L., Liang, X., Huang, H., Chui, C. K., Yeow, R. C.-H., and Zhu, J. (2019). A versatile soft crawling robot with rapid locomotion. *Soft robotics*, 6(4):455–467.

[163] Ramirez, P. T., Frumovitz, M., Pareja, R., Lopez, A., Vieira, M., Ribeiro, R., Buda, A., Yan, X., Shuzhong, Y., Chetty, N., et al. (2018). Minimally invasive versus abdominal radical hysterectomy for cervical cancer. *New England Journal of Medicine*, 379(20):1895–1904.

[164] Ranzani, T., Gerboni, G., Cianchetti, M., and Menciassi, A. (2015). A bioinspired soft manipulator for minimally invasive surgery. *Bioinspiration & biomimetics*, 10(3).

[165] Roberts, P., Damian, D. D., Shan, W., Lu, T., and Majidi, C. (2013). Soft-matter capacitive sensor for measuring shear and pressure deformation. In *2013 IEEE International Conference on Robotics and Automation*, pages 3529–3534. IEEE.

[166] Robertson, M. A., Sadeghi, H., Florez, J. M., and Paik, J. (2017). Soft pneumatic actuator fascicles for high force and reliability. *Soft robotics*, 4(1):23–32.

[167] Roche, E. T., Horvath, M. A., Wamala, I., Alazmani, A., Song, S.-E., Whyte, W., Machaidze, Z., Payne, C. J., Weaver, J. C., Fishbein, G., et al. (2017). Soft robotic sleeve supports heart function. *Science translational medicine*, 9(373).

[168] Rodriguez, J. N., Zhu, C., Duoss, E. B., Wilson, T. S., Spadaccini, C. M., and Lewicki, J. P. (2016). Shape-morphing composites with designed micro-architectures. *Scientific reports*, 6(1):1–10.

[169] Roels, E., Terryn, S., Brancart, J., Verhelle, R., Van Assche, G., and Vanderborght, B. (2020). Additive manufacturing for self-healing soft robots. *Soft robotics*, 7(6):711–723.

[170] Rosset, S., O'Brien, B. M., Gisby, T., Xu, D., Shea, H. R., and Anderson, I. A. (2013). Self-sensing dielectric elastomer actuators in closed-loop operation. *Smart Materials and Structures*, 22(10):104018.

[171] Runciman, M., Darzi, A., and Mylonas, G. P. (2019). Soft robotics in minimally invasive surgery. *Soft robotics*, 6(4):423–443.

[172] Runge, G. and Raatz, A. (2017). A framework for the automated design and modelling of soft robotic systems. *CIRP Annals*, 66(1):9–12.

[173] Rus, D. and Tolley, M. T. (2015). Design, fabrication and control of soft robots. *Nature*, 521:467–475.

[174] Saeed, M. Y., Van Story, D., Payne, C. J., Wamala, I., Shin, B., Bautista-Salinas, D., Zurakowski, D., Pedro, J., Walsh, C. J., and Vasilyev, N. V. (2020). Dynamic augmentation of left ventricle and mitral valve function with an implantable soft robotic device. *JACC: Basic to Translational Science*, 5(3):229–242.

[175] Saleem, Z. (2011). Alternatives and modifications of monopile foundation or its installation technique for noise mitigation. Technical report, Delft University of Technology.

[176] Samper-Escudero, J. L., Contreras-González, A. F., Ferre, M., Sánchez-Urán, M. A., and Pont-Esteban, D. (2020). Efficient multiaxial shoulder-motion tracking based on flexible resistive sensors applied to exosuits. *Soft Robotics*, 7(3):370–385.

[177] Selber, J. C., Baumann, D. P., and Holsinger, F. C. (2012). Robotic latissimus dorsi muscle harvest: a case series. *Plastic and reconstructive surgery*, 129(6):1305–1312.

[178] Shepherd, R. F., Ilievski, F., Choi, W., Morin, S. A., Stokes, A. A., Mazzeo, A. D., Chen, X., Wang, M., and Whitesides, G. M. (2011). Multigait soft robot. *Proceedings of the national academy of sciences*, 108(51):20400–20403.

[179] Shepherd, R. F., Stokes, A. A., Nunes, R., and Whitesides, G. M. (2013). Soft machines that are resistant to puncture and that self seal. *Advanced Materials*.

[180] Shian, S., Bertoldi, K., and Clarke, D. R. (2015). Dielectric elastomer based "grippers" for soft robotics. *Advanced Materials*, 27(43):6814–6819.

[181] Shintake, J., Sonar, H., Piskarev, E., Paik, J., and Floreano, D. (2017). Soft pneumatic gelatin actuator for edible robotics. In *2017 IEEE/RSJ International Conference on Intelligent Robots and Systems (IROS)*, pages 6221–6226. IEEE.

[182] Singhal, P., Wilson, T. S., and Maitland, D. J. (2010). Biomedical applications of thermally activated shape memory polymers. *Journal of materials chemistry*, 20(17):3356–3366.

[183] Smith, M. E. and Morton, D. G. (2010). 1 - overview of the digestive system. In Smith, M. E. and Morton, D. G., editors, *The Digestive System (Second Edition)*, pages 1 – 18. Churchill Livingstone, second edition edition.

[184] Soft Robotics Toolkit (2017). Electro-pneumatic circuit. https://softroboticstoolkit.com/low-cost-ep-circuit.

[185] Someya, T., Sekitani, T., Iba, S., Kato, Y., Kawaguchi, H., and Sakurai, T. (2004). A large-area, flexible pressure sensor matrix with organic field-effect transistors for artificial skin applications. *Proceedings of the National Academy of Sciences*, 101(27):9966–9970.

[186] Son, D., Gilbert, H., and Sitti, M. (2020). Magnetically actuated soft capsule endoscope for fine-needle biopsy. *Soft robotics*, 7(1):10–21.

[187] Souri, H., Banerjee, H., Jusufi, A., Radacsi, N., Stokes, A. A., Park, I., Sitti, M., and Amjadi, M. (2020). Wearable and stretchable strain sensors: materials, sensing mechanisms, and applications. *Advanced Intelligent Systems*, 2(8):2000039.

[188] Spencer, A. U., Kovacevich, D., McKinney-Barnett, M., Hair, D., Canham, J., Maksym, C., and Teitelbaum, D. H. (2008). Pediatric short-bowel syndrome: the cost of comprehensive care. *The American journal of clinical nutrition*, 88(6):1552–1559.

[189] Spitz, L. (2007). Oesophageal atresia. *Orphanet journal of rare diseases*, 2(1):24.

[190] Stano, G. and Percoco, G. (2020). Additive manufacturing aimed to soft robots fabrication: A review. *Extreme Mechanics Letters*, page 101079.

[191] Starke, J., Amanov, E., Chikhaoui, M. T., and Burgner-Kahrs, J. (2017). On the merits of helical tendon routing in continuum robots. In *2017 IEEE/RSJ International Conference on Intelligent Robots and Systems (IROS)*, pages 6470–6476. IEEE.

[192] Stieghorst, J. and Doll, T. (2018). Rheological behavior of pdms silicone rubber for 3d printing of medical implants. *Additive Manufacturing*, 24:217–223.

[193] Stone, I., Von Fraunhofer, J., and Masterson, B. (1986). The biomechanical effects of tight suture closure upon fascia. *Surgery, gynecology & obstetrics*, 163(5):448–452.

[194] Sugano, N. (2013). Computer-assisted orthopaedic surgery and robotic surgery in total hip arthroplasty. *Clinics in orthopedic surgery*, 5(1):1–9.

[195] Sun, Y., Song, Y. S., and Paik, J. (2013). Characterization of silicone rubber based soft pneumatic actuators. In *2013 IEEE/RSJ International Conference on Intelligent Robots and Systems (IROS)*, pages 4446–4453.

[196] Suzumori, K., Endo, S., Kanda, T., Kato, N., and Suzuki, H. (2007). A bending pneumatic rubber actuator realizing soft-bodied manta swimming robot. In *Proceedings 2007 IEEE International Conference on Robotics and Automation*, pages 4975–4980. IEEE.

[197] Szycher, M. and Poirier, V. (2021). High performance tecoflex polyurethanes in biomedical applications. In *Advances in Biomaterials*, pages 110–118. CRC Press.

[198] Takei, K., Takahashi, T., Ho, J. C., Ko, H., Gillies, A. G., Leu, P. W., Fearing, R. S., and Javey, A. (2010). Nanowire active-matrix circuitry for low-voltage macroscale artificial skin. *Nature materials*, 9(10):821–826.

[199] Takeoka, Y., Matsumoto, K., Taniguchi, D., Tsuchiya, T., Machino, R., Moriyama, M., Oyama, S., Tetsuo, T., Taura, Y., Takagi, K., et al. (2019). Regeneration of esophagus using a scaffold-free biomimetic structure created with bio-three-dimensional printing. *PloS one*, 14(3):e0211339.

[200] Takeshima, H. and Takayama, T. (2017). Geometric estimation of the deformation and the design method for developing helical bundled-tube locomotive devices. *IEEE/ASME Transactions on Mechatronics*, 23(1):223–232.

[201] Terryn, S., Mathijssen, G., Brancart, J., Lefeber, D., Van Assche, G., and Vanderborght, B. (2015). Development of a self-healing soft pneumatic actuator: A first concept. *Bioinspiration & biomimetics*, 10(4):046007.

[202] Tipnis, N. P. and Burgess, D. J. (2018). Sterilization of implantable polymer-based medical devices: A review. *International journal of pharmaceutics*, 544(2):455–460.

[203] To, C., Hellebrekers, T. L., and Park, Y.-L. (2015). Highly stretchable optical sensors for pressure, strain, and curvature measurement. In *2015 IEEE/RSJ international conference on intelligent robots and systems (IROS)*, pages 5898–5903. IEEE.

[204] Toesca, A., Peradze, N., Galimberti, V., Manconi, A., Intra, M., Gentilini, O., Sances, D., Negri, D., Veronesi, G., Rietjens, M., et al. (2017). Robotic nipple-sparing mastectomy and immediate breast reconstruction with implant: first report of surgical technique. *Annals of surgery*, 266(2):28–30.

[205] Treloar, L. (1944). Strains in an inflated rubber sheet, and the mechanism of bursting. *Rubber Chemistry and Technology*, 17(4):957–967.

[206] Trimmer, B. and Whitesides, G. (2014). An interview with george whitesides. *Soft Robotics*, 1(4):233–235.

[207] Trivedi, D., Rahn, C. D., Kier, W. M., and Walker, I. D. (2008). Soft robotics: Biological inspiration, state of the art, and future research. *Applied bionics and biomechanics*, 5(3):99–117.

[208] Truby, R. L., Katzschmann, R. K., Lewis, J. A., and Rus, D. (2019). Soft robotic fingers with embedded ionogel sensors and discrete actuation modes for somatosensitive manipulation. In *2019 2nd IEEE International Conference on Soft Robotics (RoboSoft)*, pages 322–329. IEEE.

[209] Ulanovski, D., Attias, J., Sokolov, M., Greenstein, T., and Raveh, E. (2018). Pediatric cochlear implant soft failure. *American journal of otolaryngology*, 39(2):107–110.

[210] Uppalapati, N. K. and Krishnan, G. (2018). Towards pneumatic spiral grippers: Modeling and design considerations. *Soft robotics*, 5(6):695–709.

[211] US Food and Drug Administration (2017). Implants and prosthetics. http://www.fda.gov/medical-devices/products-and-medical-procedures/implants-and-prosthetics.

[212] Van Vlierberghe, S., Dubruel, P., and Schacht, E. (2011). Biopolymer-based hydrogels as scaffolds for tissue engineering applications: a review. *Biomacromolecules*, 12(5):1387–1408.

[213] von Trotha, K.-T., Grommes, J., Butz, N., Lambertz, A., Klink, C., Neumann, U., Jacobs, M., and Binnebösel, M. (2017). Surgical sutures: coincidence or experience? *Hernia*, 21(4):505–508.

[214] Walker, J., Zidek, T., Harbel, C., Yoon, S., Strickland, F. S., Kumar, S., and Shin, M. (2020). Soft robotics: A review of recent developments of pneumatic soft actuators. In *Actuators*, volume 9, page 3.

[215] Wanaguru, D., Langusch, C., Krishnan, U., Varjavandi, V., Jiwane, A., Adams, S., and Henry, G. (2017). Is fundoplication required after the foker procedure for long gap esophageal atresia? *Journal of pediatric surgery*, 52(7):1117–1120.

[216] Wang, P., Su, Y.-J., and Jia, C.-Y. (2019). Current surgical practices of robotic-assisted tissue repair and reconstruction. *Chinese Journal of Traumatology*, 22(2):88–92.

[217] Ward, W. K. (2008). A review of the foreign-body response to subcutaneously-implanted devices: the role of macrophages and cytokines in biofouling and fibrosis. *Diabetes Sci Technol.*, 2(5):768–77.

[218] Webster III, R. J. and Jones, B. A. (2010). Design and kinematic modeling of constant curvature continuum robots: A review. *The International Journal of Robotics Research*, 29(13):1661–1683.

[219] Wehner, M., Truby, R. L., Fitzgerald, D. J., Mosadegh, B., Whitesides, G. M., Lewis, J. A., and Wood, R. J. (2016). An integrated design and fabrication strategy for entirely soft, autonomous robots. *Nature*, 536(7617):451–455.

[220] White, E. L., Case, J. C., and Kramer, R. K. (2017). Multi-mode strain and curvature sensors for soft robotic applications. *Sensors and Actuators A: Physical*, 253:188–197.

[221] Wong, T. and Gupte, G. (2019). Complications of short bowel syndrome. *Paediatrics and Child Health*, 29(9):389–393.

[222] Wu, Y., Ravnic, D. J., and Ozbolat, I. T. (2020). Intraoperative bioprinting: Repairing tissues and organs in a surgical setting. *Trends in Biotechnology*, 38(6):594–605.

[223] Xia, Y. and Whitesides, G. M. (1998). Soft lithography. *Annual review of materials science*, 28(1):153–184.

[224] Yan, J., Dong, H., Zhang, X., and Zhao, J. (2016). A three-chambed soft actuator module with omnidirectional bending motion. In *2016 IEEE International Conference on Real-time Computing and Robotics (RCAR)*, pages 505–510. IEEE.

[225] Yan, J., Zhang, X., Xu, B., and Zhao, J. (2018). A new spiral-type inflatable pure torsional soft actuator. *Soft robotics*, 5(5):527–540.

[226] Zainal, M. A., Sahlan, S., and Ali, M. S. M. (2015). Micromachined shape-memory-alloy microactuators and their application in biomedical devices. *Micromachines*, 6(7):879–901.

[227] Zhang, B., Fan, Y., Yang, P., Cao, T., and Liao, H. (2019). Worm-like soft robot for complicated tubular environments. *Soft robotics*, 6(3):399–413.

[228] Zhang, C., Zhu, P., Lin, Y., Jiao, Z., and Zou, J. (2020a). Modular soft robotics: Modular units, connection mechanisms, and applications. *Advanced Intelligent Systems*, 2(6):1900166.

[229] Zhang, J., Wang, T., Wang, J., Wang, M. Y., Li, B., Zhang, J. X., and Hong, J. (2020b). Geometric confined pneumatic soft–rigid hybrid actuators. *Soft Robotics*, pages 574–582.

[230] Zhao, H., Jalving, J., Huang, R., Knepper, R., Ruina, A., and Shepherd, R. (2016). A helping hand: Soft orthosis with integrated optical strain sensors and emg control. *IEEE Robotics & Automation Magazine*, 23(3):55–64.

[231] Zhou, J., Chen, Y., Hu, Y., Wang, Z., Li, Y., Gu, G., and Liu, Y. (2020). Adaptive variable stiffness particle phalange for robust and durable robotic grasping. *Soft robotics*, 7(6):743–757.

[232] Zhu, P. and Zhong, Z. (2021). Constitutive modelling for the mullins effect with permanent set and induced anisotropy in particle-filled rubbers. *Applied Mathematical Modelling*, 97:19–35.

[233] Zöllner, A. M., Holland, M. A., Honda, K. S., Gosain, A. K., and Kuhl, E. (2013). Growth on demand: reviewing the mechanobiology of stretched skin. *Journal of the mechanical behavior of biomedical materials*, 28:495–509.